

On the Relaxation Dynamics of Disordered Systems

Ulrich Dobramysl

Dissertation submitted to the Faculty of the
Virginia Polytechnic Institute and State University
in partial fulfillment of the requirements for the degree of

Doctor of Philosophy
in
Physics

Uwe C. Täuber, Chair
William Mather
Michel J. Pleimling
Eric R. Sharpe

August 26, 2013
Blacksburg, Virginia

Keywords: Relaxation and Disorder, Non-equilibrium statistical mechanics, Population
Dynamics, Magnetic Flux Lines
Copyright 2013, Ulrich Dobramysl

On the Relaxation Dynamics of Disordered Systems

Ulrich Dobramysl

(ABSTRACT)

We investigate the properties of two distinct disordered systems: the two-species predator-prey Lotka-Volterra model with rate variability, and an elastic line model to simulate vortex lines in type-II superconductors.

We study the effects of intrinsic demographic variability with inheritance in the reaction rates of the Lotka-Volterra model via zero-dimensional Monte Carlo simulations as well as two-dimensional lattice simulations. Individuals of each species are assigned inheritable predation efficiencies during their creation, leading to evolutionary dynamics and thus population-level optimization. We derive an effective subspecies mean-field theory and compare its results to our numerical data. Furthermore, we introduce environmental variability via quenched spatial reaction-rate randomness. We investigate the competing effects and relative importance of the two types of variability, and find that both lead to a remarkable enhancement of the species densities, while the aforementioned optimization effects are essentially neutral in the densities. Additionally, we collected extinction time histograms for small systems and find a marked increase in the stability of the populations against extinction due to the presence of variability.

We employ an elastic line model to investigate the steady-state properties and non-equilibrium relaxation kinetics of magnetic vortex lines in disordered type-II superconductors. To this end, we developed a versatile and efficient Langevin molecular dynamics simulation code, allowing us to do a careful study of samples with or without vortex-vortex interactions or disorder allows us to disentangle the various complex relaxational features present in this system and investigate their origin. In particular, we compare disordered samples with randomly distributed point defects versus correlated columnar defects. We extract two-time quantities such as the mean-square displacement, the height and density correlations, to investigate the relaxation kinetics of the system of flux lines. Additionally, we compare the steady-state mean velocity and gyration radius as a function of an external driving current in the presence of point-like and columnar disorder. We validate our simulation algorithm by matching our results against a previously-used Monte Carlo algorithm, verifying that these microscopically quite distinct methods yield similar results even in out-of-equilibrium settings.

This work was partially supported by the US Department of Energy, Office of Basic Energy Sciences (DOE-BES), under Grant No. DE-FG02-09ER46613.

To Barbara and Lea,
who let me start each day with a smile.

Acknowledgements

I would like to thank my adviser, Prof. Uwe C. Täuber, for the invaluable discussions during our countless meetings, over coffee or tea, or via email. His advice is always spot-on, and I appreciate his honest and fair criticism that aimed at helping me become a better researcher. I am especially thankful for his willingness and support in letting me explore my own ideas, and for treating me as an equal.

Thanks to Prof. Michel Pleimling for his scientific advice and suggestions. I want to acknowledge interesting discussions with my committee members Prof. Eric Sharpe, Prof. William Mather and Prof. Giti Khodoparast.

Special thanks also to Chris Thomas, who helped me sort out all the administrative problems that I encountered; and to Roger Link and Travis Heath for accommodating my somewhat unusual use cases for the department's excellent computing clusters.

I also want to thank the following people: George Daquila, for the many hours we spent in the office or outside, discussing research, life after a Ph.D. or anything else that came to our mind; G. Addison Merchut, for all the questions that make me see things differently; Brandon Bear for great philosophical discussions; Hiba Assi, for wonderful conversations about physics and the world; all the faculty, staff and students at the Virginia Tech Department of Physics, for the best place to pursue a Ph.D.; the wonderful staff at Mill Mountain Coffee Blacksburg, for providing me with a great writing environment during many hot summer days.

I want to thank my parents, Elfriede and Wilhelm, who always encourage me to pursue my dreams. As a child they unceasingly supported my curiosity, for which I will be ever grateful. Thanks also to my uncle, Bernhard, for the time he spent teaching me about electronics, how to think algorithmically, and how to properly do electronic measurements.

And last, but most importantly, I would like to thank my wife Barbara for her love and incredible support during this graduate endeavor and for many discussions about both of our fields of research and science in general, and our daughter Lea for making my life brighter.

Contents

Foreword	1
I Population Dynamics	3
1 Introduction	4
1.1 Ecology and Population Dynamics	4
1.2 Predator-Prey Competition	5
1.3 Mean-Field Equations	6
1.4 Stochasticity and Simulations	9
1.5 Spatial Structure	10
1.6 Variability	12
1.7 Evolutionary Dynamics	14
2 Demographic Variability	16
2.1 Model Rules	16
2.2 Doi-Peliti Formalism and Mean-Field Equations	18
2.2.1 Master Equation	18
2.2.2 Fock-space Equivalent Formulation and the Time Evolution Operator	20
2.2.3 Coherent-State 'Action' and Mean Field Equations	22
2.2.4 Steady-State Solutions	24
2.3 Population Distributions from Simulations	25

3 Spatial vs. Demographic Variability	29
3.1 Model	29
3.2 Steady-State Particle Density	30
3.3 Extinction Statistics	33
4 Conclusions	35
5 Bibliography	37
II Vortex Line Relaxation	40
6 Introduction	41
6.1 Vortex Lines in Type-II Superconductors	41
6.2 Dissipation, Pinning and Vortex Matter	42
6.3 Physical Aging	44
6.4 Overview	44
7 Theoretical Background	46
7.1 Ginzburg-Landau Theory of Superconductivity	46
7.1.1 The Ginzburg-Landau Equations	47
7.1.2 Superconductivity	47
7.1.3 London Penetration Depth and Coherence Length	48
7.1.4 The Ginzburg-Landau Parameter	49
7.1.5 Vortex formation	49
7.1.6 Abrikosov Lattices	51
7.1.7 Pinning	52
7.2 Elastic Line Model	53
7.2.1 Effective Model Hamiltonian	53
7.2.2 Langevin Molecular Dynamics	54
7.3 Comparison of Microscopic Algorithms	54

7.3.1	Material Parameters	55
8	Steady State Properties of Driven Systems	56
8.1	Point-Like Pinning Sites	57
8.2	Columnar Pinning Sites	57
9	Relaxation	61
9.1	Relaxation Simulation Protocol	62
9.2	Measured Quantities	62
9.3	Free Non-interacting Vortex Lines	63
9.4	Non-interacting Vortices with Point Disorder	67
9.5	Interacting Vortex Lines without Disorder	70
9.6	Interacting Vortex Lines with Point Disorder	73
9.7	Non-interacting Vortices with Columnar Defects	76
9.8	Interacting Vortex Lines with Columnar Defects	79
9.9	Finite-Size Effects	82
10	Conclusions	85
11	Bibliography	87
A	Monte Carlo Simulations	93
A.1	Population Dynamics	94
A.2	Metropolis Monte Carlo	95
B	Langevin Molecular Dynamics	97

List of Figures

1.1	Lotka-Volterra mean-field oscillations and phase space trajectory.	7
1.2	Population densities from a single Lotka-Volterra Monte Carlo simulation run.	8
1.3	Snapshots from a one-dimensional and a two-dimensional Lotka-Volterra Monte Carlo simulation run.	11
2.1	Inheritance model rules.	17
2.2	Population distributions for various values of the inheritance distribution width w_P .	26
2.3	Population distributions for various values of the inheritance distribution width w_P from two-dimensional lattice simulations.	27
3.1	The (quasi-)steady-state predator density as a function of spatial and individual variability, as well as variability and spatial influence.	31
3.2	Correlation lengths and relaxation time as a function of variability.	32
3.3	Extinction time probability and mean extinction time in a small system of 10×10 lattice sites as a function of individual variability w_P .	34
6.1	Mean-field phase diagram of a type-II superconductor.	42
7.1	Dependence of the free energy F on the order parameter ψ for (a) $\alpha > 0$ and (b) $\alpha < 0$.	47
7.2	Isolated vortex.	50
7.3	Triangular vortex lattice solutions.	51
8.1	Steady-state (a) velocity and (b) gyration radius of $N = 16$ vortex lines with a length of $L = 20$ elements as a function of the driving force F_d in the presence of point pins with varying disorder potential strength p .	58

8.2	Steady-state (a) velocity and (b) gyration radius of $N = 16$ vortex lines with $L = 20$ as a function of the driving force F_d in the presence of columnar disorder.	59
9.1	Relaxation behavior of (a) the vortex line mean-square displacement $B(t, 0)$, (c) the squared gyration radius $r_g^2(t)$, and (b,d) the associated effective exponents β_B and β_h over time for free non-interacting flux lines with length $L = 10$ (\bullet marker), $L = 640$ (\times marker) and $L = 2560$ (\blacktriangleright marker) averaged over at least 1000 realizations. (<i>Adapted from reference [60], figure 3.</i>)	65
9.2	Relaxation of two-time quantities in a system of non-interacting flux lines without disorder for a line length of (a-c) $L = 10$ and (d-f) $L = 2560$, averaged over 800 different noise realizations.	66
9.3	Relaxation behavior of (a) the flux line mean-square displacement $B(t, 0)$, (c) the squared gyration radius $r_g^2(t)$, and (b, d) the associated effective exponents β_B and β_h over time for non-interacting vortices subject to point pins with potential strength $p = 0.01\epsilon_0$ (\bullet marker) and $p = 0.05\epsilon_0$ (\blacktriangleright), averaged over 1000 realizations.	68
9.4	Relaxation of (a,d) the mean-square displacement, (b,e) the height autocorrelation function, and (c,f) the density autocorrelation in a system of non-interacting vortex lines of length $L = 640$, subject to randomly distributed point pins with a potential depth of (a-c) $p = 0.01\epsilon_0$ and (d-f) $p = 0.05\epsilon_0$; data averaged over 1000 realizations.	69
9.5	Relaxation behavior of (a) the flux line mean-square displacement $B(t, 0)$, (c) the squared gyration radius $r_g^2(t)$, and (b, d) the associated effective exponents β_B and β_h over time for interacting vortices in a system without pinning centers, averaged over 5000 realizations.	71
9.6	Relaxation of (a,d) the mean-square displacement, (b,e) the height autocorrelation function, and (c,f) the density autocorrelation in a system of interacting flux lines without disorder and $L = 640$; data averaged over 800 realizations.	72
9.7	Relaxation behavior of (a) the flux line mean-square displacement $B(t, 0)$, (c) the squared gyration radius $r_g^2(t)$, and (b, d) the associated effective exponents β_B and β_h over time for interacting vortices in a system with point-like disorder of strength $p = 0.05\epsilon_0$, averaged over 1000 realizations.	74
9.8	Relaxation of (a) the mean-square displacement, (b) the normalized height autocorrelation function, and (c) the density autocorrelation in a system of interacting vortex lines with point pinning centers of strength $p = 0.05\epsilon_0$ and $L = 640$; data averaged over 800 realizations. (<i>Adapted from reference [60], figure 10.</i>)	75

9.9	The normalized two-time height autocorrelation function $C(t, s)$ for different values of the vortex mass m in a system of interacting flux lines subject to randomly distributed point pins of strength $p = 0.05\epsilon_0$, at waiting time $s = 8$, and averaged over 1000 simulation runs.	76
9.10	Relaxation behavior of (a) the flux line mean-square displacement $B(t, 0)$, (c) the squared gyration radius $r_g^2(t)$, and (b, d) the associated effective exponents β_B and β_h over time for non-interacting vortices subject to columnar pinning centers with $p = 0.05\epsilon_0$; data averaged over 10000 realizations.	77
9.11	Relaxation of (a) the mean-square displacement, (b) the height autocorrelation function, and (c) the density autocorrelation in a system of non-interacting flux lines of length $L = 640$ subject to randomly distributed columnar pins of strength $p = 0.05\epsilon_0$; data averaged over 1000 realizations.	78
9.12	Non-equilibrium relaxation of (a) the flux line mean-square displacement $B(t, 0)$, (c) the squared gyration radius $r_g^2(t)$, and (b, d) the associated effective exponents β_B and β_h over time for interacting vortices in a system with columnar defects of strength $p = 0.05\epsilon_0$, averaged over 1000 realizations.	80
9.13	Relaxation of (a) the mean-square displacement, (b) the normalized height autocorrelation function, and (c) the density autocorrelation in a system of interacting vortices of length $L = 640$ with columnar defects of strength $p = 0.05\epsilon_0$; data averaged over 800 realizations. (<i>Adapted from reference [60], figure 15.</i>)	81
9.14	Non-equilibrium relaxation of the flux line mean-square displacement $B(t, 0)$ and the squared gyration radius $r_g^2(t)$ over time for non-interacting vortices in systems with point-like and columnar defects with identical pinning strengths $p = 0.05\epsilon_0$ for (a,b) $L = 2$ and (c,d) $L = 10$, averaged over 10000 realizations. (<i>Adapted from reference [60], figure 16.</i>)	83
B.1	Vortex line discretization scheme.	98
B.2	Shape of the pinning and interaction potentials	99

Foreword

Disordered systems are ubiquitous in nature. Experimental physicists and biologists have to deal with this fact every day. The kind, shape and stochastic distribution of the disorder can have a profound impact on the macroscopic properties of the system in question. This dissertation addresses two highly distinct examples of systems containing randomness and disorder: the effects and influence of environmental and individual randomness on a two-species predator-prey model; and the steady-state properties and relaxation kinetics of magnetic vortex lines in disordered type-II superconductors. In both projects, numerical investigations using a variety of stochastic computer simulations methods were carried out in order to clarify the role and influence of disorder.

The former topic addresses a modification of the famous Lotka-Volterra predator-prey model, which is one of the cornerstones of population dynamics and ecology. This work is a continuation of a project started in 2006, in which we investigated the effects of purely spatial randomness in the reaction rates of predator and prey. Real ecosystems are generally non-homogeneous, hence it is crucial to clarify the influence of environmental variability on the properties of such systems. Here, we expanded the scope of the project by introducing variability in individuals, together with the concept of inheritance, which leads to evolutionary optimization on the population level. We compared the effects of these features with the influence of environmental variability. The results are presented in part I of this work.

The second topic concerns the dynamics of magnetic flux (vortex) lines in type-II superconductors. In technological applications of these materials, an effective pinning mechanism for vortex lines needs to be implemented to avoid the generally undesirable dissipation of energy. Pinning is provided by various kinds of defect sites in the crystal lattice, which act as effective potential wells for vortex lines. We employ an elastic line description of interacting flux lines subject to disorder due to defects and external driving currents to simulate the behavior of this system. The interplay of the thermal, elastic, interaction and disorder energy scales render this system highly complex. We aim to disentangle the various observable effects and determine their origin by employing an efficient Langevin molecular dynamics algorithm. This is the scope of the second part of this work.

In both of these topics we investigate the relaxation kinetics and the stationary properties of disordered systems. They differ in the manifestation of disorder and the field of applicability:

interaction rates and ecology versus randomized energy landscapes and superconductivity. However, the tools and algorithms we employ to analyze these systems are very similar in nature, demonstrating once again the versatility of the instruments of statistical physics.

As described above, this dissertation is split into two parts. Each part starts with a thorough introduction to familiarize the reader with the respective field. The subsequent chapters are dedicated to various sub-topics and results thereof, followed by conclusions and possible future avenues of research. Both parts finish with a section containing the respective references, which are numbered consecutively and uniquely throughout the whole document.

Part I

Population Dynamics

Chapter 1

Introduction

Parts of this chapter were adapted from our publication:

U. Dobramysl, U. C. Täuber, to appear in JSTAT (2013). “Copyright (2013) by the Institute of Physics.”

1.1 Ecology and Population Dynamics

The field of population dynamics deals with the mathematical modeling of interacting species. It has been a very active field since about 40 years [1, 2, 3, 4] and continues to provide exciting challenges. Ecological environments are complicated systems with many participating agents, fluxes of energy and resources and many inputs and outputs. It is generally neither feasible nor desirable to model all the microscopic interactions and processes occurring in such a complex system. It would require a tremendous amount of computational power and in general a more detailed knowledge of system’s parameters than is available. In addition, such an approach would not produce any new results or insights since it just copies the ecological environment as a whole. More importantly, we would not be able to identify critical components and parameters.

Take, for example, an ephemeral pond ecosystem: Two abundant species in such a system are tadpoles and mosquito larvae, both generally considered to be herbivores, consuming different types of algae and detritus [5]. However, under certain circumstances the mosquito larvae can start to prey upon the tadpole [6, 7]. In addition to these species, there can be other species, predators and prey in this ecosystem. All of them are connected either through direct predator-prey relationships or indirect competition for resources. Energy enters this system primarily through algae, which thrive depending on various conditions, such as temperature, sunlight exposure and water acidity. There can be spatial variations of resource availability due to differences in hydrodynamic flows. All this is to illustrate that

the interactions in such an ecosystem are complex and cannot be all taken into account when creating a model.

Hence, it is important to start from a high-altitude perspective and identify the most important components of the system. This step also depends on the particular questions or quantities we are interested in. If we are interested only in the interactions between a predator fish and its prey, a tadpole, we can usually forget about the details and competition of multiple algae bacteria species, and assume that the algae are just a resource with a steady growth rate that provides food for higher level organisms. We can go further, and approximate the algae with an infinite resource which the tadpole species consumes at a steady rate, yielding a steady reproduction rate. Assuming that the tadpole is the predator fish's only food source, the predator fish reproduction is inherently coupled to its ability to consume tadpoles. Hence we can lump the predator reproduction and its interaction with the prey into one process, the predation process. The predator fish is preyed upon by other bigger fish, but we are not interested in these interactions and can probably assume a steady rate of mortality of our predator. Of course, one needs to check later that, by making approximations, no essential information was lost and the model still exhibits the features of the real ecological neighborhood, or at least the components we are interested in. Our model consists now of the prey reproduction, the predator-prey interaction and the predator mortality. This model is called the Lotka-Volterra predator-prey model and we will come back and discuss this model in much more detail in the subsequent sections and chapters.

There exists a wealth of different models for various applications. The ecological dynamics of three, cyclically competing species of californian lizards can be modeled using the rock-paper-scissors model [8, 9]. In the case of highly asymmetric interaction rates, the three species rock-paper-scissors model can be mapped to the two species Lotka-Volterra model [10]. The cyclic competition between four and more species has also been extensively studied [11, 12, 13, 14].

1.2 Predator-Prey Competition

We are now coming back to the Lotka-Volterra model, which I mentioned in 1.1. It was originally introduced in 1920 by A. J. Lotka to study certain types of chemical reactions [15]. Later, it was independently proposed in 1926 by V. Volterra, to study the predator-prey relationship of fish in the Adriatic sea [16]. The Lotka-Volterra model consists of two species, the predators A and the prey B . These species are governed by three rules, namely:



The first rule (1.1a) governs predator mortality. If only this rule would be present, the predator population would decay exponentially with a characteristic rate μ . The second rule (1.1b) yields prey reproduction and would lead to an exponential increase in the number of prey in the absence of any controlling processes, such as predation or the introduction of finite carrying capacities (i.e. restrictions on the global or local population size). The rate σ controls this process. Finally, the third rule (1.1c) introduces predator-prey interaction. A prey particle is consumed by a predator with a predation rate λ and simultaneously a new predator particle is created. Hence, the only way the predator population can be sustained (or grow) is by consuming prey, which is also the only way the prey population can be kept from growing indefinitely.

There are a number of assumptions that are made in this model:

- The prey population reproduces at a constant rate, which implies that growth is not limited by the availability of food resources of this species.
- The mortality of single predators is constant and doesn't depend on the abundance of prey, a rather unrealistic assumption.
- Natural processes that might lead to prey death occur on much larger time scales than the predation interaction, hence they are negligible. This is probably justified as long as both species coexist. In the event of predator extinction or near-extinction this assumption might yield unnatural results.
- Predator reproduction is directly coupled to predation. While it is reasonable to assume a connection between the reproduction rate of a predator species and the availability of food, a direct conversion of prey to predator is too simple.

This list is by no means exhaustive. A more thorough criticism of the Lotka-Volterra model can be found in reference [17].

1.3 Mean-Field Equations

In order to construct the mean-field equations of the Lotka-Volterra model (1.1) one assumes that the populations of both species are well-mixed and distributed homogeneously, such that one can ignore spatial and temporal correlations and fluctuations. Since the predator population decreases exponentially with rate μ , the change of the predator population has to include a term $-\mu a(t)$, where $a(t)$ denotes the time-dependent and spatially averaged density of species A . Similarly, the prey population density $b(t)$ increases exponentially with a rate σ , hence it must include a term $\sigma b(t)$. The predation interaction depends on the availability of both predators and prey, hence the interaction term has to depend on both densities and the predation rate λ . The interaction is conservative in the sense that one prey

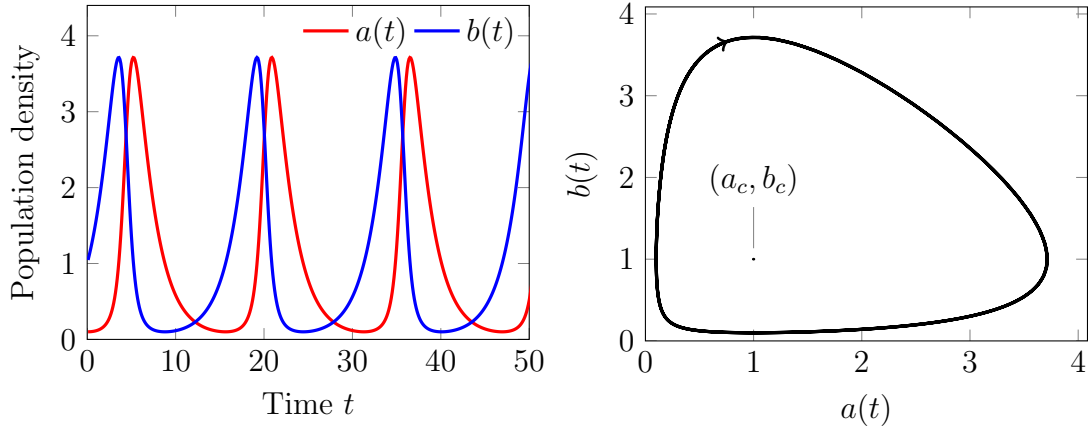


Figure 1.1: Lotka-Volterra mean-field oscillations and phase space trajectory. The Lotka-Volterra mean-field equations (1.2) give rise to nonlinear oscillations around the coexistence fixed point $(\sigma/\lambda, \mu/\lambda)$. The left panel shows the predator and prey population densities $a(t)$ and $b(t)$ as a function of time t for the reaction rates $\sigma = 0.5$, $\mu = 0.5$ and $\lambda = 0.5$ (τ indicates unit time) and initial densities of $a(0) = 0.1$ and $b(0) = 1$. The oscillations are clearly visible. The right panel displays the phase space trajectory as a closed cycle around the coexistence fixed point. (Adapted from reference [19], figure 1.)

is converted into exactly one predator, thus the mean-field factorization of the interaction term $\lambda a(t)b(t)$ enters positively and negatively into the predator and prey density change, respectively. Putting it all together yields the Lotka-Volterra mean-field equations:

$$\frac{d}{dt}a(t) = -\mu a(t) + \lambda a(t)b(t) \quad (1.2a)$$

$$\frac{d}{dt}b(t) = \sigma b(t) - \lambda a(t)b(t) \quad (1.2b)$$

These equations may be derived in a more formal manner via the master equation of the Lotka-Volterra model (1.4) (for the detailed procedure see reference [18]).

By setting the density change to zero, one immediately finds the fixed points of this system with stationary densities (a_{fp}, b_{fp}) :

1. The trivial fixed point where both population densities are zero $(0, 0)$.
2. The predator extinction fixed point, with the prey population tending to infinity $(0, \infty)$.
3. The coexistence fixed point where both predator and prey densities are finite $(a_c = \sigma/\lambda, b_c = \mu/\lambda)$.

The trivial and the predator extinction fixed point are both linearly unstable with respect to small perturbations in the densities a and b (with $\lambda = 0$ the state $(0, \infty)$ becomes stable).

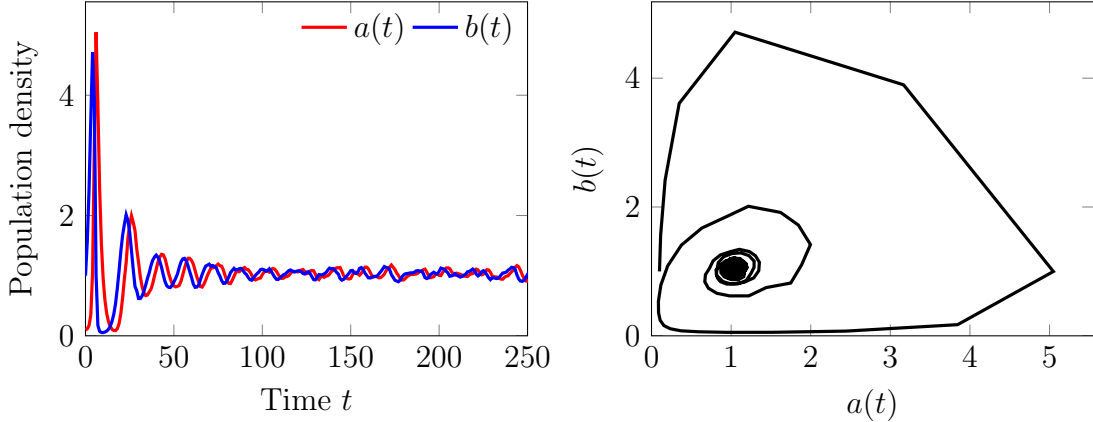


Figure 1.2: Population densities from a single Monte Carlo simulation run. The left panel shows the densities $a(t)$ and $b(t)$ as a function of time t for $\sigma = 0.5$, $\mu = 0.5$ and $\lambda = 0.5$ and initial densities of $a(0) = 0.1$ and $b(0) = 1$. One can clearly see that the Lotka-Volterra oscillations are now damped due to the stochastic nature of the simulation and the densities approach the coexistence fixed point. After reaching the steady state the densities perform erratic oscillations around these values driven by population number fluctuations. The right panel shows that the phase space trajectory of the simulation run is a spiral beginning at the initial densities of $(0.1, 1)$ and approaching the (quasi)-steady-state coexistence point $(1 + \epsilon_a, 1 + \epsilon_b)$. The deviations ϵ_a and ϵ_b stem from a renormalization of the steady-state density due to fluctuations. (Adapted from reference [19], figure 2.)

The coexistence fixed point is marginally stable, linear stability analysis yields imaginary eigenvalues, hence this fixed point gives rise to marginal cycles. This is the origin of the characteristic Lotka-Volterra oscillations with a frequency of $\omega = \sqrt{\mu\sigma}$ (this result is valid only in the linearized system in the limit of small amplitudes), displayed in figure 1.1. These stable phase-space orbits are associated with a first integral of motion of the Lotka-Volterra mean-field equations. By dividing equations (1.2a) and (1.2b) and separating the variables we get

$$\left(\frac{\sigma}{a} - \lambda\right)da = \left(-\frac{\mu}{b} + \lambda\right)db .$$

Integrating both sides yields the constant expression

$$K(t) = \sigma \ln a(t) + \mu \ln b(t) - \lambda[a(t) + b(t)] . \quad (1.3)$$

A rigorous stability analysis of the Lotka-Volterra mean-field equations can be found in references [20, 21].

1.4 Stochasticity and Simulations

The derivation of the mean-field equations discussed in the last section assumes that the system is well-mixed and deterministic. Correlations between species densities are assumed to be negligible and hence the nonlinear interaction term in equations (1.2) contains only the mean densities. These assumptions are, in general, unrealistic. Natural systems are inhomogeneous and exhibit spatial correlations. Processes occurring in ecological systems are generally stochastic, with associated probabilities and not deterministic. Hence, a more realistic way to obtain data on a model is to analyse its underlying master equation, containing its complete stochastic description. To numerically solve the master equation one implements the model's rules *directly* using computer simulations. These Monte Carlo or agent-based simulations use large numbers of discrete members or particles of all the species in a model and let them perform according to the rules, stochastically solving the master equation. By rescaling with an appropriate unit of time, the rates, μ , σ and λ in the Lotka-Volterra case, become probabilities for single particles acting according to their associated rule. For a more in-depth discussion of Monte Carlo simulations in the context of population dynamics see section A.1.

The master equation of the Lotka-Volterra system with parallel and independent updates reads:

$$\begin{aligned} \frac{d}{dt}P(A, B, t) = & \mu(A + 1)P(A + 1, B, t) + \sigma(B - 1)P(A, B - 1, t) \\ & + \lambda(A - 1)(B + 1)P(A - 1, B + 1, t) - (\mu A + \sigma B + \lambda AB)P(A, B, t) \end{aligned} \quad (1.4)$$

where $P(A, B, t)$ denotes the probability of the system being in a state with A predator and B prey particles at time t . By solving equation (1.4) for $dP/dt = 0$ one can see that this system has exactly one steady-state solution, namely $P(A = 0, B = 0, t \rightarrow \infty) = 1$ and $P(A > 0, B > 0, t \rightarrow \infty) = 0$ [20]. Hence, the previously unstable trivial extinction fixed point becomes a stable absorbing state. Due to the discrete nature of the stochastic system, fluctuations in the number of particles can drive the population into extinction if the number of particles becomes small. It is an absorbing state since the population can never recover from an extinction state. Moreover, this result means that any system with a finite number of particles *always* reaches the extinction state, but the extinction time scale can become quite large already for reasonably sized systems. This feature is absent in the mean-field equations since the population densities can get arbitrarily small without the population going extinct. The marginally stable species coexistence fixed point in the mean-field model becomes meta-stable in a stochastic system. While fluctuations will eventually drive the system to extinction, the coexistence state is long-lived. In Monte Carlo simulations, the population densities approach the coexistence densities via damped oscillations starting from the initial conditions. Figure 1.2 shows the species densities over time and the resulting spiral in phase space for a representative simulation run. Population fluctuations lead to small oscillations around the (quasi-)steady-state densities after the system reached the (quasi-)stationary state. Internal white noise stemming from the demographic stochasticity excites

the resonant frequency of the system and results in these small oscillations. This leads to a drastic delay in the ultimate extinction of the system [22].

By introducing the mean particle densities as

$$a(t) = \sum_{A,B=0}^{\infty} AP(A, B, t) \quad \text{and} \quad b(t) = \sum_{A,B=0}^{\infty} BP(A, B, t)$$

we can derive the mean field equations (1.2). Taking the time derivative of the mean predator density and inserting the master equation (1.4) yields

$$\begin{aligned} \frac{da}{dt} &= \sum_{A,B=0}^{\infty} A \frac{d}{dt} P(A, B, t) \\ &= \sum_{A,B=0}^{\infty} [\mu A(A+1)P(A+1, B, t) + \sigma A(B-1)P(A, B-1, t) \\ &\quad + \lambda A(A-1)(B+1)P(A, B, t) - (\mu A + \sigma B + \lambda AB)AP(A, B, t)] \\ &= \sum_{A,B=0}^{\infty} [-\mu A + \lambda AB]P(A, B, t), \end{aligned}$$

where we shifted the summations over A and B to arrive at the last step. In order to arrive at the mean-field rate equation, we need to make the approximation that the probability to be in a state described by the particle numbers A and B is factorizes into the independent probabilities of having A predators and B prey, $P(A, B, t) \approx P(A, t)P(B, t)$. This leads to

$$\frac{da}{dt} \approx -\mu a + \lambda ab,$$

which is identical to the mean-field equation for the predator population (1.2a). An analogous derivation yields the equation describing the prey population (1.2b).

1.5 Spatial Structure

Ecological systems exhibit spatial structure. Members of species move through the environment foraging or evading predators. This leads to spatial correlations in the abundance of species, and emerging spatial patterns such as spirals or wavefronts [3, 9, 23, 24]. None of these features are captured by a mean-field model or by zero-dimensional stochastic models. It is however sometimes possible to use a stochastic PDE model to describe spatial patterns [25]. In Monte Carlo simulations in an ecological context, one generally uses a simple hyper-cubic lattice of edge length L and dimensionality d to introduce spatial structure. It is assumed that a simple diffusion process is adequate to describe the movement of species

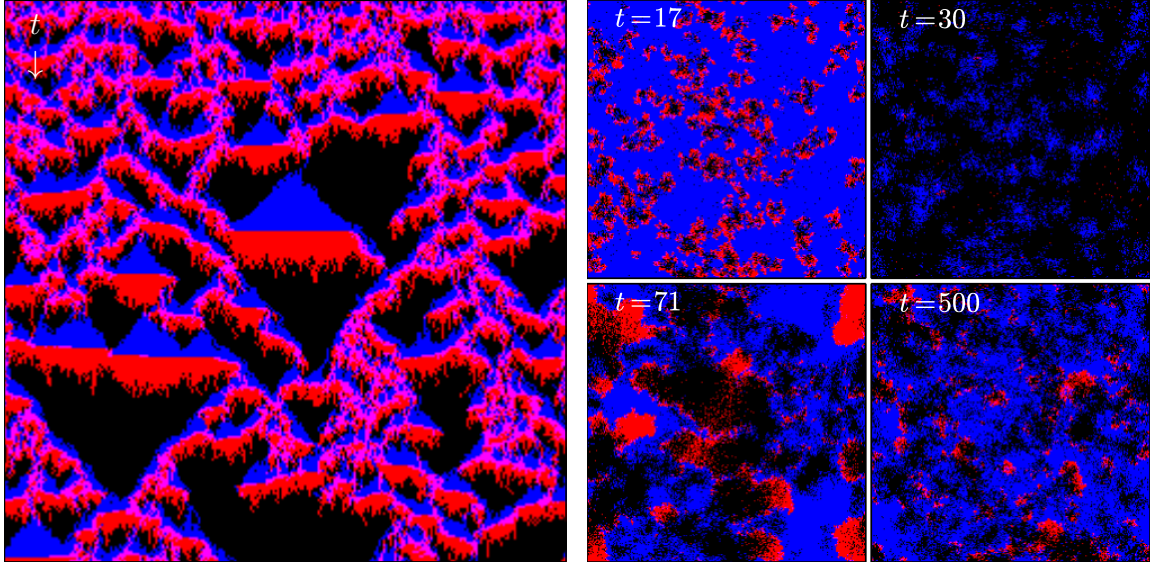


Figure 1.3: Snapshots from a one-dimensional and a two-dimensional Lotka–Volterra Monte Carlo simulation run. The left panel shows a one-dimensional simulation with $L = 250$, $\mu = 0.5$, $\sigma = 0.5$ and $\lambda = 0.3$, and initial densities $a(0) = 1 = b(0)$. The vertical direction shows time evolution while the horizontal is the spatial direction. The colors blue and red indicate the presence of prey and predator particles respectively, and a black pixel indicates an empty site. At $t = 0$ the system is still well-mixed and clusters of prey particles form and grow over time. Predators invade the cluster and thereby often remove the cluster completely. The right panel displays several snapshots from a two-dimensional simulation with $L = 250$, $\mu = 0.9$, $\sigma = 0.1$ and $\lambda = 1$. In the initial configuration, particles were randomly distributed with the densities $a(0) = 0.01$ and $b(0) = 1$. The predator-prey community survives an initial predator invasion ($t = 17$), which leads to a subsequent prey proliferation due to predator scarcity ($t = 30$). Predator fronts start to invade a large cluster of prey ($t = 71$). After the initial transient oscillations, the system reaches the coexistence steady state with smaller prey clusters and predator invasion fronts ($t = 500$). See reference [21] for a detailed discussion of similar simulation snapshots. (Adapted from reference [19], figure 3.)

through space. Hence, particles hop from one lattice site to a randomly chosen neighboring site, performing random walks. There are two distinct ways in which the lattice dynamics can be managed: Exclusion of particles and allowing multiple particles per site. The latter method can be viewed as a coarse-grained variant of the former. When using particle exclusion, only one particle is allowed per lattice site and interactions occur between particles on neighboring lattice sites. This scheme allows for a state-based simulation approach, where each lattice site is either occupied by a predator particle, a prey particle or empty. Hence, empty sites can be viewed as being occupied by a third species and the introduction of a conservation law where the number of predator and prey particles as well as this third species need to add up to the number of lattice sites L^d . Particle wandering is implemented via the random exchange of neighboring particles or empty sites. In the case of multiple particles per site, the number of particles is essentially unrestricted (although for computational reasons, it is often necessary to introduce a safety limit). Interactions happen between particles on the same lattice site. No conservation law exists when using this method. Throughout this work, the scheme allowing multiple particles per site is used. A remarkable feature of the Lotka-Volterra model is that the results in the coexistence phase are qualitatively independent of this and other details of the simulation method [20, 21, 26]. Yet it should be noted that the introduction of global or local population number restrictions (which the exclusion method effectively does) induces a predator extinction threshold, separating the two-species coexistence phase from a state with proliferating prey filling the entire system. For the predator population this phase represents an inactive, absorbing state.

Figure 1.3 shows representative snapshots from a one-dimensional and a two-dimensional Lotka-Volterra Monte Carlo simulation. The one-dimensional simulation progresses by forming prey clusters that are subsequently invaded by predators, which leads to intriguing spatio-temporal patterns. In the two-dimensional simulation, patches of prey particles form and become invaded by predators. Initially several large clusters span the system, which yields the observed synchronized oscillations in the densities. As the simulations progress the clusters become smaller and more numerous, hence the invasion-cluster growth cycles desynchronize throughout the lattice and the (quasi-)steady state is reached. The right-hand side of figure 1.3 shows several snapshots from a representative simulation run, displaying the phases mentioned above.

1.6 Variability

Ecological systems are in general not homogeneous. The availability of energy and resources can vary significantly over various length scales. Coming back to the example of the ephemeral pond ecosystem, we can imagine that trees in the vicinity of the pond cast shadows across the pond, limiting the exposure to sunlight on certain parts of the water surface. The growth of algae will thus be locally restricted since their only source of energy is photosynthesis. On the other hand, shadows can locally alter the competition between

predator fish and their prey due to the availability of hiding places. As before, the significance of this variability depends on the the length scale of variation, the typical length scale of the species interactions we are interested in and the length scale of species diffusion. A reef looks fairly homogeneous for the silver-tip shark hunting its prey, the grey reef shark. But the prey of the grey reef shark, smaller reef fishes, cephalopods and crustaceans among others [27], are small enough to find hiding places in various parts of the reef. Hence, variability of the reef environment probably plays a crucial role during their interaction and locally influences the probability of a successful predation process.

In most ecological models, the effects of environmental variability are assumed to only enter via a trivial renormalization of the coarse-grained reaction rates. But, as explained above, if the variation takes place on a similar length-scale as the interactions, its effects are not adequately captured by such a simplified description. In a spatial ecosystem model, we can describe spatial variability by making the reaction rates a random function of our spatial coordinates. It is impossible to retrieve the exact spatial distribution of rates for a given ecosystem, since the model rules are abstractions of the real processes. A good starting point is that the rates should vary around some well-defined average value. The disorder or variation strength would then be given by the second moment of a Gaussian distribution, a model parameter, much like the average values of the rates. Not knowing anything more about the environment, we can make the approximation that the rates are spatially uncorrelated, which makes all the higher moments of the distribution zero. Hence, our model description of environmental variability has at its core rates that are uncorrelated, Gaussian distributed quenched (fixed in time) random variables.

In the spatial stochastic Lotka-Volterra simulation model, environmental variability can be easily implemented by making the rates defining the stochastic process probabilities a property of the lattice sites. The values $\mu(\vec{x}_i)$, $\sigma(\vec{x}_i)$ and $\lambda(\vec{x}_i)$ (where \vec{x}_I represents the position of the lattice site i) are drawn from an appropriately chosen Gaussian distribution at the beginning of each simulation run. Details about the implementation are given in chapter 3. Our previous work on this model [28] confirmed the crucial role of environmental variability in the predation rate λ . We found that the densities of *both* predator and prey species increase by up to 24% as a function of the variation strength. Other quantities, such as the correlation lengths and the speed of activity fronts were influenced as well. Variability in the other rates μ and σ did not lead to significant changes in the system; see reference [28] and chapter 3 for a more in-depth discussion. Environmental variability has also been subsequently investigated in the context of cyclic models, particularly the three species rock-paper-scissors and May-Leonard models. The effects of spatial variations in the reaction rates on both of these models were surprisingly small, which indicates that cyclic three-species models seem to be robust against the introduction of environmental variability [8, 24]. The macroscopic properties of these systems are hardly modified by stochastic fluctuations in general.

Variability can also be considered in the context of variation between individual members of species. Due to differences in genetic heritage and learned strategies, the effectiveness with respect to various processes, such as reproduction, death or predation, can vary between

individuals of the same species. A larger-than-average tadpole is more visible, hence its probability of being preyed upon by a mosquito larva is probably greater than for an average-sized tadpole.

Hence, we can view the efficiency at certain processes as properties or traits of individual agents when modeling these systems. In our investigation, we focused again on the non-linear predation process and made the predation rate of a particular reaction between a predator and a prey particle a function of their respective predation efficacies. These predation efficacy values $\eta_{A/B}$ are numbers between zero and one and are assigned to new particles during the prey reproduction and predation processes. For predator particles, the interpretation of the assigned predation efficiency is straightforward: A higher value simply means that this particular predator particle is better at hunting prey. For prey particles, the meaning of the predation efficiency is more counter-intuitive: A higher value corresponds to a higher chance for the prey being consumed during a predation reaction. Hence, it is preferable for prey to have a low predation efficiency value. A more detailed discussion is given in chapter 2.

1.7 Evolutionary Dynamics

The investigation of individual or demographic variability directly leads into a discussion of population-level evolution and optimization of traits. It is reasonable to assume that offspring inherits certain abilities from their parents. These abilities can be derived from the genetic make-up that is inherited from parents (genes). They can also be strategies for food-gathering or hunting patterns, learned through imitation from their immediate social surroundings (memes). A combination of genes and memes determines a particular particle's efficiency at a given process, hence the more discrete nature of the genetic make-up and the presence or absence of certain strategies is smeared out. This coarse-grained interpretation of process efficiencies finally allows us to assume that the efficiency value of a given offspring particle will be in the vicinity of the parent particle. The severity of genetic mutations as well as the accuracy of strategy imitation between generations then determines the amount of inheritance variability of the coarse-grained efficiencies.

Applied to the previously discussed Lotka-Volterra system, this scheme allows for optimization of predation efficiencies at the level of species populations: A predator particle with a high predation efficiency will reproduce more often during its lifetime than a predator particle with a low efficiency. The predation efficiency of the offspring clusters around the parent efficiency, but the high-efficiency offspring particles will, again, reproduce more often. Hence we expect to see an increase in the predation efficiency of the whole predator population over time. A similar argument holds for the prey population. A more detailed discussion of this scheme is given in chapter 2 and reference [29].

Optimization and evolution in predator-prey system has been studied previously in experimental and theoretical contexts (using different models). Kishida *et al.* investigated recipro-

cal phenotype plasticity in salamanders and its prey, tadpoles. The gape of the salamander species adapted as a function of the body size of the tadpoles [30]. Yoshida *et al.* studied prey evolution in an experimental model using planktonic rotifers. They additionally modeled this system using a system of nonlinear differential equations [31]. Fort and Inchausti used an agent-based model that included a niche axis to study the emergence of biodiversity [32]. Rogers *et al.* used a niche model and applied a master equation expansion. They could show that demographic noise leads to the spontaneous formation of species [33]. Traulsen *et al.* investigated evolutionary dynamics in unstructured populations using a stochastic differential equations approach [34]. Weitz *et al.* studied the co-evolution of bacteria and bacteriophage via mean-field and stochastic models [35]. Our investigation was motivated in part by these previous studies. However, our focus is the influence of variability on systems that exhibit optimization effects.

Chapter 2

Demographic Variability

Parts of this chapter were adapted from our publication:

U. Dobramysl, U. C. Täuber, to appear in JSTAT (2013). “Copyright (2013) by the Institute of Physics.”

In this chapter, we focus on the effects of randomness in the properties of individual members of species. This *demographic* variability also opens up the possibility to include evolutionary dynamics in our model, as already discussed in the introductory chapter. I will give a more rigorous definition of the model under investigation in section 2.1. In section 2.2, I will derive the mean-field equations and discuss their steady-state solutions. Finally, section 2.3 deals with the results of stochastic simulations and a comparison with the mean-field solutions.

2.1 Model Rules

We use the Lotka-Volterra model as a basis for our study of individual variability, as we already discussed in chapter 1. In our model, particles of either species have an intrinsic property that describes their efficiency during predation reactions. More specifically, each particle carries a predation efficiency value η between zero and one. During a predation interaction between a predator particle with an efficiency value of η_A and a prey particle with a corresponding value of η_B , the predation rate is determined from the arithmetic mean of these efficiencies:

$$\lambda = \frac{1}{2}(\eta_A + \eta_B). \quad (2.1)$$

Consequently, a predator particle with a high predation efficacy has a higher chance of consuming a prey and reproducing and can be considered to be good at “hunting”. A prey particle with a low efficiency value is generally less likely to be consumed and hence can be considered to be good at “evading”. Note that this efficiency value η is different from the fitness value that is derived from a certain genotype, which is defined as the average

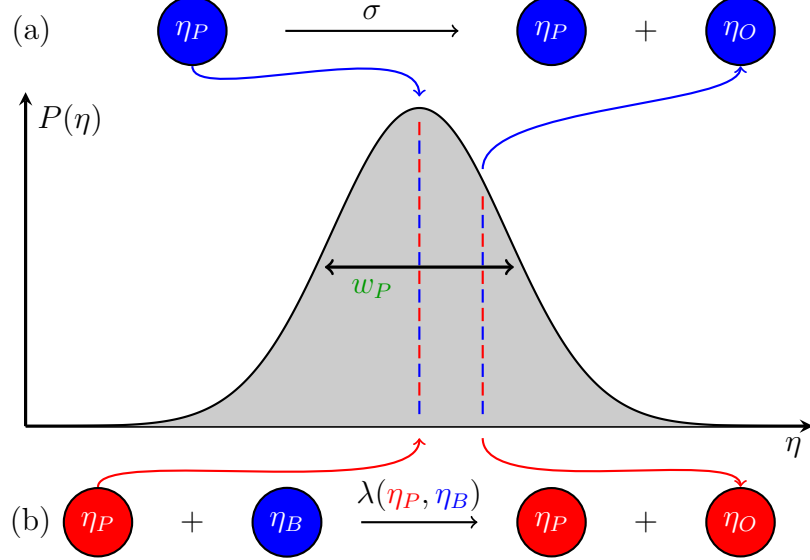


Figure 2.1: Inheritance model rules. (a) During prey reproduction, a parent particle spawns an offspring prey particle with a rate σ . The parent particle’s predation efficiency value η_P is used as the mean of a Gaussian distribution with a standard deviation of w_P , truncated to the interval between zero and one. The offspring’s efficiency value η_C is then drawn from this inheritance distribution. (b) During predation, a predator particle consumes a prey particle with a rate λ , a function of the participating particles’ predation efficiency values. A new offspring predator particle is created and its efficiency value η_O is determined via the same mechanism as is used in the case of prey reproduction. (*Adapted from reference [19], figure 5.*)

number of offspring. The predation efficiency is a mesoscopic continuous stochastic variable describing the combined effects of genetic makeup and learning of strategies on the hunting or evasion capabilities of an individual particle.

As discussed in section 1.7, we include inheritance and thus evolutionary dynamics in the predation efficiencies. I argued earlier that the predation efficiency value of an offspring particle is likely to be near the parent’s value. The prime goal of this work is to investigate the influence of variability, hence we need to be able to control the average efficiency deviation between generations (i.e. the mutation probability). This suggests the use of a symmetric probability distribution that exhibits a maximum around the parent particle’s efficiency value with a well-defined second moment.

Figure 2.1 shows how the predation efficiency is determined during the reproduction processes of prey and predator particles. The parent particle’s efficiency value η_P is used as the mean value of a Gaussian distribution, truncated to the interval $[0, 1]$. The offspring’s efficacy value η_O is then drawn from this inheritance distribution. The standard deviation of the Gaussian distribution (before truncation) serves as the measure of variability in this scheme.

It can also be viewed as the average severity of mutations from one generation to the next.

This variable inheritance of efficacies now allows for evolution of the hunting and evasion properties of the predator and prey populations. Selection processes due to the predation reaction will optimize the steady-state population distributions of both species. There is however an asymmetry between the optimization mechanisms of predators and prey, since the species interaction directly affects only the predator reproduction, whereas the prey population optimization happens through an indirect selection bias. We will discuss this further in section 2.3.

2.2 Doi-Peliti Formalism and Mean-Field Equations

In this section I systematically derive the mean-field equations for the Lotka-Volterra model with inheritance of efficiencies. I start by writing down the model's master equation, which describes the time evolution of the probabilities of the system's microscopic states. I then switch to a Fock-space equivalent formulation with particle creation and annihilation operators, which allows us to rewrite the master equation as an “imaginary-time Schrödinger equation.” This yields a Liouville (or pseudo-Hamiltonian) time evolution operator. I write down the coherent-state ‘action’ in terms of the ladder operator eigenvalues and finally arrive at the mean-field equations for the predator and prey particle numbers. The steady-state solutions can then be found numerically. Finally, I will show the exact solution in the case of a uniform inheritance distribution.

2.2.1 Master Equation

The master equation of a system with a discrete set of states, which are fully characterized by occupation numbers of single-particle states, governs the time evolution of the configuration probabilities of said states. For each possible reaction in the system, there exists a probability inflow term into a given state and an outflow term to a different state. Since this includes all of the possible states of our discrete system and the transitions between them, the master equation completely describes a stochastic system. It can, in principle, be solved to yield the probability distribution as a function of time for a given initial state. However, the number of states is generally large and hence exact numerical solutions of the master equation become next to impossible to find. Monte Carlo simulations offer an approximate solution, by sampling realizations of the system’s time evolution and hence approximating the resulting time-dependent probability distribution.

To construct the master equation of our LV-system with demographic variability and inheritance of a continuous efficiency variable, we need to find an equivalent system with a discrete set of states. To this end, we discretize the interval of possible predation efficiency values $0 \leq \eta \leq 1$ into N bins, with the bin midpoint values $\eta_i = (i+1/2)/N$, $i = 0 \dots N-1$. We then

consider a predator or prey particle with an efficacy value in the range $\eta_i - 1/2 \leq \eta < \eta_i + 1/2$ to belong to the predator or prey subspecies i . The probability for the system to be in a state with a collection of $\{n_0, \dots, n_{N-1}\} \equiv \{n\}$ particles of subspecies of type A and $\{m_0, \dots, m_{N-1}\} \equiv \{m\}$ particles of subspecies of type B at time t is given by $P(\{n\}, \{m\}, t)$. In the following, the notation $\{n_i + 1\}$ indicates that there are $\{n_0, n_1, \dots, n_i + 1, \dots, n_{N-1}\}$ particles in the collection.

We now start to gather the inflow and outflow terms of the LV reactions. The predator death process (1.1a) yields an inflow of probability from a state with one additional predator in subspecies i , $n_i + 1$, when a single predator dies, and an outflow if a predator dies in the current state. Hence, the change in the probability of a state due to the death of a predator is given by

$$\mu \sum_i [(n_i + 1)P(\{n_i + 1\}, \{m\}, t) - n_i P(\{n\}, \{m\}, t)],$$

which depends on the predator death rate μ , the number of predator particles in subspecies i and the probabilities of the respective states. Since the predator death can occur in any of the subspecies, we need to sum over all predator subspecies i .

The prey reproduction (1.1b) reaction is slightly more complicated: since this process involves the creation of a particle, we need to take the (imperfect) inheritance of rates into account. To this end, we introduce the reproduction probability $f(\eta_1, \eta_2)$ that a particle with predation efficiency η_1 produces offspring with efficiency η_2 . We do not make any assumptions about the shape of this probability distribution other than that it be symmetric under exchange of its arguments, and that it be properly normalized with $\int_0^1 d\eta_1 f(\eta_1, \eta_2) = 1$. In the following, we use the discretized form $f_{ij} = f(\eta_i, \eta_j)$. The creation of a prey particle then leads to a change in probability of

$$\sigma \sum_i \left[\sum_k (m_i - \delta_{ik}) f_{ik} P(\{n\}, \{m_k - 1\}, t) - m_i P(\{n\}, \{m\}, t) \right].$$

The first term describes the inflow of probability due to the creation of a prey particle in subspecies i by a parent particle in subspecies k . We need to sum over all prey subspecies k because a prey particle of any subspecies has a chance to produce offspring of a different subspecies, weighted by the reproduction probability f_{ik} and the number of particles that can reproduce.

For the predation reaction (1.1c) we need to calculate the particle-dependent predation rate and include the reproduction probability distribution due to the creation of predator offspring in this reaction. Since the predation rate is given as the mean of the predation efficiencies of both particles, see equation (2.1), we introduce the quantity $\lambda_{ij} = (\eta_i + \eta_j)/2$. The interaction between a predator and a prey particle then yields the change in the probabilities

$$\sum_{ij} \lambda_{ij} \left[\sum_k (n_i - \delta_{ik})(m_j + 1) f_{ik} P(\{n_k - 1\}, \{m_j + 1\}, t) - n_i m_j P(\{n\}, \{m\}, t) \right].$$

Probability flows into the current state when a predator in subspecies k is created and a prey in subspecies j is consumed by a predator in subspecies i , described by the first term. The outflow of probability is due to interaction of any predator or prey from subspecies i or j , respectively.

Gathering the inflow and outflow terms of all reactions, we finally arrive at the master equation of the LV system with demographic variability and evolutionary dynamics:

$$\begin{aligned} \frac{\partial}{\partial t} P(\{n\}, \{m\}, t) = & \mu \sum_i [(n_i + 1)P(\{n_i + 1\}, \{m\}, t) - n_i P(\{n\}, \{m\}, t)] \\ & + \sigma \sum_i \left[\sum_k (m_i - \delta_{ik}) f_{ik} P(\{n\}, \{m_k - 1\}, t) - m_i P(\{n\}, \{m\}, t) \right] \\ & + \sum_{ij} \lambda_{ij} \left[\sum_k (n_i - \delta_{ik})(m_j + 1) f_{ik} P(\{n_k - 1\}, \{m_j + 1\}, t) - n_i m_j P(\{n\}, \{m\}, t) \right] \end{aligned} \quad (2.2)$$

This differential equation completely describes the change of the probability distribution over time, starting from a known initial probability distribution $P(\{n\}, \{m\}, t_0)$. A possible choice for the initial probability distribution here is the Poisson distribution

$$P(\{n\}, \{m\}, t_0) = \left(\prod_i \frac{\bar{n}_0^{n_i}}{n_i!} e^{-\bar{n}_0} \right) \left(\prod_j \frac{\bar{m}_0^{m_j}}{m_j!} e^{-\bar{m}_0} \right), \quad (2.3)$$

with the mean initial predator and prey subspecies densities \bar{n}_0 and \bar{m}_0 .

2.2.2 Fock-space Equivalent Formulation and the Time Evolution Operator

Because we are dealing with a system that has a discrete set of particles in different states, and a state is completely characterized by the set of occupation numbers $\{n\}$ and $\{m\}$, a Fock space description in analogy to quantum mechanical oscillators is appropriate. The transition between states are uniquely identified by integer changes in the occupation numbers due to the reactions. Hence, we can introduce a general state $\phi(t)$ by writing

$$|\phi(t)\rangle = \sum_{\{n\}} P(\{n\}, \{m\}, t) |\{n\}, \{m\}\rangle, \quad (2.4)$$

where the $|\{n\}, \{m\}\rangle = \prod_i |n_i\rangle |m_i\rangle$ are the basis states of our system, weighted by the probability of each state and summed over all the possible states of the system.

By differentiating with respect to time and inserting the master equation (2.2) we arrive at

$$\begin{aligned} \frac{\partial}{\partial t} |\phi(t)\rangle &= \sum_{\{n\}} \sum_{\{m\}} |\{n\}, \{m\}\rangle \frac{\partial}{\partial t} P(\{n\}, \{m\}, t) = \\ &= \sum_{\{n\}} \sum_{\{m\}} |\{n\}, \{m\}\rangle \left(\mu \sum_i [(n_i + 1)P(\{n_i + 1\}, \{m\}, t) - n_i P(\{n_i\}, \{m\}, t)] \right. \\ &\quad \left. + \sigma \sum_i \left[\sum_k (m_i - \delta_{ik}) f_{ik} P(\{n_i\}, \{m_k - 1\}, t) - m_i P(\{n_i\}, \{m\}, t) \right] \right. \\ &\quad \left. + \sum_{ij} \lambda_{ij} \left[\sum_k (n_i - \delta_{ik})(m_j + 1) f_{ik} P(\{n_k - 1\}, \{m_j + 1\}, t) - n_i m_j P(\{n_i\}, \{m_j\}, t) \right] \right). \end{aligned}$$

To factor out the only time-dependent quantity, the probability density $P(\{n\}, \{m\}, t)$, we shift the summation over states and get

$$\begin{aligned} \frac{\partial}{\partial t} |\phi(t)\rangle &= \sum_{\{n\}} \sum_{\{m\}} P(\{n\}, \{m\}, t) \left(\mu \sum_i n_i [|\{n_i - 1\}, \{m\}\rangle - |\{n_i\}, \{m\}\rangle] \right. \\ &\quad \left. + \sigma \sum_i m_i \left[\sum_k f_{ik} |\{n_i\}, \{m_k - 1\}\rangle - |\{n_i\}, \{m\}\rangle \right] \right. \\ &\quad \left. + \sum_{ij} \lambda_{ij} n_i m_j \left[\sum_k f_{ik} |\{n_k + 1\}, \{m_j - 1\}\rangle - |\{n_i\}, \{m_j\}\rangle \right] \right) \end{aligned}$$

Now we introduce raising and lowering operators in complete analogy to a quantum mechanical harmonic oscillator or bosonic Fock states. We need two sets of operators, a_i , a_i^\dagger and b_i , b_i^\dagger for species A and B, respectively. The operators act on the states in the following manner

$$\begin{aligned} a_i^\dagger |\{n\}, \{m\}\rangle &= |\{n_i + 1\}, \{m\}\rangle \\ a_i |\{n\}, \{m\}\rangle &= n_i |\{n_i - 1\}, \{m\}\rangle \\ b_i^\dagger |\{n\}, \{m\}\rangle &= |\{n\}, \{m_i + 1\}\rangle \\ b_i |\{n\}, \{m\}\rangle &= m_i |\{n\}, \{m_i - 1\}\rangle \\ [a_i, a_j^\dagger] &= \delta_{ij} = [b_i, b_j^\dagger], \end{aligned} \tag{2.5}$$

guaranteeing that the ladder operators have integer eigenvalues. This procedure finally leads to an “imaginary-time Schrödinger equation” for the time evolution of a general state

$$\begin{aligned} \frac{\partial}{\partial t} |\phi(t)\rangle &= - \sum_i \left[\mu(a_i^\dagger - 1)a_i + \sigma \left(1 - \sum_k f_{ik} b_k^\dagger \right) b_i^\dagger b_i \right. \\ &\quad \left. + \sum_j \lambda_{ij} \left(b_j^\dagger - \sum_k f_{ik} a_k^\dagger \right) a_i^\dagger a_i b_j \right] |\phi(t)\rangle. \end{aligned} \tag{2.6}$$

Using the ansatz $|\phi(t)\rangle = \exp(-Ht) |\phi(0)\rangle$, we find the time evolution operator H (Liouville operator or non-Hermitian pseudo-Hamiltonian) for our system to be

$$H = \sum_i \left[\mu(a_i^\dagger - 1)a_i + \sigma \left(1 - \sum_k f_{ik} b_k^\dagger \right) b_i^\dagger b_i + \sum_j \lambda_{ij} \left(b_j^\dagger - \sum_k f_{ik} a_k^\dagger \right) a_i^\dagger a_i b_j \right]. \quad (2.7)$$

Note that one can get this result from the reaction Liouville operator of the standard LV system [18] by replacing $1 - b_i^\dagger \rightarrow 1 - \sum_k f_{ik} b_k^\dagger$ in the prey reproduction term, as well as $b_j^\dagger - a_j^\dagger \rightarrow b_j^\dagger - \sum_k f_{jk} a_k^\dagger$ and $\lambda \rightarrow \sum_j \lambda_{ij}$ (with the appropriate change in the indices) in the predator reproduction term, as one would expect.

2.2.3 Coherent-State 'Action' and Mean Field Equations

To calculate observables $\langle O(t) \rangle = \sum_{\{n\}} \sum_{\{m\}} O(\{n\}, \{m\}) P(\{n\}, \{m\}, t)$ one needs to introduce a projection state $\langle P | = \langle 0 | \prod_i e^{a_i} e^{b_i}$ with $\langle P | 0 \rangle = 1$ and $\langle P | a_j^\dagger = \langle P | = \langle P | b_j^\dagger$ due to $[e^{a_i}, a_j^\dagger] = e^{a_i} \delta_{ij}$ (and similarly for the b_i) [18]. We can then write observables as

$$\langle O(t) \rangle = \langle P | O(\{n\}, \{m\}) | \phi(t) \rangle. \quad (2.8)$$

Due to probability conservation $1 = \langle P | \phi(t) \rangle = \langle P | e^{-Ht} | \phi(0) \rangle$ must hold and hence, $\langle P | H = 0$ since $\langle P | \phi(0) \rangle = 1$, and thus $H(a_i, b_i, a_i^\dagger \rightarrow 1, b_i^\dagger \rightarrow 1) = 0$.

Next, we introduce ladder operator coherent states, well known from many-particle quantum mechanics. The right eigenstates of the predator annihilation operator a_i with eigenvalue α_i are $|\alpha_i\rangle = \exp(-|\alpha_i|^2/2 + \alpha_i a_i^\dagger) |0\rangle$, which can be easily checked by inserting into $a_i |\alpha_i\rangle = \alpha_i |\alpha_i\rangle$. These states are overcomplete in the sense that $\int \prod_i d\alpha_i^* d\alpha_i |\alpha_i\rangle \langle \alpha_i| = \pi$. An analogous set of right eigenstates can be introduced for the prey annihilation operator $b_i |\beta_i\rangle = \beta_i |\beta_i\rangle$. By repeatedly inserting the over-completeness relation of both sets of states into the time evolution (2.6) and therefore the time-dependent observable (2.8), and following the analysis done in reference [18] (described more generally in reference [36]), we arrive at a path integral expression for calculating averages:

$$\langle O(t) \rangle = N^{-1} \int \prod_i d\alpha_i^* d\alpha_i d\beta_i^* d\beta_i O(\{\alpha_i\}, \{\beta_i\}) \exp(-S[\{\alpha_i^*\}, \{\alpha_i\}, \{\beta_i^*\}, \{\beta_i\}, t]) \quad (2.9)$$

The normalization is determined by calculating the average of the unity operator $N = \int \prod_i d\alpha_i^* d\alpha_i d\beta_i^* d\beta_i e^{-S}$. The coherent state path integral 'action' (the exponential weight in

the path integral) then becomes

$$\begin{aligned} S[\{\alpha_i^*\}, \{\alpha_i\}, \{\beta_i^*\}, \{\beta_i\}, t] = & \sum_i \left(-\alpha_i(t) - \beta_i(t) - \bar{n}_0 \alpha_i^*(0) - \bar{m}_0 \beta_i^*(0) \right. \\ & + \int_0^t dt' \left[\alpha_i^* \frac{\partial \alpha_i}{\partial t'} + \beta_i^* \frac{\partial \beta_i}{\partial t'} + \mu(\alpha_i^* - 1)\alpha_i + \sigma \left(1 - \sum_k f_{ik} \beta_k^* \right) \beta_i^* \beta_i \right. \\ & \left. \left. + \sum_j \lambda_{ij} \left(\beta_j^* - \sum_k f_{ik} \alpha_k^* \right) \alpha_i^* \alpha_i \beta_j \right] \right). \end{aligned} \quad (2.10)$$

The terms in which the fields explicitly depend on the initial and final time stem from the coherent state normalization and can be safely ignored for averages and correlation functions that do not explicitly depend on these times, as is the case here. The variables \bar{n}_0 and \bar{m}_0 represent the average initial number of prey and predator particles in each subspecies, respectively, and originate in the initial Poisson distribution (2.3).

The classical equations of motion for the fields α_i^* , α_i , β_i^* and β_i are determined by using the steepest descent method, i.e. the minimum of S with respect to the fields. Hence we set the variation of S to zero:

$$\frac{\delta S}{\delta \alpha_i} = 0 = -\frac{\partial \alpha_i^*}{\partial t} + \mu(\alpha_i^* - 1) + \sum_j \lambda_{ij} \left(\beta_j^* - \sum_k f_{ik} \alpha_k^* \right) \alpha_i^* \beta_j \quad (2.11)$$

$$\frac{\delta S}{\delta \beta_i} = 0 = -\frac{\partial \beta_i^*}{\partial t} + \sigma \left(1 - \sum_k f_{ik} \beta_k^* \right) \beta_i^* + \sum_j \lambda_{ij} \left(\beta_i^* - \sum_k f_{jk} \alpha_k^* \right) \alpha_j^* \alpha_j \quad (2.12)$$

$$\frac{\delta S}{\delta \alpha_i^*} = 0 = \frac{\partial \alpha_i}{\partial t} + \mu \alpha_i + \sum_j \lambda_{ij} \left(\beta_j^* - \sum_k f_{ik} \alpha_k^* \right) \alpha_i \beta_j - \sum_{kj} \lambda_{ij} f_{ki} \alpha_k^* \alpha_k \beta_j \quad (2.13)$$

$$\begin{aligned} \frac{\delta S}{\delta \beta_i^*} = 0 = & \frac{\partial \beta_i}{\partial t} + \sigma \left(1 - \sum_k f_{ik} \beta_k^* \right) \beta_i - \sigma \sum_k f_{ki} \beta_k^* \beta_k + \sum_j \lambda_{ji} \alpha_j^* \alpha_j \beta_i \\ & + \sum_j \lambda_{ji} \left(\beta_i^* - \sum_k f_{ik} \alpha_k^* \right) \alpha_i^* \alpha_i \end{aligned} \quad (2.14)$$

Equations (2.11) and (2.12) are readily solved by $\alpha_i^* = 1 = \beta_i^*$, a consequence of probability conservation. Equations (2.13) and (2.14) then yield the classical equations of motion of the fields α_i and β_i . Since the predator and prey subspecies counts are $a_i(t) = \langle P | n_i | \phi(t) \rangle = \alpha_i(t)$ and $b_i(t) = \langle P | m_i | \phi(t) \rangle = \beta_i(t)$, we arrive at the mean-field rate equations of our system:

$$\frac{\partial a_i}{\partial t} = -\mu a_i + \sum_{jk} \lambda_{kj} f_{ki} a_k b_j \quad (2.15)$$

$$\frac{\partial b_i}{\partial t} = \sigma \sum_k f_{ki} b_k - \sum_j \lambda_{ji} a_j b_i. \quad (2.16)$$

These equations look very similar to the standard Lotka-Volterra mean-field equations (1.2). In fact, setting $f_{ij} = \delta_{ij}$ and $\lambda_{ij} = \lambda\delta_{ij}$, yields a set of standard LV mean-field equations for each subspecies i .

2.2.4 Steady-State Solutions

Steady-state solutions of mean-field equations (2.15) and (2.16) are determined by setting the time derivatives to zero: $\partial a_i(t)/\partial t = 0 = \partial b_i(t)/\partial t$. Therefore, the steady-state particle counts can always be found by numerically solving the implicit equations

$$\mu a_i = \sum_{jk} \lambda_{kj} f_{ki} a_k b_j \quad (2.17)$$

$$\sigma \sum_k f_{ki} b_k = \sum_j \lambda_{ji} a_j b_i, \quad (2.18)$$

using a self-consistent, iterative approach.

However, in the special case of a uniform inheritance distribution $f_{ij} = 1/N$, a closed form of the steady-state counts can be found. In this case, there is no correlation between the parent and offspring particle efficiencies, and the right side of equations (2.17) becomes independent of the index i . Consequently, the number of predators in bin i is constant and independent of i , hence $a_i = \text{const} = A$. Equation (2.18) can be rewritten as

$$\frac{b_i}{\sum_k b_k} = \frac{\sigma}{AN} \frac{2N}{\sum_j (i+j+1)}. \quad (2.19)$$

Summing both sides over i and using $\sum_j 1 = N$ and $\sum_j j = N(N-1)/2$, we arrive at the expression

$$\frac{AN}{2\sigma} = \sum_i \frac{1}{i + \frac{N+1}{2}}.$$

Using a difference equation involving the digamma function $\psi(x+N) - \psi(x) = \sum_i \frac{1}{i+x}$ yields

$$\frac{AN}{2\sigma} = \psi\left(\frac{3N+1}{2}\right) - \psi\left(\frac{N+1}{2}\right).$$

To arrive at a useful, approximate value of the constant A , we rewrite this expression as

$$\frac{AN}{2\sigma} = \ln\left(\frac{3N+1}{N+1}\right) + \frac{1}{3N+1} - \frac{1}{N+1} - \sum_{n=1}^{\infty} \frac{2^{2n-1} B_{2n}}{n} \left[\frac{1}{(3N+1)^{2n}} - \frac{1}{(N+1)^{2n}} \right],$$

where we used the asymptotic series expansion of the digamma function

$$\psi(x) = \ln x + \frac{1}{2x} - \sum_{n=1}^{\infty} \frac{B_{2n}}{2nx^{2n}}$$

(B_k is the k -th Bernoulli number). Hence, in the limit of large N , the constant simplifies to

$$\lim_{N \rightarrow \infty} \frac{AN}{2\sigma} = \ln 3.$$

Defining the subspecies densities as $\rho_{a,i} = a_i / \sum_j a_j$ and $\rho_{b,i} = b_i / \sum_j b_j$, and using equation (2.19), as well as the definition of the efficiency bins $\eta_i = (i + 1/2)/N$, we finally arrive at

$$\rho_a = \frac{1}{N}, \quad \rho_{b,i} = \frac{2}{N \ln 3} \frac{1}{1 + 2\eta_i}, \quad (2.20)$$

which is valid in the limit of large N ($N = 100$ proved to be sufficiently large). Hence, the predator density becomes constant and independent of the subspecies index i . The prey density exhibits a selection bias towards low values of the efficiency η .

2.3 Population Distributions from Simulations

We are now ready to perform Monte Carlo simulations of our system. Our main goal in this section is to extract the predator and prey population distributions as a function of the particle efficiencies. To this end, we introduce efficiency bins $\eta_i = (i + 1/2)/N$, $i = 0, \dots, N - 1$ in complete analogy to the derivation of the master equation in section 2.2.1. We then count the number of particles a_i and b_i in the interval $[\eta_i - 1/(2N), \eta_i + 1/(2N)]$ and calculate the densities $\rho_{A,i} = a_i / \sum_j a_j$ and $\rho_{B,i} = b_i / \sum_j b_j$. The resulting histograms approximate the population distributions as a function of the efficacies.

Our simulations start by assigning all particles an initial predation efficiency of $\eta_{A/B} = 0.5$. Hence the population distributions for $t = 0$ exhibit a sharp peak at $\eta = 0.5$ and are zero everywhere else. This choice is mainly due to computational convenience, since the final steady-state population distributions do not depend on the initial state of the system. We checked this statement by varying the initial distribution of particles in efficiency space. There of course exist initial conditions in which the probability of one or both of the species to go extinct is rather high. Since we are interested only in (quasi-)steady states that exhibit species co-existence during the observation time, we exclude those initial conditions from our considerations. The simulations in this section are zero-dimensional, except where noted differently, meaning that there is no spatial lattice over which particles can hop from site to site. Since there are no spatial correlations, we can be confident that our previously derived mean-field equations for the steady state (2.17) and (2.18) should constitute a fair estimate for the behavior of the stochastic simulation.

We let the system and thus the population distributions evolve over time. The predator and prey populations optimize their predation efficiency over many generations. Predators benefit from a higher efficacy value, because their average interaction and thus reproduction rate is higher. Hence, a predator with a high η is more likely to have more offspring, compared

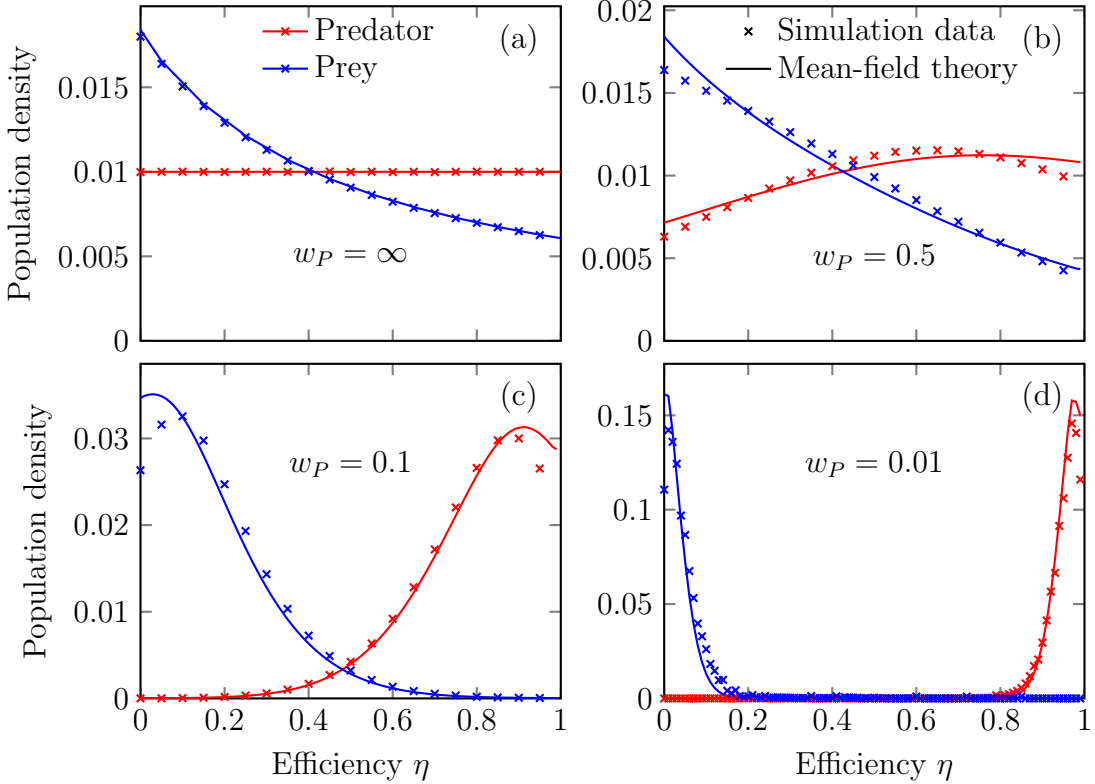


Figure 2.2: Population distributions for various values of the inheritance distribution width w_P . The red and blue curves indicate the predator and prey populations as a function of the efficiency, respectively. Curves with \times markers stem from zero-dimensional (well-mixed) simulations, while the solid lines show the mean-field theory predictions. (a) Population distribution for an uniform inheritance distribution with $w_P = \infty$. The prey population shows an inherent selection bias towards low η , while the predator population is flat. The mean-field theory prediction (2.20) exactly agrees with the simulation data. (b) Population distribution for a broad inheritance distribution with $w_P = 0.5$. The inherent selection bias of the prey population is still visible, but overlaid with the dynamic optimization towards low η . The predator population optimizes towards higher η and shows a maximum around $\eta \approx 0.65$. Our numeric mean-field theory solution agrees qualitatively. (c) Population distributions for a narrow inheritance distribution with $w_P = 0.1$. Both predator and prey populations optimized towards high and low values of η with maxima at $\eta \approx 0.9$ and $\eta \approx 0.1$ respectively. Mean-field theory over-estimates the optimization effects and places the population maxima slightly more towards the efficiency extrema. (d) Population distribution data for a sharply peaked inheritance distribution with $w_p = 0.01$. The maxima move even closer to the edges of the efficiency range. Simulation data displayed in this plot have been averaged over 1000 realizations. (Adapted from reference [19], figure 6.)

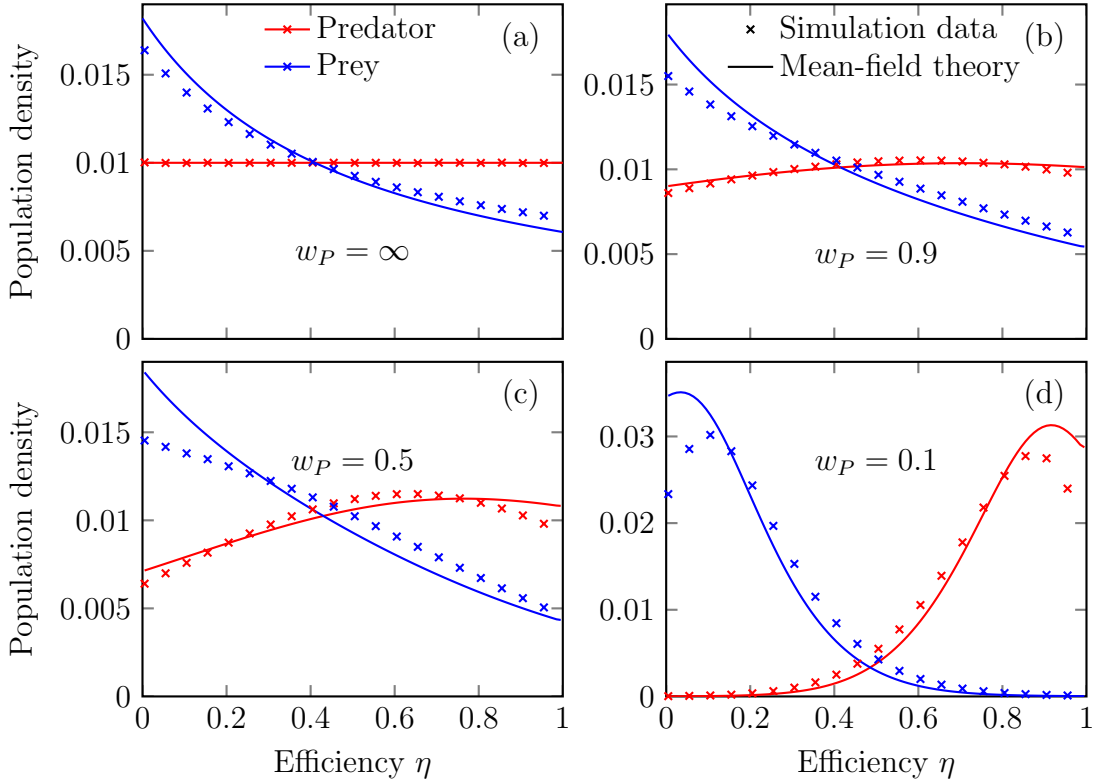


Figure 2.3: Population distributions for various values of the inheritance distribution width w_P from two-dimensional lattice simulations. The red and blue curves indicate the predator and prey populations as a function of the efficiency, respectively. Curves with \times markers stem from simulations, while the solid lines show the mean-field theory predictions. (a) Population distribution for an uniform inheritance distribution with $w_P = \infty$. The mean-field prediction for the prey population (2.20) ignores spatial correlations and thus over-estimates the prey selection bias in this case. (b-d) Population distributions for a broader inheritance distributions with $w_P = 0.9, 0.5, 0.1$, respectively. The mean-field prediction deviates more strongly from the simulation data than in the case of well-mixed zero-dimensional simulations. Simulation data displayed in this plot have been averaged over 10000 realizations with a lattice size of 128×128 . (*Adapted from reference [19], figure 7.*)

to a low- η predator particle, which in turn inherits this high η value. This yields an overall optimization of the predator population towards high efficiency values. Prey particles on the other hand benefit from low predation efficiency values, because their average lifetime is longer than prey particles with high η . Hence a low η yields a larger number of offspring particles and, accordingly, the same optimization as for the predator population occurs, only towards low η values. This dynamic, evolutionary optimization finally leads to a steady-state distribution of particles when the distance of the population maxima from the efficiency-edges $\eta = 0, 1$ is balanced by the finite width of the inheritance distribution.

Figure 2.2 displays the population density as a function of the efficiency η for various values of the inheritance distribution width w_P . The special case of an infinite width $w_P = \infty$ is shown in figure 2.2(a). In this situation, no correlation exists between the efficiency values of a parent- and its offspring particles and the efficiency assignment during reproduction is completely random. Consequently, the predator population distribution is flat and independent of η , as predicted by our mean-field theory result (2.20). The prey population distribution shows an inherent selection bias towards low values of η . A low efficiency in a prey particle means that it is more likely to live longer than a prey particle with a higher efficiency, according to our formula for the predation rate (2.1). Hence, at any given time when the system is in the (quasi-)steady state, there needs to be a higher number of prey particles in the low-efficiency bins than in the higher ones. This result and the simulation data agrees perfectly with our mean-field theory result (2.20) as well, without any fit parameters.

For non-uniform inheritance distribution, evolutionary optimization of the predator and prey populations takes place. Figure 2.2(b) shows the population distribution for $w_P = 0.5$. In this case, the effects of the inherent prey selection bias are still visible and no clear prey population maximum is visible. The predator population exhibits a maximum at $\eta \approx 0.65$ due to the balancing of dynamic optimization and the finite width of the inheritance distribution. The numerical, self-consistent solution of our mean-field theory agrees qualitatively but over-estimates the effects of optimization. At an even smaller inheritance distribution width of $w_P = 0.1$, the predator and prey population distributions, displayed in figure 2.2(c), form clear maxima at high and low values of η , respectively. Again, the numerical mean-field predictions over-estimate optimization effects and place the population maxima nearer to the efficiency edges $\eta = 0, 1$. A sharply peaked inheritance distribution with $w_P = 0.01$ yields population maxima even closer to the edges of the efficiency range, as shown in 2.2(d).

It should be noted that two-dimensional lattice simulations yield quantitatively slightly different predator and prey population distributions. Emerging spatial correlations influence the results as shown in figure 2.3. Since mean-field theory ignores spatial correlations, our solution already over-estimates the prey selection bias in the two-dimensional model, but is still qualitatively correct. A similar trend is noticeable for finite values of the inheritance distribution width w_P .

Chapter 3

Spatial vs. Demographic Variability

We now introduce *spatial* randomness in addition to demographic variability, which we discussed in the last chapter. We want to clarify the importance of both types of variability in the interaction rate. To this end, we need to introduce a new control parameter that makes it possible to tune the relative influence of environmental and demographic randomness. This can be motivated by thinking of different layers in an oceanic ecosystem. At shallow depths, spatial variability is weak or non-existent, since the water surface is very homogeneous. Near the ocean floor however, variations of the geography need to be taken into account. As in our previous publication on purely spatial variability [28], we then measure the (quasi-)steady-state density as a function of variability and spatial influence. Finally, we discuss the influence of variability on the stability of our predator-prey ecosystem.

The remainder of this chapter was adapted from our publication:

*U. Dobramysl, U. C. Täuber, Phys. Rev. Lett. **110** 048105 (2013). “Copyright (2013) by the American Physical Society.”*

3.1 Model

Since we wish to address the distinctions between internal and spatial randomness, we introduce in addition environmental variability by assigning a spatial predation efficacy value η_S to each lattice site, drawn from a normalized Gaussian distribution with fixed mean 0.5 and standard deviation w_S , truncated to $[0, 1]$, and set to be fixed in time. The ensuing predation rate λ is a random variable as well, namely a function of both the spatial efficiency at the lattice site the reaction occurs on and the two individual predation efficacies of the participating predator and prey particles. We finally define a model parameter ζ that describes the relative importance of the spatial over individual efficacies:

$$\lambda = \zeta \eta_S + (1 - \zeta) (\eta_A + \eta_B)/2. \quad (3.1)$$

3.2 Steady-State Particle Density

To quantify the influence of variability, and in particular the distinction between individual (internal) variability and spatial environmental randomness, we measured its impact on the (quasi-)steady-state particle density for both species. Figure 3.1(a) displays the relative change of the predator density $\rho_A(w_S, w_P)$ over the zero-variability case as a function of w_S and w_P for $\zeta = 0.3$. Both types of variability contribute additively and positively to the density enhancement. Figure 3.1(b) shows the relative density change as a function of $w = w_S = w_P$ and ζ . The prey density shows the same quantitative behavior for all parameter ranges. Hence we observe a significant increase of the population densities of *both* species for higher variability not only for purely spatial ($\zeta = 1$) randomness [28], but also for individual variability ($\zeta = 0$). In contrast, the effect of spatial randomness in either the prey birth rate σ or the predator death rate μ on the species densities stayed below a rather low value of 2%.

The striking minimum in the density increase occurring near a spatial influence factor $\zeta = 0.3$ arises from the combined variabilities through the quenched randomness of the lattice and the emergent variability of the individual particles. We argue that the density increase is primarily a monotonic function of the variability in the predation rate λ . Using the dependence of the predation rate λ on the spatial predation efficacy value η_S and the predation efficiencies of the participating particles η_A and η_B given in the text, the standard deviation of λ is $\sigma_\lambda = \sqrt{\zeta^2 \sigma_S^2 + (1 - \zeta)^2 (\sigma_A^2 + \sigma_B^2)/2}$. Due to the truncation of predation efficiency values to the range $[0, 1]$, the effective standard deviation of the spatial predation efficacy is different from the environmental variability parameter. Similarly, the standard deviation of the predation efficiencies of individual particles has to be taken from simulation data. Figure 3.1(c) shows the resulting standard deviation of λ as a function of w and ζ which is a measure of the effective combined variability. It reflects the minimum in the density increase at $\zeta \approx 0.3$. The data also emphasize that environmental variability has a more pronounced effect on the species densities as compared to demographic variability, since the density increase is disproportionately higher for $\zeta \rightarrow 1$.

Surprisingly, we observe that low individual variability with weak or no spatial influence, i.e. $0 < w_P \ll 1$ and $\zeta = 0$, yields the strongest species optimization with the maxima of the predator and prey populations closest to $\eta = 1$ and $\eta = 0$ respectively; see Fig. 2.2(a). But the enhancement of the overall species densities in this regime is minute and tends to zero for small w_P ; see the lower right corner of Fig. 3.1(b). The respective benefits of the up- / downward optimization of the predator / populations in terms of predation efficiency clearly almost cancel each other. Hence we conclude that predation efficiency optimization is essentially neutral and carries no benefit for either species in terms of their net population densities (at least in the context of our model), despite its vital necessity to ensure the survival of co-evolving species. This also reinforces our argument that the density enhancement is a function of rate variability only.

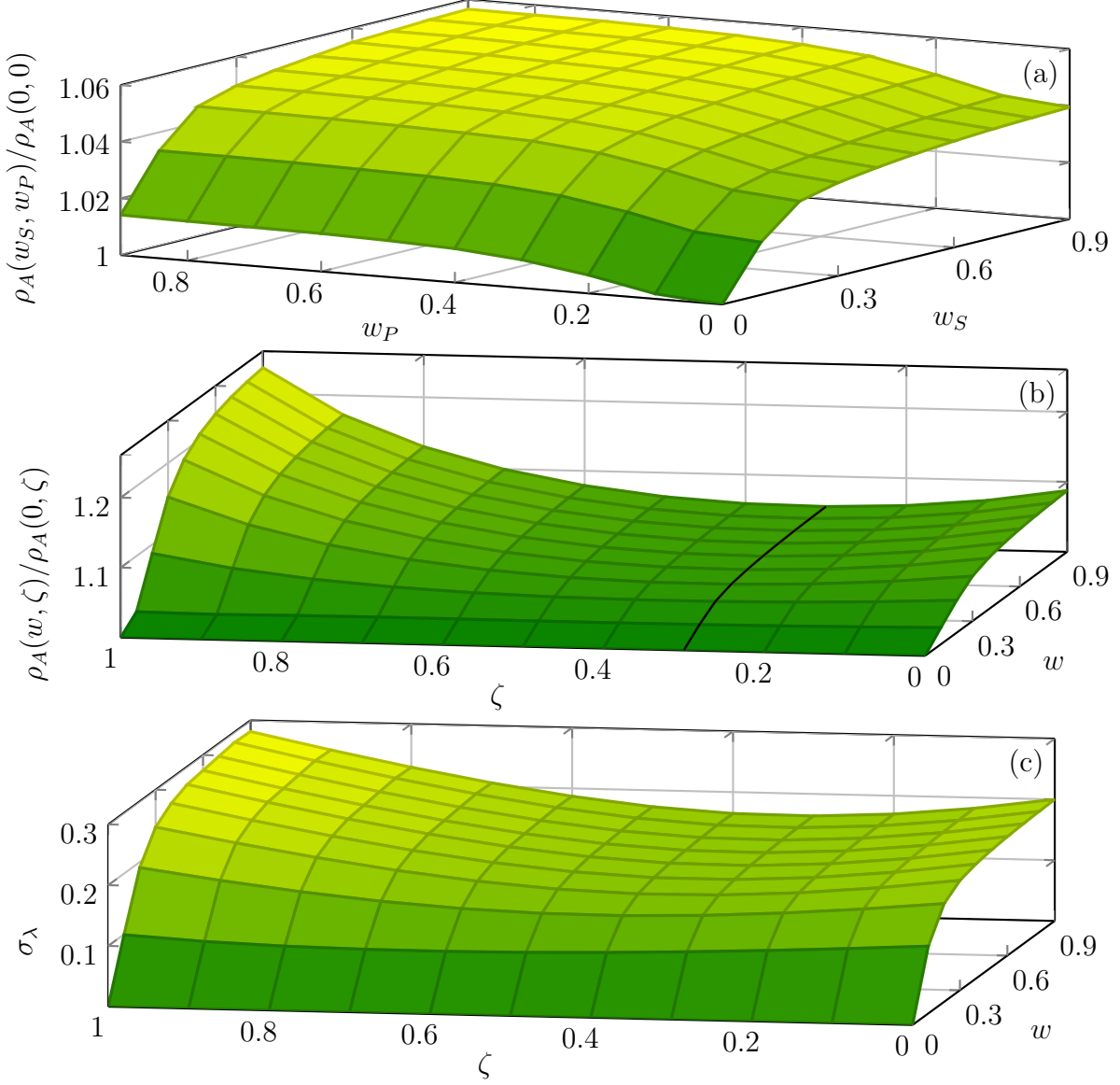


Figure 3.1: The (quasi-)steady-state predator density as a function of spatial and individual variability, as well as variability and spatial influence. (a) The (quasi-)steady-state predator density ρ_A as a function of the spatial and individual variability w_S and w_P for $\zeta = 0.3$. The black line represents the slice of equal spatial and individual variability $w_S = w_P$ from the minimum in (b). (b) The predator density shows a consistent increase for all values of the spatial variability influence ζ as function of equal variabilities $w = w_S = w_P$ over a system with zero variability. A remarkable minimum is observed near $\zeta = 0.3$ (black line). (c) The standard deviation of the predation rate σ_λ , calculated via error propagation from the spatial and individual predation efficiency distributions. Results in this figure represent an ensemble average over 10000 realizations on a lattice of size 128×128 . (*Adapted from reference [29], figure 3.*)

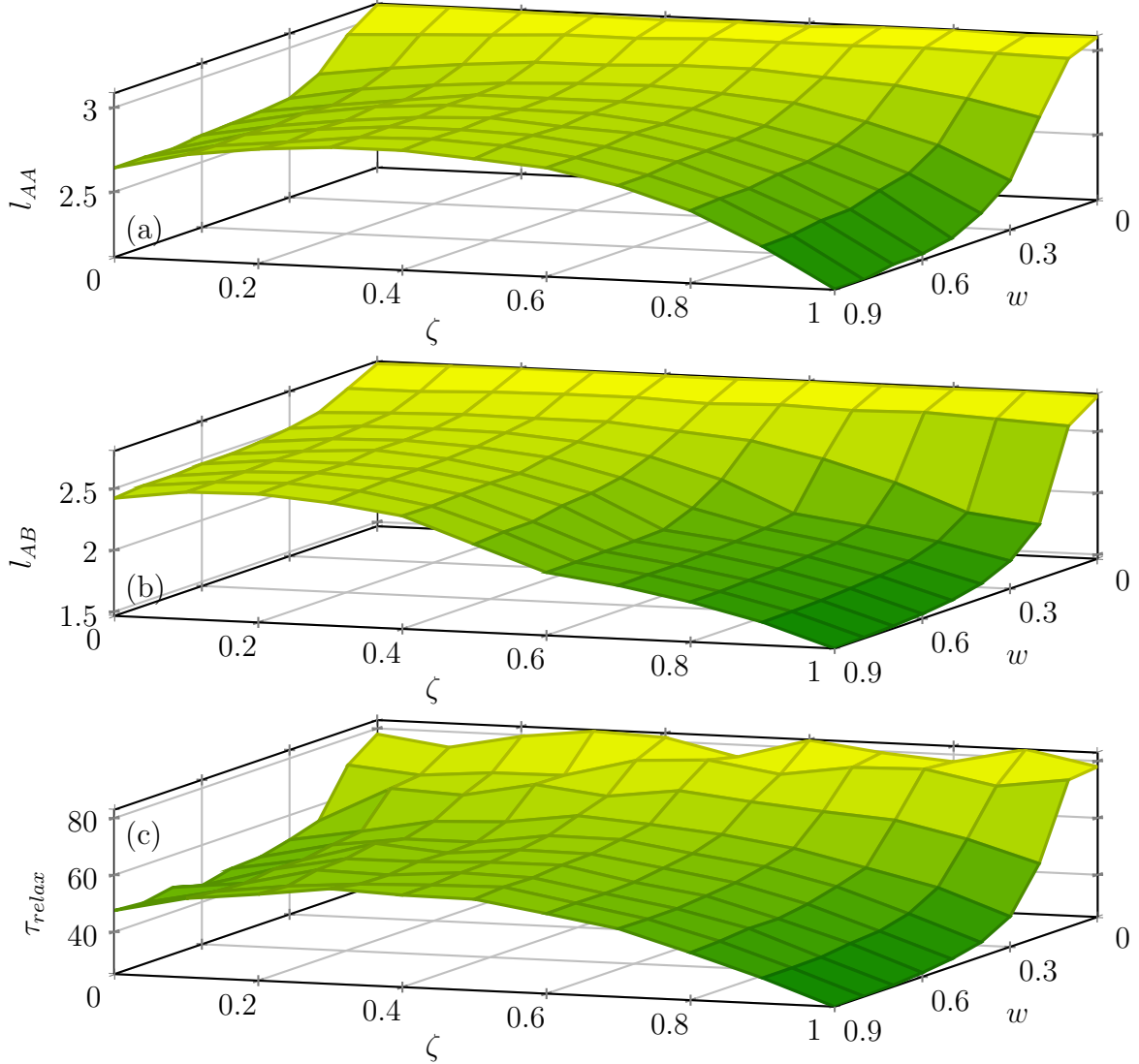


Figure 3.2: Correlation lengths and relaxation time as a function of variability. (a) The autocorrelation length l_{AA} and (b) the cross-correlation length l_{AB} from the predator-predator autocorrelation function. The prey-prey correlation length l_{BB} would essentially display the same shape as l_{AA} scaled by ~ 0.9 . (c) The predator density relaxation time τ_{relax} toward the quasi-stationary state. Results in this figure represent an ensemble average over 10000 realizations on a lattice of size 128×128 . (*Adapted from reference [29], figure 4.*)

The predator-predator and prey-prey correlation lengths l_{AA} and l_{BB} and typical predator-prey distance l_{AB} , measured by extracting the (quasi-)steady-state exponential decay length and the position of the maximum (in the case of l_{AB}) from the correlation functions $C_{\alpha\beta}(x) = \langle n_{\alpha i+x} n_{\beta i} \rangle - \rho_\alpha \rho_\beta$ with $\alpha, \beta = A, B$, decrease for increasing variability w ; see Fig. 3.2(a). For $\zeta = 1$ we reproduce the data from Ref. [28], where we argued that the decrease in $l_{\alpha\beta}$ indicated a more tightly clustered population around lattice sites with small spatial predation efficiency η_S , leading to the observed enhanced densities and higher amplitudes in the initial population oscillations. Surprisingly we also see a (less pronounced) decrease of $l_{\alpha\beta}$ for $\zeta \rightarrow 0$, indicating the existence of spontaneously formed tight activity patches around clusters of highly optimized prey particles. To investigate the effect of the combined variability on the relaxation of the population densities we collected data on the characteristic decay time of the initial predator population oscillations by least-square fitting of an exponentially decaying sinusoidal function to the predator species density time series; see Fig. 3.2(b). As expected, increasing disorder w induces a roughly threefold decrease in the purely spatial case ($\zeta = 1$) and about a twofold decrease in the individual variability case ($\zeta = 0$).

3.3 Extinction Statistics

In finite stochastic systems with an absorbing state (here, predator extinction), fluctuations will eventually drive the system into the absorbing state, as discussed in section 1.4 and reference [20]. This can be exploited to gain information about the stability of our model against the extinction of either species as a function of the model parameters. To this end, we simulated small systems, with a lattice size of 10×10 sites until the number of particles of either the prey or the predator species reaches zero, and collected the simulation time up to this event into extinction time histograms. The normalized extinction event count then corresponds to the extinction event probability $P_e(t)$.

We collected extinction histograms for small systems (lattice size 10×10 sites) to determine the influence of individual variability on the stability of the population. Figure 3.3(a) shows the extinction data for selected values of the variability w_P . The histograms show that the extinction probabilities are consistent with an exponential tail of the distribution in the long-time limit [37]. For increasing variability, the extinction event distributions become increasingly broader. Figure 3.3(b) shows the mean extinction time $t_e = \sum_{t=0}^{\infty} t P_e(t)$ and its standard deviation $\sigma_e = \sqrt{\sum_{t=0}^{\infty} (t - t_e)^2 P_e(t)}$ as a function of the inheritance distribution widths w_P . The mean extinction time is enhanced by a factor of up to ≈ 4.5 due to individual variability. This, together with the increase in σ_e , indicates that a higher number of realizations of our small system survive for longer times. Hence, we conclude that individual variability renders our model more robust against extinction.

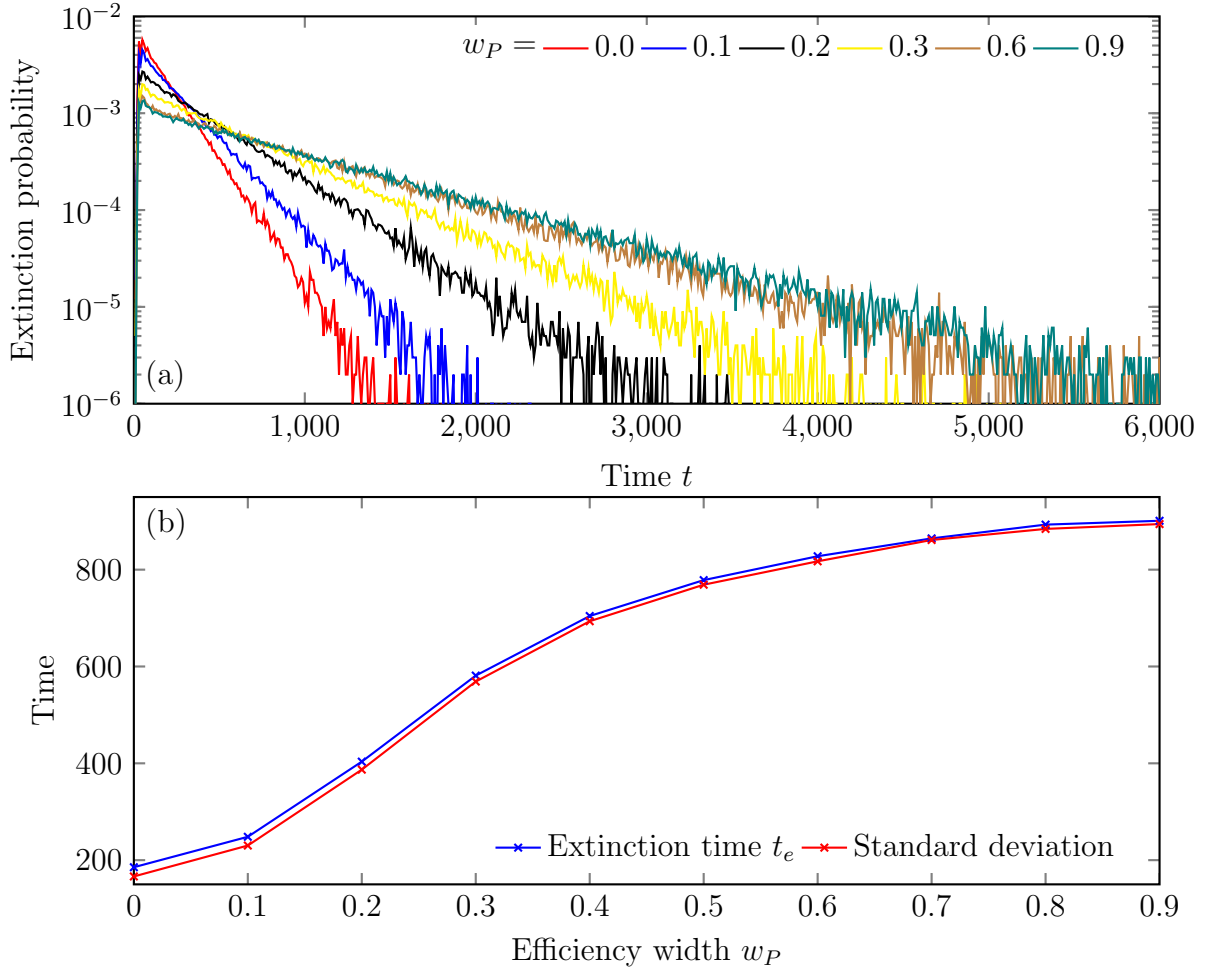


Figure 3.3: Extinction time probability and mean extinction time in a small system of 10×10 lattice sites as a function of individual variability w_P . Only individual efficiencies are considered here, hence ζ . (a) Normalized extinction event histograms as a function of time for different widths of the efficiency inheritance distribution w_P . In the case of no variability $w_P = 0$, extinction events are mostly confined to the time regime $t < 1000$. For higher values of w_P the tail of the extinction event distribution moves to longer times and becomes increasingly broader. (e) The mean extinction time t_e (blue) shows a more than four-fold increase as a function of the variability w_P . Its standard deviation (red) has approximately the same value as t_e , which is consistent with an exponential long-time tail. The data presented in this figure represent an average over 100000 realizations. (Adapted from reference [19], figure 10.)

Chapter 4

Conclusions

In the previous chapters, I discussed and analyzed our modifications of the standard Lotka-Volterra predator-prey model. I first introduced demographic variability by attaching a predation efficiency value to the individual predator and prey particles that determines the probability of a successful predation reaction between two such particles. In addition, these efficiency values are assigned in a way that enables dynamic, evolutionary optimization during reproduction processes. We introduced a measure of demographic variability, the width of the inheritance distribution, which can also be identified as a measure of the mutation probability during reproduction processes.

We derived a mean-field theory for this model to predict the predator and prey population distributions as a function of the predation efficiency. To this end, I first introduced the model’s master equation and subsequently constructed the model’s Liouville operator via the Doi-Peliti formalism. I then introduced the field-theoretic “action” of a coherent-state path integral formulation, from which we systematically found the mean-field equations for the population distributions. In the special case of an uniform inheritance distribution, it was possible to find a closed solution of these equations, which predicts an inherent selection bias for the prey population toward low efficiency.

Subsequently, I presented data from zero-dimensional, well-mixed simulations for several values of the inheritance distribution width, i.e. different variability. The population distributions for the case of a uniform inheritance distribution exactly matched the analytic solution of the mean-field theory. Finite values of the inheritance distribution width yield dynamic optimization of the predator and prey populations towards high and low efficiency values, respectively. The steady-state population distribution is determined by the balance between optimization pressure and variability. Thus, our model does not lead to fixation of a population at extreme values of the efficiency axis, in contrast to discrete genetic drift models [38].

In chapter 3, I presented our spatial, two-dimensional simulations, in order to implement

quenched spatial randomness in addition to individual variability in the predation efficiencies. By introducing a control parameter, the spatial importance factor, we were able to tune the system between purely spatial efficiency and purely individual efficiency. We found a marked enhancement of the steady-state densities of both species over the simple Lotka-Volterra system without variability, similar to our previous result for purely spatial variability [28]. Evolutionary optimization of the population densities proved to be essentially neutral in terms of the steady-state densities, but necessary for species survival. Finally, we analyzed the stability of small populations against extinction and found that an increase of individual variability rendered the system more stable.

While of course not directly applicable to real ecological systems, our results are nevertheless important for the analysis of larger food webs and evolutionary dynamics in multi-species settings. The effects of variability in the predation rate need to be investigated in these more complicated models. The cyclic three species rock-paper-scissors game for example does not show the same enhancements due to spatial variability [8], except in the limit of highly asymmetric rates, in which the Lotka-Volterra model is recovered [10]. More research is needed to clarify the conditions under which variability plays an important role or under which its effects are suppressed. The neutrality of evolutionary optimization of predation efficiencies, discussed in chapter 3.2, is a surprising result and also needs further investigation.

This project allows for a multitude of possible extensions. We already performed preliminary studies in two promising directions:

- **Rates other than the predation rate can be subjected to variability.** We investigated systems in which the hopping probability was a property of individual particles and hence subject to demographic variability. Our preliminary results show the formation of interesting meta-stable spatial structures and the emergence of a predator-extinction threshold.
- **The introduction of a second prey species with a different mutation speed.** Indirect competition of two prey species due to the asymmetric consumption by the predator can lead to interesting dynamic scenarios and effects on the extinction probability of both prey species.

Chapter 5

Bibliography

- [1] R. May. *Stability and complexity in model ecosystems*. Vol. 6. Princeton, NJ, Princeton University Press (1973) (cit. on p. 4).
- [2] J. Smith. *Models in ecology*. Cambridge, Cambridge University Press (1974), p. 145 (cit. on p. 4).
- [3] J. D. Murray. *Mathematical Biology*. 3rd ed. Vol. I and II. New York, Springer (2002) (cit. on pp. 4, 10).
- [4] J. Hofbauer and K. Sigmund. *Evolutionary Games and Population Dynamics*. Cambridge, Cambridge University Press (1998) (cit. on p. 4).
- [5] A. Mokany. “Impact of tadpoles and mosquito larvae on ephemeral pond structure and processes”. *Marine and Freshwater Research* **58** 436 (2007) (cit. on p. 4).
- [6] L. Blaustein and J. Margalit. “Mosquito larvae (*Culiseta longiareolata*) prey upon and compete with toad tadpoles (*Bufo viridis*)”. *Journal of Animal Ecology* **63** 841–850 (1994) (cit. on p. 4).
- [7] L. Blaustein and J. Margalit. “Priority Effects in Temporary Pools: Nature and Outcome of Mosquito Larva-Toad Tadpole Interactions Depend on Order of Entrance”. *Journal of Animal Ecology* **65** 77–84 (1996) (cit. on p. 4).
- [8] Q. He, M. Mobilia, and U. C. Täuber. “Spatial rock-paper-scissors models with inhomogeneous reaction rates”. *Physical Review E* **82** 051909 (2010) (cit. on pp. 5, 13, 36).
- [9] T. Reichenbach, M. Mobilia, and E. Frey. “Mobility promotes and jeopardizes biodiversity in rock-paper-scissors games”. *Nature* **448** 1046–9 (2007) (cit. on pp. 5, 10).
- [10] Q. He, U. C. Täuber, and R. K. P. Zia. “On the relationship between cyclic and hierarchical three-species predator-prey systems and the two-species Lotka-Volterra model”. *The European Physical Journal B* **85** 141 (2012) (cit. on pp. 5, 36).

- [11] S. O. Case, C. H. Durney, M. Pleimling, and R. K. P. Zia. “Cyclic competition of four species: Mean-field theory and stochastic evolution”. *Europhysics Letters* **92** 58003 (2010) (cit. on p. 5).
- [12] C. H. Durney, S. O. Case, M. Pleimling, and R. K. P. Zia. “Stochastic evolution of four species in cyclic competition”. *Journal of Statistical Mechanics: Theory and Experiment* **2012** P06014 (2012) (cit. on p. 5).
- [13] A. Roman, D. Konrad, and M. Pleimling. “Cyclic competition of four species: domains and interfaces”. *Journal of Statistical Mechanics: Theory and Experiment* **2012** P07014 (2012) (cit. on p. 5).
- [14] R. K. P. Zia. “General Properties of a System of S Species Competing Pairwise”. *arXiv:1101.0018* (2010) (cit. on p. 5).
- [15] A. J. Lotka. “Undamped oscillations derived from the law of mass action.” *Journal of the American Chemical Society* **42** 1595–9 (1920) (cit. on p. 5).
- [16] V. Volterra. “Variazioni e fluttuazioni del numero d’individui in specie animali conviventi”. *Mem. Accad. Sci. Lincei.* **2** 31–113 (1926) (cit. on p. 5).
- [17] T. Royama. “A comparative study of models for predation and parasitism”. *Researches on Population Ecology* **13** 1–91 (1971) (cit. on p. 6).
- [18] U. C. Täuber. “Population oscillations in spatial stochastic Lotka-Volterra models: a field-theoretic perturbational analysis”. *Journal of Physics A: Mathematical and Theoretical* **45** 405002 (2012) (cit. on pp. 7, 22).
- [19] U. Dobramysl and U. C. Täuber. “Environmental vs demographic variability in stochastic predator-prey models”. *Journal of Statistical Mechanics: Theory and Experiment* **to appear** (2013) (cit. on pp. 7, 8, 11, 17, 26, 27, 34).
- [20] M. Mobilia, I. T. Georgiev, and U. C. Täuber. “Phase Transitions and Spatio-Temporal Fluctuations in Stochastic Lattice Lotka-Volterra Models”. *Journal of Statistical Physics* **128** 447–483 (2007) (cit. on pp. 8, 9, 12, 33).
- [21] M. J. Washenberger, M. Mobilia, and U. C. Täuber. “Influence of local carrying capacity restrictions on stochastic predator-prey models”. *Journal of Physics: Condensed Matter* **19** 065139 (2007) (cit. on pp. 8, 11, 12).
- [22] A. J. McKane and T. J. Newman. “Predator-Prey Cycles from Resonant Amplification of Demographic Stochasticity”. *Physical Review Letters* **94** 218102 (2005) (cit. on p. 10).
- [23] S. Dunbar. “Travelling wave solutions of diffusive Lotka-Volterra equations”. *Journal of Mathematical Biology* **17** 11–32 (1983) (cit. on p. 10).
- [24] Q. He, M. Mobilia, and U. C. Täuber. “Coexistence in the two-dimensional May-Leonard model with random rates”. *The European Physical Journal B* **82** 97–105 (2011) (cit. on pp. 10, 13).

- [25] T. Reichenbach, M. Mobilia, and E. Frey. “Self-organization of mobile populations in cyclic competition.” *Journal of Theoretical Biology* **254** 368–83 (2008) (cit. on p. 10).
- [26] M. Mobilia, I. T. Georgiev, and U. C. Täuber. “Fluctuations and correlations in lattice models for predator-prey interaction”. *Physical Review E* **73** 040903(R) (2006) (cit. on p. 12).
- [27] C. Bester. *Grey Reef Shark. Education - Biological Profiles*. URL: <http://www.flmnh.ufl.edu/fish/Gallery/Descript/GReefShark/GReefShark.html>
- [28] U. Dobramysl and U. C. Täuber. “Spatial Variability Enhances Species Fitness in Stochastic Predator-Prey Interactions”. *Physical Review Letters* **101** 258102 (2008) (cit. on pp. 13, 29, 30, 33, 36).
- [29] U. Dobramysl and U. C. Täuber. “Environmental versus Demographic Variability in Two-Species Predator-Prey Models”. *Physical Review Letters* **110** 048105 (2013) (cit. on pp. 14, 31, 32).
- [30] O. Kishida, Y. Mizuta, and K. Nishimura. “Reciprocal phenotypic plasticity in a predator-prey interaction between larval amphibians”. *Ecology* **87** 1599–1604 (2006) (cit. on p. 15).
- [31] T. Yoshida, L. E. Jones, S. P. Ellner, G. F. Fussmann, and N. G. Hairston. “Rapid evolution drives ecological dynamics in a predator-prey system.” *Nature* **424** 303–6 (2003) (cit. on p. 15).
- [32] H Fort and P Inchausti. “Biodiversity patterns from an individual-based competition model on niche and physical spaces”. *Journal of Statistical Mechanics: Theory and Experiment* **2012** P02013 (2012) (cit. on p. 15).
- [33] T. Rogers, A. J. McKane, and A. G. Rossberg. “Demographic noise can lead to the spontaneous formation of species”. *Europhysics Letters* **97** 40008 (2012) (cit. on p. 15).
- [34] A. Traulsen, J. C. Claussen, and C. Hauert. “Stochastic differential equations for evolutionary dynamics with demographic noise and mutations”. *Physical Review E* **85** 041901 (2012) (cit. on p. 15).
- [35] J. S. Weitz, H Hartman, and S. A. Levin. “Coevolutionary arms races between bacteria and bacteriophage.” *Proceedings of the National Academy of Sciences of the United States of America* **102** 9535–40 (2005) (cit. on p. 15).
- [36] U. C. Täuber, M. Howard, and B. P. Vollmayr-Lee. “Applications of field-theoretic renormalization group methods to reaction-diffusion problems”. *Journal of Physics A: Mathematical and General* **38** R79–R131 (2005) (cit. on p. 22).
- [37] M. Parker and A. Kamenev. “Extinction in the Lotka-Volterra model”. *Physical Review E* **80** 021129 (2009) (cit. on p. 33).
- [38] D. L. Hartl and A. G. Clark. *Principles of Population Genetics*. 3rd. Sunderland, MA, Sinauer Associates (1997). Chap. 274-275 (cit. on p. 35).

Part II

Vortex Line Relaxation

Chapter 6

Introduction

The second part of this dissertation addresses relaxation and steady-state properties of a true condensed matter system, namely magnetic flux lines in type-II superconductors. This class of materials encompasses all of the ceramic, high-temperature superconductors, and many of the metallic, low-temperature superconductors. Since these are used in technological and commercial applications, as well as for research purposes, a deep understanding of their dynamic and static characteristics is crucial. In this chapter, I present a brief, non-technical introduction on magnetic flux lines and their various properties. I introduce the different types of pinning sites and how their presence influences the behavior of a system of magnetic flux lines. Additionally, I give a succinct discussion of physical aging, which is relevant to the relaxation dynamics of magnetic flux lines. These topics will be discussed in much more detail in chapter 7.

6.1 Vortex Lines in Type-II Superconductors

Type-II superconductors exhibit a unique feature that makes them a particularly interesting field of study: In an externally applied magnetic field, they form topological excitations, so-called magnetic flux or vortex lines (these two expressions will be used interchangeably in the present work). In the more commonly-known type-I superconductors, external magnetic fields below the critical field strength are screened by super-currents and, hence, completely expelled from the bulk of the superconducting material (Meissner-Ochsenfeld effect). This can be viewed as a consequence of photons becoming effectively massive due to the non-zero vacuum expectation value of the superconducting order parameter in Ginzburg-Landau theory [39] (see section 7.1).

In type-II superconductors, the phase diagram is split into two superconducting phases (see figure 6.1). Below the first critical field H_{C1} , the material is in the Meissner phase, where the magnetic field is completely expelled. For external magnetic fields that lie between the two

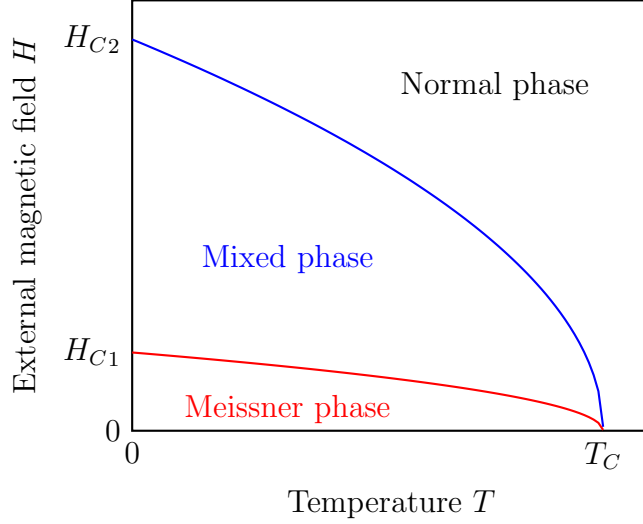


Figure 6.1: Mean-field phase diagram of a type-II superconductor. Below the first critical field strength H_{C1} the external magnetic field is expelled completely (Meissner phase). For fields between H_{C1} and H_{C2} the system is in the mixed phase, in which the magnetic field penetrates the bulk material through quantized vortex lines. Above H_{C2} the material becomes normal conducting. Thermal fluctuations and disorder strongly modify this simple mean-field phase diagram.

critical fields H_{C1} and H_{C2} , magnetic flux lines are created. Each vortex line carries one flux quantum $\Phi_0 = hc/(2e)$ of the magnetic field with the field lines existing inside the vortex core. At the upper critical field H_{C2} the material is completely covered with vortex cores and thus becomes normal-conducting. Hence, the first-order phase transition between the superconducting and normal phases in type-I superconductors is turned into two continuous, second-order transitions.

6.2 Dissipation, Pinning and Vortex Matter

An important consequence of the presence of vortex lines is that the material is not truly superconducting anymore. In the presence of an externally applied current, the vortex is subject to a Lorentz force via the magnetic field lines penetrating through the core. This leads to a finite vortex velocity, an induced electric field, and, consequently, to the dissipation of energy. Hence, vortex motion or flow yields an effective Ohmic resistance to an applied super-current. The movement of magnetic flux lines can, however, be prevented by naturally occurring or artificially introduced material defects [40, 41].

Defect sites locally suppress the superconducting order parameter and hence lead to a local reduction of the condensation energy [42]. Thus, there exists an attractive force between

defect sites and other normal-conducting regions, such as vortex cores, in order to prevent the loss of condensation energy, see section 7.1.7. Hence, material defects are pinning centers, providing potential wells in which vortex lines can get trapped, effectively stopping their motion.

In addition to Lorentz forces and disorder potential wells, vortex lines are subject to thermal fluctuations and mutual long-range repulsion. The latter stems from the interaction between the screening super-currents that surround the vortex core. Thermal fluctuations are due to thermally excited microscopic currents in the surrounding charge liquid analogous to Brownian motion. The energy scales of thermal fluctuations, pinning potential wells, vortex line tension and mutual repulsion fall in roughly the same order of magnitude, hence, magnetic flux lines in a disordered superconductor form a remarkably complex system displaying a wealth of diverse phenomena.

There are many different phases of vortex matter. A clean system, without disorder, and at low temperatures, displays a hexagonal arrangement of vortex lines, due to the long-range repulsive interaction. This so-called Abrikosov lattice was predicted theoretically by Abrikosov in 1957 [43], and experimentally first observed by Essmann and Träuble in 1967 [44]. We will discuss Abrikosov lattices in more detail in section 7.1.6. At higher temperatures a first-order melting transition into a vortex fluid phase can be observed [45, 46, 47]. In disordered materials, weak point-like pinning sites naturally occur in the form of e.g. oxygen vacancies. Their presence already destroys the low-temperature Abrikosov lattice and the first-order vortex lattice melting transition is replaced by a second-order continuous transition into a vortex glass phase [48, 49, 50, 51] without any remaining translational order. In addition, there are theoretical indications for a topologically ordered, dislocation-free Bragg glass phase [52, 53, 54, 55, 56, 57] and predictions for a multi-domain glass phase [58]. The phase diagram of a system of vortex lines in a disordered type-II superconductor with weak pinning sites is thus already very complex and rich [40, 59].

Aside from point-like pinning sites, there exist other types of correlated disorder that can affect the dynamics of magnetic flux lines. In the present work, columnar pinning sites will be discussed extensively and compared to the effects of point-like disorder. Naturally occurring line dislocations in the crystal lattice of the superconducting material can serve as columnar pinning sites. It is also possible to artificially create columnar disorder tracks by using high energy ion bombardment of material samples or nanoscale fabrication techniques. This type of pinning site yields completely different relaxational dynamics and steady-state behavior compared to point-like disorder (see chapters 8 and 9 as well as reference [60]). Civale *et al.* showed experimentally that the pinning efficiency of columnar pinning sites is considerably higher than point-like pinning sites [61]. Vortex lines in the presence of columnar disorder form a strongly pinned Bose glass phase. The vortex cores are localized at the pinning sites resulting in a diverging tilt modulus [62, 63, 64]. Analytical treatment of this system is possible via a mapping to the propagation of bosons in imaginary time [65, 66]. Other types of disorder, e.g. planar pinning sites due to grain boundaries, exist as well, but are not discussed in this work.

Our study of the steady-state behavior and the relaxation dynamics of vortex lines in disordered superconductors is based on the analysis of a coarse-grained elastic line model [64] (see section 7.2). For our computer simulations we mainly use Langevin Molecular Dynamics (LMD); see section 7.2.2. In non-equilibrium systems the validation of simulation algorithms is crucial. In particular, it is of utmost importance to clarify if an observed effect is an artifact of the specific simulation method or a true, physical feature of the system. Hence, to validate our LMD algorithm, we compare our results with data generated using a Monte Carlo (MC) algorithm [67, 68].

6.3 Physical Aging

Physical aging is an important feature of the relaxation of a multitude of complex systems. By preparing a system in an initial state away from an equilibrium or non-equilibrium steady-state, such as heating a material beyond a melting phase transition and subsequently fixing the temperature of the external heat bath to below the transition, one can observe the material's relaxation towards thermal equilibrium. Struik's ground-breaking experimental investigation of aging in various polymers showed that the response of certain materials to such a treatment is universal and not dependent on the details of the material or the system [69]. Since then, it has been shown that a multitude of glassy systems show physical aging (for an overview see [70]). In order for a system to undergo aging, the system must exhibit *slow relaxation* (in algebraic, not exponential time) and the observed quantities must not exhibit time translation invariance. For the more narrow definition of *simple aging*, two-time response and correlation functions must additionally show *dynamical scaling* [71].

Recent studies have shown that many complex systems behave glass-like and show physical aging under certain conditions [71, 72, 73]. Du *et al.* showed that disordered vortex matter exhibits physical aging. They measured the voltage response to a current pulse in a $2H - NbSe_2$ sample, and demonstrated that the response depended on the pulse duration [74]. Several research groups performed computer simulation studies of the relaxation dynamics of vortex matter. Nicodemi and Jensen investigated a restricted-occupancy model of thin-film vortex matter with MC dynamics. Using two-time correlation functions they found dynamical scaling [75, 76, 77, 78]. LMD studies of a three-dimensional elastic line model were performed by Bustingorry, Cugliandolo and Domínguez. They found evidence for physical aging in the two-time density-density autocorrelation function, the mean-square displacement and the linear susceptibility [79, 80].

6.4 Overview

In section 7.1, I first discuss the theoretical background of superconductivity on the level of Ginzburg-Landau theory. Subsequently, I introduce Abrikosov's vortex solution to the

Ginzburg-Landau equations and show how the minimum-energy configuration in a non-disordered system is a hexagonal lattice arrangement of vortices. In section 7.2 I introduce our coarse-grained elastic line model and give a brief overview of our Langevin Molecular Dynamics algorithm.

In chapter 8, I will present our results on the non-equilibrium steady-state behavior of a system of driven vortex lines. We vary an external driving force and measure the corresponding steady-state mean vortex line velocity. Since vortex line motion directly leads to an effective Ohmic resistance, this is equivalent to measuring the current-voltage (*I*-*V*) characteristics of this system. To characterize the internal fluctuations of magnetic flux lines, we additionally determine the radius of gyration, which is a measure of the roughness along the length of elastic lines. Not surprisingly, we find that there are considerable differences in the *I*-*V* characteristics and the line roughness between the point-like and columnar disorder types. By comparing results between the two simulation algorithms we find that there is a slight renormalization of the pinning energies due to the choice of algorithm.

Chapter 9 deals with the relaxation of vortex lines in the presence and absence of disorder. As stated before, the various competing energy scales render a system of interacting magnetic flux lines subject to different types of disorder very complex. The relaxation behavior is dominated by many cross-overs between distinct time regimes, thereby making a straightforward analysis impossible. By first studying free and non-interacting vortex lines we aim to disentangle the various competing effects. We will also focus on the differences between point-like and columnar pinning sites.

Chapter 7

Theoretical Background

In this chapter, I review the theoretical background on which the model our computer simulation uses is based. In section 7.1, I introduce Ginzburg-Landau theory, which is a phenomenological framework that describes superconductivity. I discuss how superconductivity arises in this framework, under which circumstances one distinguishes between type-I and type-II superconductors, and how vortices emerge as solutions of the Ginzburg-Landau equations. In section 7.2, I describe our coarse-grained elastic line model of vortex lines and our Langevin Molecular Dynamics simulation algorithm. In addition, I discuss the material parameters and simulation units we use in our investigation.

7.1 Ginzburg-Landau Theory of Superconductivity

In their seminal paper, Vitaly Ginzburg and Lev Landau proposed a phenomenological theory for superconductivity [39]. Building on Landau's original theory of second order phase transitions [81] they introduced a model free energy depending on a complex field ψ as the order parameter

$$F = F_N + \int d^2x \left[|\psi|^2 (\alpha + \frac{\beta}{2} |\psi|^2) + \frac{1}{2m} |(-i\hbar \vec{\nabla} - \frac{e}{c} \vec{A})\psi|^2 + \frac{|\vec{B}|^2}{2\mu_0} \right], \quad (7.1)$$

where F_N is the free energy of the material in its non-superconducting state, α and β are temperature-dependent phenomenological parameters, \vec{A} is the electromagnetic vector potential and $\vec{B} = \vec{\nabla} \times \vec{A}$ is the magnetic field [41].

In contrast to the BCS theory of superconductivity [82, 83, 84], this theory captures the macroscopic behavior of superconductors without assuming any microscopic effects, much like electromagnetism in media assumes some kind of effective, coarse-grained description of the materials. Ginzburg-Landau theory can, however, be rigorously derived as a limit of BCS theory close to the critical temperature [85, 86].

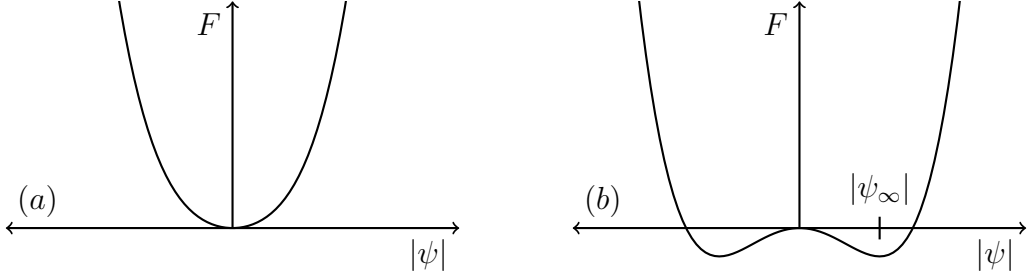


Figure 7.1: Dependence of the free energy F on the order parameter ψ for (a) $\alpha > 0$ and (b) $\alpha < 0$. F is offset by the normal state free energy F_N . Figure (b) shows that the free energy has degenerate minima at $|\psi| = |\psi_\infty|$ (Mexican hat potential) for a nonzero value of the order parameter field.

7.1.1 The Ginzburg-Landau Equations

To arrive at an equation of motion for the order parameter ψ in the Ginzburg-Landau theory, the free energy (7.1) has to be minimized with respect to the order parameter field ψ . Hence, we arrive at the collective mean-field Ginzburg-Landau equation

$$\frac{1}{2m}(-i\hbar\vec{\nabla} - \frac{e}{c}\vec{A})^2\psi + \alpha\psi + \beta|\psi|^2\psi = 0. \quad (7.2)$$

Equation (7.2) has the form of a Schrödinger equation for a particle in a magnetic field, plus a nonlinear term $\beta|\psi|^2\psi$.

In addition, we have an expression for the super-current density (via minimization of the free energy (7.1) with respect to the electromagnetic field \vec{A})

$$\vec{j} = \frac{e}{m}\Re\{\psi^*(-i\hbar\vec{\nabla} - \frac{e}{c}\vec{A})\psi\}, \quad (7.3)$$

which enables us to identify the magnitude of the order parameter field with the density of superconducting electrons and provides a connection to London's theory of superconductivity [87].

7.1.2 Superconductivity

Equation (7.3) tells us that the super-current is nonzero only if the order parameter ψ is non-zero, hence we identify a phase with non-zero ψ as superconducting. The free energy (7.1) F , with the electromagnetic field \vec{A} set to zero, is a polynomial of order 4 in ψ . Hence, the material and temperature-dependent constant β has to be positive, otherwise the free energy spectrum would be unbounded from below and the theory would be unstable with respect to finite thermal fluctuations.

Depending on the sign of the parameter α the free energy either describes a parabola with a minimum at $\psi = 0$ (for $\alpha > 0$) or a Mexican hat with degenerate minima at $|\psi|^2 = |\psi_\infty|^2 = -\frac{\alpha}{\beta}$ (for $\alpha < 0$); see figure 7.1. Hence the vacuum expectation value of ψ and thus the super-current density \vec{j} is non-zero only for negative α . Therefore we naturally expect the phenomenological parameter α to be proportional to $T - T_C$ to leading order close to the critical temperature. Hence, expanding α in a series around $T = T_C$ and dropping the terms beyond first order in $\frac{T}{T_C}$ we arrive at

$$\alpha(T) \approx \alpha_C \frac{1}{T_C} (T - T_C). \quad (7.4)$$

In addition, when expanding β in a series

$$\beta(T) \approx \beta_0 + \sum_{i=1}^{\infty} \beta_i \left(\frac{T - T_C}{T} \right)^i, \quad (7.5)$$

the zeroth order term has to be dominant $\beta_0 \gg \beta_{i>0}$ in order for the theory to be stable.

When we write the order parameter in terms of fluctuating fields in the superconducting phase $\psi = (-\frac{\alpha}{\beta} + \psi_f) e^{i\theta}$, the kinetic part of the free energy (7.1) picks up a term containing only constant pre-factors to the electromagnetic field - an effective mass term

$$-\frac{2e^2}{mc^2} \frac{\alpha}{\beta} |\vec{A}|^2.$$

Hence, the photon acquires an effective mass, in analogy to the Higgs field in the Standard Model of particle physics (which is called the Anderson-Higgs mechanism). This is the origin of the Meissner effect, the expulsion of electromagnetic fields from the superconducting material.

7.1.3 London Penetration Depth and Coherence Length

If we write the order parameter field as $\psi = |\psi| e^{i\phi}$, the kinetic energy term in (7.1) can be written as

$$\frac{1}{2m} \left(\hbar^2 (\vec{\nabla} |\psi|)^2 + \left(\hbar \vec{\nabla} \phi - \frac{e}{c} \vec{A} \right)^2 |\psi|^2 \right) \quad (7.6)$$

The gradient term is connected to changes of the magnitude of the order parameter field. This is important only for the energy contribution of domain walls, while the second term is the kinetic energy associated with ψ . If we assume negligible variations of the phase angle ϕ , this term gives $\frac{e^2 A^2 |\psi|^2}{2mc^2}$, exactly the photon mass term mentioned above. Comparing this to the kinetic energy density resulting from London's equations [41], we get the London penetration depth in Ginzburg-Landau theory

$$\lambda = \sqrt{\frac{mc^2}{4\pi e^2 |\psi|^2}} \quad (7.7)$$

The London penetration depth λ describes the characteristic length scale over which the magnetic field vanishes inside a superconductor. If we identify the order parameter with the density of superconducting electrons $|\psi|^2 = n_s$ this result is the same as one would get from London's equations [41].

In the case of vanishing external fields we can write equation (7.2) as

$$-\frac{\hbar^2}{2m\alpha(T)}\vec{\nabla}^2\psi + \psi - \frac{\beta}{\alpha}|\psi|^2\psi = 0 \quad (7.8)$$

We can then define the coherence length:

$$\xi = \sqrt{\frac{\hbar^2}{2m|\alpha(T)|}} \quad (7.9)$$

This defines the characteristic length scale over which the order parameter field varies. In BCS theory, this corresponds roughly to the size of a Cooper pair.

7.1.4 The Ginzburg-Landau Parameter

The Ginzburg-Landau parameter is defined as the ratio of the London penetration depth (7.7) over the coherence length (7.9):

$$\kappa = \frac{\lambda}{\xi} \quad (7.10)$$

In their paper Ginzburg and Landau showed that if this parameter is greater than $\frac{1}{\sqrt{2}}$, the transition from the superconducting to the normal state is smooth, over a range of external magnetic fields greater than the critical field H_{c1} [39, 43, 88]. A material exhibiting this property is called a type-II superconductor. Type-I superconductors exhibit a first order phase transition where the superconducting state breaks down immediately above the critical field.

If $\kappa > \frac{1}{\sqrt{2}}$, the surface energy of internal phase boundaries becomes negative, hence there is an energy gain associated with the creation of a region of normal-conducting material inside the superconducting phase. This mixed state persists for an external field greater than the critical field H_{c1} , but lower than $H_{c2} \equiv \sqrt{2}\kappa H_c$.

7.1.5 Vortex formation

The Ginzburg-Landau equations 7.2 and 7.3 contain non-perturbative solitonic solutions. The simplest of those are domain walls, but here we are interested in solutions containing a nonzero axially symmetric global current density, a vortex.

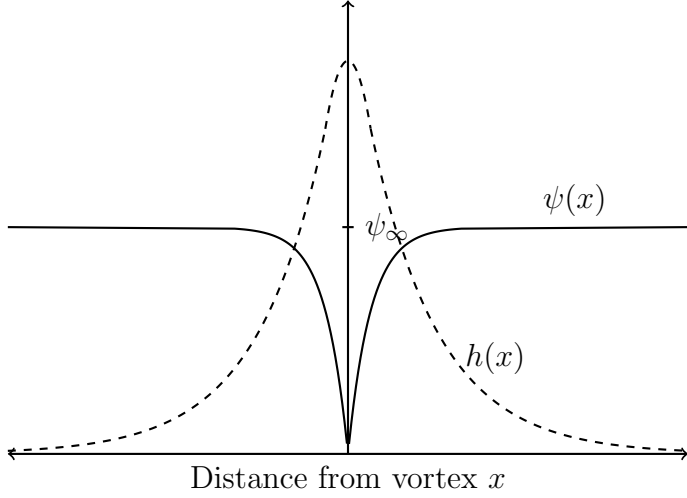


Figure 7.2: Isolated vortex. The order parameter field ψ goes to zero at the center of the vortex, indicating that superconductivity breaks down at this position. The magnetic field h is nonzero inside the vortex, its associated flux is $\frac{hc}{2e}$. See reference [41], page 151.

The part of the free energy containing the order parameter is

$$F_o = \int d^2x \left[\frac{1}{2m} \left| (-i\hbar\vec{\nabla} - \frac{e}{c}\vec{A})\psi \right|^2 + |\psi|^2 \left(\frac{\beta}{2}|\psi|^2 + \alpha \right) \right] \quad (7.11)$$

We have a condition that fixes \vec{A} at $|\vec{x}| \equiv r \rightarrow \infty$ which we will discuss later. For the second term in the energy to be finite we have to require $\psi(r \rightarrow \infty) = \sqrt{-\frac{\alpha}{\beta}} \equiv v$. The condition on ψ fixes the magnitude but not the phase of the scalar field at infinity. Thus we can use the ansatz $\psi = v \exp(i\theta)$, with $v \equiv |\psi|$, for the field solution at $r \rightarrow \infty$ [89].

Assuming that we are far enough from the vortex core and the external magnetic field is shielded by the super-currents, we can set the electromagnetic field to zero $\vec{A} = 0$. Thus, we arrive at the current density at spatial infinity

$$\vec{j} = -\frac{e}{m} \Re \{ \psi^* i\hbar \vec{\nabla} \psi \} = \frac{2e\hbar v^2}{m} \hat{e}_\theta \quad (7.12)$$

Thus the current has only an azimuthal component, so the field rotates at infinity. Figure 7.2 shows the behavior of the order parameter and the magnetic field in the vicinity of a vortex.

For $\vec{A} = 0$ in the vortex solution, the first term in (7.11) is proportional to

$$\int d^2x (\nabla_i \psi)^\dagger \nabla_i \psi \propto \int d^2x \frac{1}{r^2} = 2\pi \left(\lim_{r \rightarrow \infty} \ln r - \lim_{r \rightarrow 0} \ln r \right) \quad (7.13)$$

Thus the energy is logarithmically diverging in this case, yielding a condition on the value of the gauge field at spatial infinity. The term $\frac{e^2}{c^2} |A|^2 \psi^\dagger \psi$ has to cancel the kinetic field energy

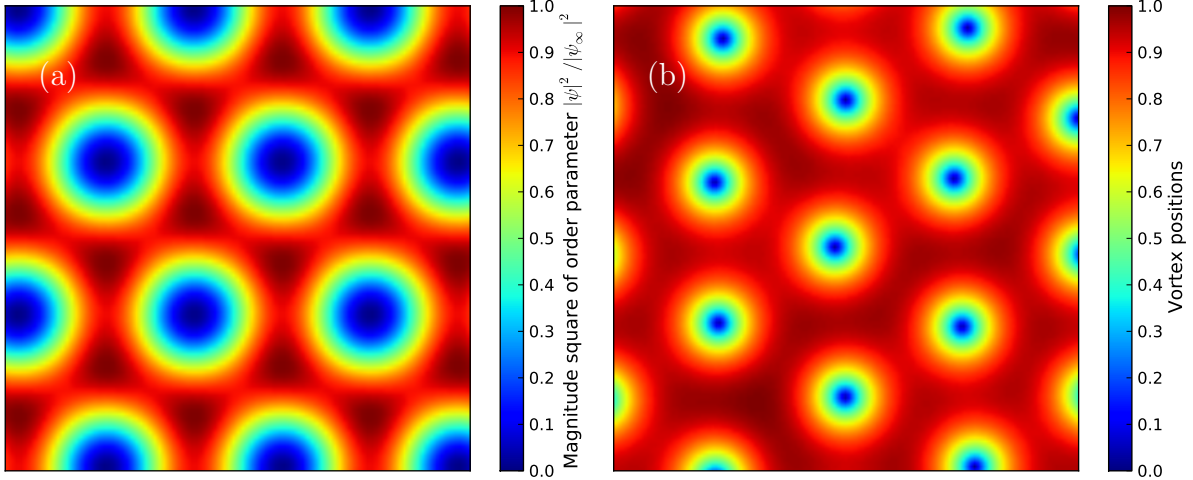


Figure 7.3: Triangular vortex lattice solutions. (a) The color plot shows the magnitude of the order parameter field $|\psi|^2$ calculated from the Abrikosov solution (7.16). The vortices are aligned in a triangular lattice with the spacing inversely proportional to the applied magnetic field. The field penetrates through the vortex cores [91]. (b) Triangular lattice from a Langevin flux line simulation. The color plot shows the approximation to the fields generated by the vortices, for illustration purposes only. Each vortex produces a contribution proportional to $1 - e^{-r/b_0}$, where b_0 describes the fundamental simulation unit of length.

so that the whole integrand vanishes faster than $\frac{1}{r^2}$, thus

$$\lim_{r \rightarrow \infty} \vec{A} = -i \frac{\hbar c}{e} \frac{\vec{\nabla} \psi}{\psi} = \frac{\hbar c}{e} \hat{e}_\theta \quad (7.14)$$

The magnetic flux through one isolated vortex is then:

$$\Phi = \int d^2x (\vec{\nabla} \times \vec{A}) \cdot \hat{e}_z = \oint \vec{A} \cdot \hat{e}_z = \frac{hc}{e} \quad (7.15)$$

This is the famous magnetic flux quantum proposed by Fritz London [90].

7.1.6 Abrikosov Lattices

In 1957, Abrikosov published a paper in which he proposed an approximate solution for the Ginzburg-Landau equations (7.2) and (7.3) [43]. His approximation is valid for the case $1 - \frac{H}{H_{c2}} \ll 1$, i.e. the external field H is very close to the upper critical field H_{c2} . In this regime the order parameter is very small $|\psi|^2 \ll 1$ and the influence of the superconducting electrons

on the magnetic field is negligible. It can then be shown, by neglecting the small, cubic nonlinear term $|\psi|^2\psi$, that solutions of the form $\psi_k \propto \exp\left[iky - \frac{(x-x_k)^2}{2\xi^2}\right]$ with $x_k = \frac{khc}{2\pi eH}$ and k a free parameter (determined by minimizing the free energy) are possible [41]. Since the theory is now linear, these solutions can be superimposed to form a crystalline lattice:

$$\begin{aligned}\psi(x, y) &= \sum_{n=-\infty}^{\infty} C_n e^{inxqy} \varphi_n(x), \\ \varphi_n(x) &= e^{-\frac{(x-x_n)^2}{2\xi^2}},\end{aligned}\tag{7.16}$$

where we restricted the possible values of k to integer multiples of the parameter q to enforce a crystalline structure. This solution shows a periodicity of $\Delta y = \frac{2\pi}{q}$ in the y direction. This automatically leads to a periodicity in the location of the vortex centers $x_n = \frac{nqhc}{2\pi eH}$ of $\Delta x = \frac{qhc}{2\pi eH}$, the period of which is controlled by q (which is again ultimately determined by minimizing the free energy). For the detailed derivation, see reference [41]. Calculating the flux through one unit cell yields

$$\phi = H\Delta x \Delta y = \frac{hc}{e}\tag{7.17}$$

Thus each unit cell of the vortex lattice carries exactly one flux quantum, as we would expect from the last section.

Which symmetry is chosen by the system is determined by minimizing the parameter $\beta = \frac{\langle\psi^4\rangle}{\langle\psi^2\rangle^2}$, i.e. the nonlinear contribution to the Ginzburg-Landau free energy. Detailed calculations show that imposing triangular symmetry by choosing the right periodicity condition $C_{n+2} = C_n$ and thus $C_1 = \pm iC_0$ yields the lowest $\beta \approx 1.16$ [91]. It should be noted here that in Abrikosov's original paper a square lattice of these vortex solutions was shown to have the lowest value of $\beta \approx 1.18$, but this mistake has since been corrected by Kleiner *et al* [91].

The hexagonal lattice solution of vortices is depicted in figure 7.3(a). Figure 7.3(b) shows that a hexagonal lattice also arises from Langevin-type vortex line simulations.

7.1.7 Pinning

A simple argument for the pinning of vortex lines at defect sites can be made via a volume effect: Defect sites locally suppress the density of superconducting charge carriers. Hence, they attract other normal-conducting regions such as vortex cores. The condensation energy density of Cooper pairs is $-\frac{\alpha^2}{2\beta}$ (from the above mean-field theory), thus the pinning energy has to be on the order of $-V\frac{\alpha^2}{2\beta}$, where V is the volume of overlap between the extent of the defect and the vortex core. However, this volume effect pinning energy is too small to account for experimental results and quasiparticle scattering effects need to be taken into account [42].

7.2 Elastic Line Model

In our investigation of the steady-state and relaxational dynamics of vortex lines, we assume that our system is in the extreme London limit, where the penetration depth λ is much larger than the coherence length ξ , and thus the Ginzburg-Landau parameter $\kappa \gg \frac{1}{\sqrt{2}}$. The size of the vortex cores, which is of the order of ξ , is then negligible, and vortex lines behave analogous to elastic lines with infinitesimal thickness.

This section was adapted with only minor changes, with kind permission of The European Physical Journal (EPJ), from our publication:

U. Dobramysl, H. Assi, M. Pleimling and U. C. Täuber, “Relaxation dynamics in type-II superconductors with point-like and correlated disorder”, Eur. Phys. J. B (2013) 86:228. “Copyright EDP Sciences, Società Italiana di Fisica and Springer-Verlag, 2013.”

7.2.1 Effective Model Hamiltonian

We consider in the following a system of N vortex lines in the London limit. In order to model the dynamics of the system we employ a fully three-dimensional elastic line description [64, 92]. Vortex lines are described by their trajectories $\vec{r}_i(z)$, where z denotes the direction of the applied external magnetic field and the crystallographic c -direction, and \vec{r}_i is the $x - y$ position of line i at z . As an immediate consequence of this description, vortex lines in this model cannot form loops or overhangs, since $\vec{r}_i(z)$ has to be unique. This is a reasonable assumption, as long as the vortex energy per length (i.e. the elastic line tension) is large compared to the energy scale of thermal fluctuations.

High- T_C superconducting materials are highly anisotropic: the crystallographic c -direction is much larger than the a and b -directions; the effective charge carrier masses M_{ab} and M_c are different for the different directions. Hence, we always assume that the magnetic field is aligned with the material’s crystallographic c direction, and the material properties discussed below are given for this configuration and assigned the in-plane index ab .

The Hamiltonian of this system is written as a functional of the vortex line trajectories with an extent of L in the z -direction and consists of three competing terms: the elastic line energy, the attractive external potential due to disordered pinning sites, and the repulsive vortex-vortex interactions:

$$\begin{aligned} H[\vec{r}_i(z)] = & \sum_{i=1}^N \int_0^L dz \left[\frac{\tilde{\epsilon}_1}{2} \left| \frac{d\vec{r}_i(z)}{dz} \right|^2 + U_D(\vec{r}_i(z), z) \right. \\ & \left. + \frac{1}{2} \sum_{j \neq i}^N V(|\vec{r}_i(z) - \vec{r}_j(z)|) \right]. \end{aligned} \quad (7.18)$$

The elastic line stiffness or local tilt modulus is given by $\tilde{\epsilon}_1 \approx \Gamma^{-2} \epsilon_0 \ln(\lambda_{ab}/\xi_{ab})$, where $\Gamma^{-1} = M_{ab}/M_c$ represents the effective mass ratio or anisotropy parameter, whereas λ_{ab} and ξ_{ab} respectively denote the London penetration depth and coherence length in the ab crystallographic plane. The in-plane vortex-vortex interaction is given by $V(r) = 2\epsilon_0 K_0(r/\lambda_{ab})$, with the zeroth-order modified Bessel function K_0 (essentially a logarithmic repulsion that is exponentially screened at the scale λ). In our investigation, the N_D pinning sites are modeled by randomly distributed smooth potential wells of the form

$$U_D(\vec{r}, z) = -\sum_{\alpha=1}^{N_D} \frac{b_0}{2} p \delta(z - z_\alpha) \left[1 - \tanh \left(5 \frac{|\vec{r} - \vec{r}_\alpha| - b_0}{b_0} \right) \right],$$

where $p \geq 0$ is the pinning potential strength, and \vec{r}_α and z_α indicate the in-plane and z position of pinning site α . Lengths are measured in units of the pinning potential width b_0 . Energies are measured in units of $\epsilon_0 b_0$ with $\epsilon_0 = (\phi_0/4\pi\lambda_{ab})^2$, and the magnetic flux quantum $\phi_0 = hc/2e$.

7.2.2 Langevin Molecular Dynamics

We employ a LMD algorithm to simulate the vortex line dynamics. To this end, we discretize the system into layers along the z axis. The layer spacing corresponds to the crystal unit cell size c_0 along the crystallographic c-direction [92, 93]. Forces acting on the vortex line vertices can then be derived from the properly discretized version of the Hamiltonian (7.18). We proceed to numerically solve the (overdamped) Langevin equation

$$\eta \frac{\partial \vec{r}_i(t, z)}{\partial t} = -\frac{\delta H[\vec{r}_i(t, z)]}{\delta \vec{r}_i(t, z)} + \vec{F}_D + \vec{f}_i(t, z). \quad (7.19)$$

with the Bardeen-Stephen viscous drag parameter $\eta = \phi_0^2/2\pi\rho_n c^2 \xi_{ab}^2$ [40, 94]. The fast, microscopic degrees of freedom of the surrounding medium are captured by thermal stochastic forcing, modeled as uncorrelated Gaussian white noise fulfilling $\langle \vec{f}_i(t, z) \rangle = 0$ and the Einstein relation $\langle \vec{f}_i(t, z) \vec{f}_j(s, z') \rangle = 4\eta k_B T \delta_{ij} \delta(t-s) \delta(z-z')$, which guarantees that the system relaxes to thermal equilibrium with a canonical probability distribution $\propto e^{-H/k_B T}$ in the absence of an external drive term. In addition, in order to simulate out-of-equilibrium settings, an external driving force \vec{F}_D (stemming from a supercurrent via the Lorentz force) can be specified. The time integration is performed via simple discretization of Eq. (7.19); see section B and reference [95].

7.3 Comparison of Microscopic Algorithms

A considerable amount of work has been done using Metropolis MC implementations of the model described above and variations thereof [68, 92, 93]. This is usually based on

performing a random but spatially truncated step and evaluating the ensuing change in the system's energy ΔE . The Metropolis rule then accepts the step with a probability $P(\Delta E) = \min\{1, \exp(-\Delta E/k_B T)\}$. A step size cut-off is necessary in order not to skip over pinning potential wells, see references [68, 93] for more information. Gotcheva *et al.* investigated the differences between a Metropolis and a continuous-time MC algorithm for a system of flux lines on a discrete lattice and subject to varying temperature and driving force [96, 97]. The continuous-time update rule preserved positional order, while the Metropolis rule led to a disordered moving state, questioning the validity of the Metropolis algorithm for studies of driven vortex matter in lattice simulations. More recent studies demonstrated that positional order was preserved in off-lattice Metropolis MC of driven vortex matter [93].

It is crucial to investigate and compare different microscopic implementations of algorithms such as Metropolis MC and LMD simulations in a non-equilibrium setting (e.g. a system of vortex lines subject to an external driving force). The choice of algorithm might introduce spurious effects that cannot be predicted *a priori*. In order to separate actual physical effects of the studied elastic line model from these artifacts, we performed a careful numerical comparison of LMD with earlier MC studies. Fast microscopic degrees of freedom are modeled by the thermal force term in LMD, see Eq. (7.19). In equilibrium the noise strength is set by the Einstein relation (fluctuation-dissipation theorem, FDT). In out-of-equilibrium situations, there exists in general no FDT-equivalent that would uniquely determine the form and strength of the noise correlations. Since the large-scale and long-time characteristics of Langevin stochastic differential equations can be drastically influenced by the noise correlator properties, it is necessary to validate results by comparing to other numerical methods [93]. In chapter 8, we therefore compare results from MC for steady-state properties of the vortex line model to data generated by the LMD algorithm. It should be noted that a direct comparison of time scales is difficult since the length of a MC time step is a dynamically generated quantity, whereas in LMD the time step duration is a function of the material parameters.

7.3.1 Material Parameters

We chose our simulation parameters to closely match the material parameters of the ceramic high- T_C type-II superconducting compound $\text{YBa}_2\text{Cu}_3\text{O}_7$ (YBCO). The material is highly anisotropic with an effective mass anisotropy ratio of $\Gamma^{-1} = 1/5$. We set the pinning center radius to $b_0 = 35\text{\AA}$ and measure simulation distances in terms of this length. The in-plane London penetration depth and coherence length are $\lambda_{ab} = 34b_0 \approx 1200\text{\AA}$ and $\xi_{ab} = 0.3b_0 \approx 10.5\text{\AA}$ respectively. The vortex line energy per unit length is $\epsilon_0 \approx 1.92 \cdot 10^{-6} \text{ erg/cm}$, hence the line tension energy scale becomes $\tilde{\epsilon}_1 \approx 0.189\epsilon_0$. The depth of the pinning center potential is set to $p = 0.05\epsilon_0$, except when noted differently. The intrinsic simulation time scale is determined by the Bardeen-Stephen viscous drag coefficient $\eta \approx 10^{-10} \text{ erg}\cdot\text{s}/\text{cm}^2$ (for the normal-state resistivity of YBCO near T_C , $\rho_n \approx 500\mu\Omega\text{cm}$, see table 1 in reference [98]), resulting in a basic time unit of $t_0 = \eta b_0/\epsilon_0 \approx 18\text{ps}$.

Chapter 8

Steady State Properties of Driven Systems

This chapter was adapted with only minor changes in the section structure and figure captions, with kind permission of The European Physical Journal (EPJ), from our publication:

U. Dobramysl, H. Assi, M. Pleimling and U. C. Täuber, “Relaxation dynamics in type-II superconductors with point-like and correlated disorder”, Eur. Phys. J. B (2013) 86:228. “Copyright EDP Sciences, Società Italiana di Fisica and Springer-Verlag, 2013.”

In the steady state of our driven flux line system, we measure the mean vortex velocity v by extracting the velocities of each line element in the direction of the driving force F_d from the time stepping algorithm in the Langevin Molecular Dynamics (LMD) method and average over all line elements in the system. In the case of the Monte Carlo (MC) method, we take the average displacement in the direction of the driving force F_d over 30 MC steps and calculate the mean velocity. Using Faraday’s law, we can relate the vortex line mean velocity to an induced electric field $\vec{E} = \vec{B} \times \vec{v}/c$, which translates to a voltage drop across the sample. Similarly, the driving force is related to an applied external current via the Lorentz force $F_d = |\vec{j} \times \phi_0 \vec{B}/B|$. Hence, a driving force vs. mean vortex velocity graph is equivalent to experimentally determined current-voltage (I-V) characteristics.

To quantify thermal spatial fluctuations along the vortex lines, we compute the vortex line radius of gyration $r_g = \sqrt{\langle (\vec{r}_{i,z} - \bar{\vec{r}}_i)^2 \rangle}$, i.e. the root mean-square displacement from the lines’ mean lateral positions. The angular brackets again indicate an average over line elements as well as noise and disorder realizations. This quantity is expected to show a maximum at driving forces just below the depinning transition, due to the zero-temperature depinning transition [99].

8.1 Point-Like Pinning Sites

We first employ LMD simulations for interacting flux lines in the presence of point-like disorder with disorder potential strength p , subject to a driving force F_d stemming, via the Lorentz force, from an external current. Results for the steady-state velocity and gyration radius are gathered in Fig. 8.1. The red dots in Fig. 8.1 indicate MC-generated data, while the solid lines were produced using LMD with different values of p . It is quite clear from Fig. 8.1(a) that a pinning potential strength $p = 0.05\epsilon_0$ in MC corresponds to $p \approx 0.04\epsilon_0$ in LMD. In MC, vortex line elements test a region with a radius of $0.25b_0$ around their current position for possible jump targets. It is conceivable that the pin energy barrier appears a bit smoother in MC since its width falls into the same length scale, which leads to the observed renormalization of the pinning potential strength. The slightly higher maximum of the MC gyration radius data for $p = 0.05\epsilon_0$ over the corresponding LMD curve with $p = 0.04\epsilon_0$ in Fig. 8.1(b) supports this argument, since vortex line elements are most likely trapped at a pinning site until they escape via a single jump. It is much less probable for any line element to escape the pin via multiple successive jumps. In LMD on the other hand, the thermal force is only an added component on top of the (in this case stronger) driving and elastic tension forces. Hence, LMD yields smooth escape trajectories out of a point pin's binding potential, and the vortex line is consequently less rough, resulting in a smaller radius of gyration.

Figures 8.1(c) and (d) show that the depinning force scales roughly linear with the pinning potential strength p , as expected [64]. The vortex velocity curves cross at $F_d/p \approx 0.19$, while the gyration radii have their maxima around $F_d/p \approx 0.12$, with a slight systematic shift to lower F_d/p for smaller pinning strength values p . It should be noted that a true continuous non-equilibrium depinning phase transition occurs only at $T = 0$ (and in the thermodynamic limit). The gyration radius maximum in the vicinity of the critical depinning force may consequently be understood as the thermally rounded remnant of this zero-temperature phase transition [99].

8.2 Columnar Pinning Sites

Figures 8.2(a) and (b) display the mean velocity v and the radius of gyration r_g as a function of the driving force F_d of vortices subject to randomly distributed columnar pinning sites. Correlated disorder is much more effective at pinning flux lines than point disorder [61]. This is reflected in a critical depinning force that is about an order of magnitude higher for columnar defects than for uncorrelated point pins of the same strength p (per layer; results shown in Fig. 8.1). In Figs. 8.2(c) and (d) the driving force is again scaled with the pin strength p . The vortex velocity curves cross at $F_d/p \approx 1.9$, which is indeed a factor of 10 larger compared to point pins. In the presence of columnar defects, a single flux line may be in one of the following four configurations: [64] (i) unpinned, located away from any

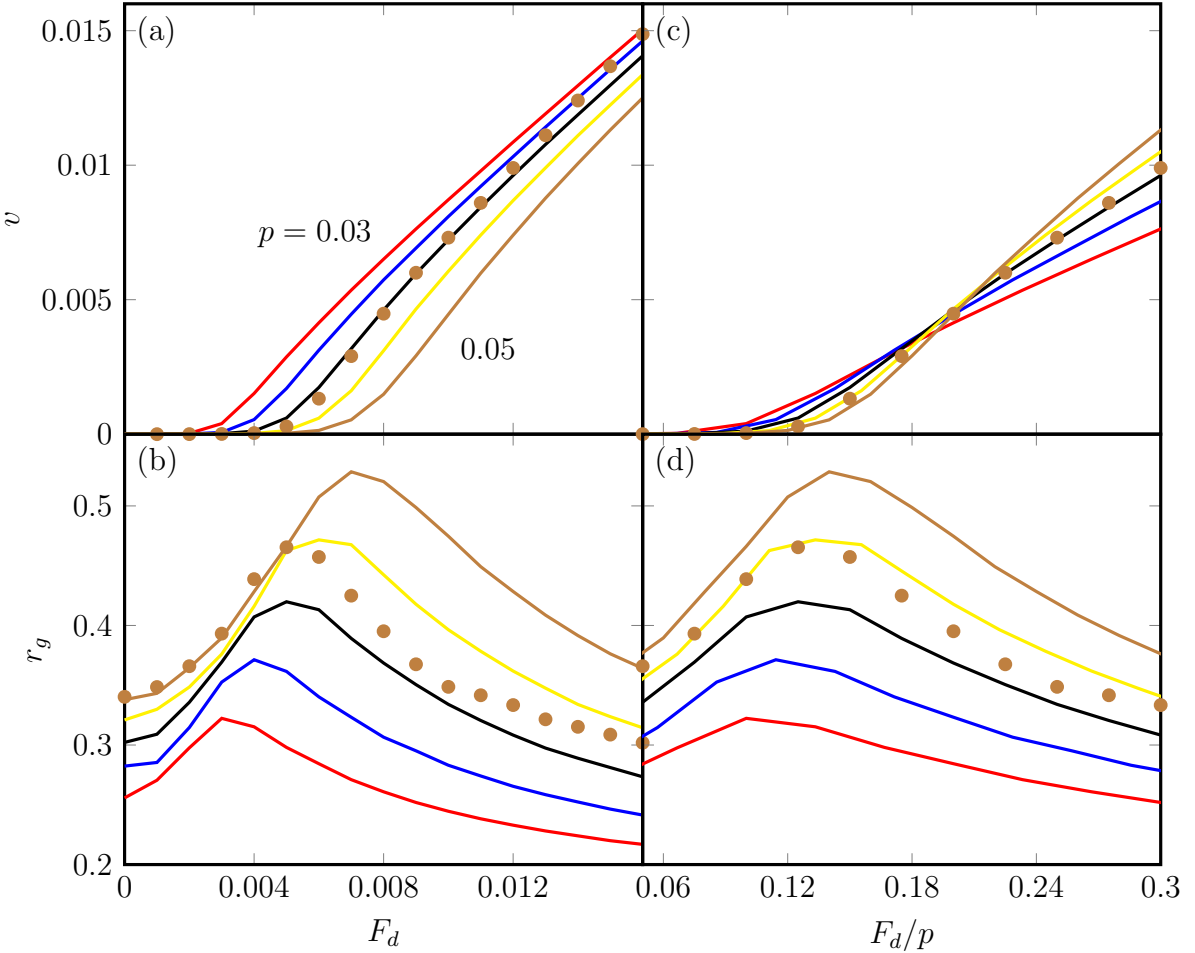


Figure 8.1: Steady-state (a) velocity and (b) gyration radius of $N = 16$ vortex lines with a length of $L = 20$ elements as a function of the driving force F_d in the presence of point pins with varying disorder potential strength p . The brown circles show data from MC simulations with $p = 0.05\epsilon_0$, while the other graphs display LMD simulation data with p ranging from $0.03\epsilon_0$ to $0.05\epsilon_0$ in steps of $0.005\epsilon_0$. In (c) and (d), the force axis is rescaled with the disorder potential strength. The velocity curves in (c) cross at $F_d/p \approx 0.19$ while the gyration radius maxima in (d) align around $F_d/p \approx 0.12$, with a slight bias towards higher F_d/p for higher values of p . (*Adapted from reference [60], figure 1.*)

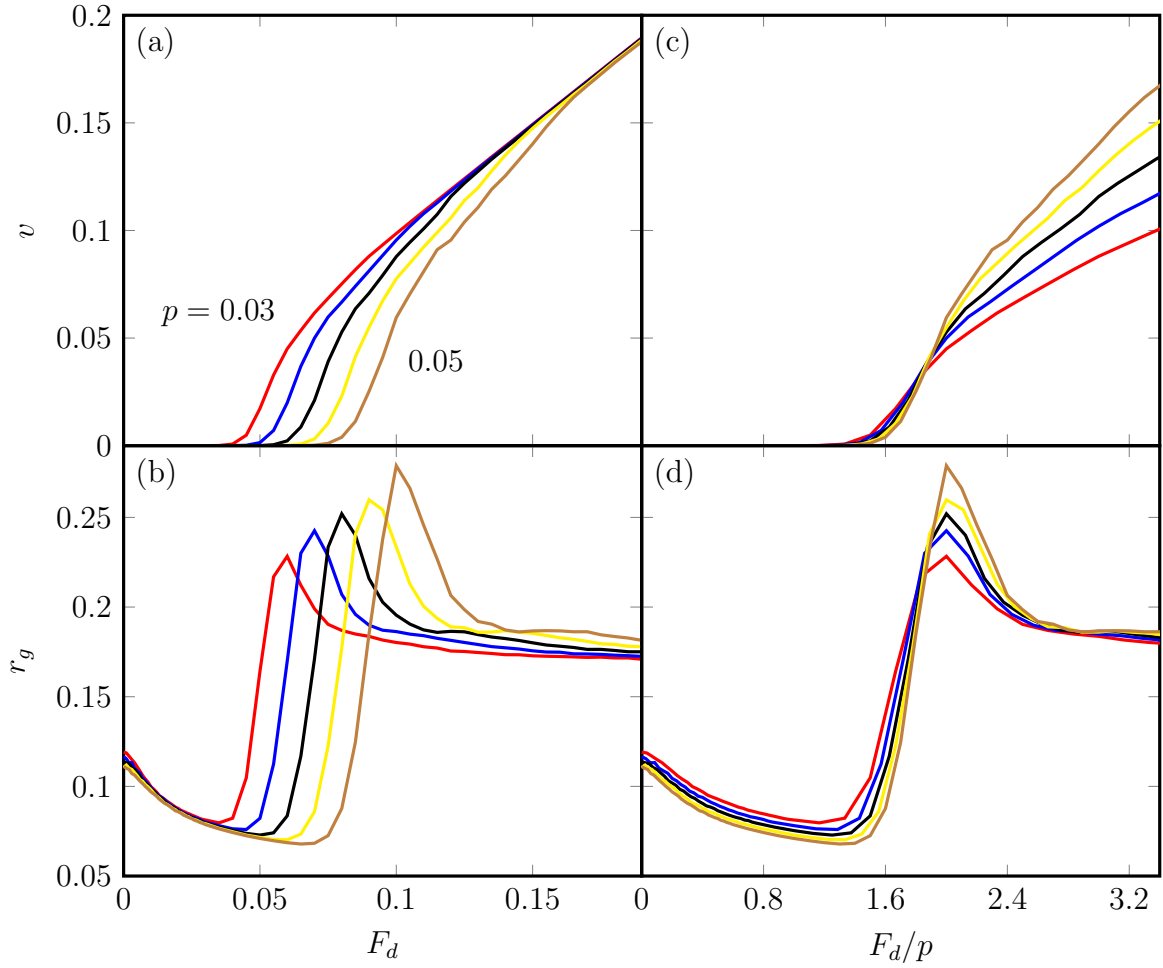


Figure 8.2: Steady-state (a) velocity and (b) gyration radius of $N = 16$ vortex lines with $L = 20$ as a function of the driving force F_d in the presence of columnar disorder. The disorder potential strength varies between $p = 0.03\epsilon_0$ and $p = 0.05\epsilon_0$ in steps of $0.005\epsilon_0$. As expected, the radius of gyration displays quite different behavior for columnar pins as compared to point pinning sites, compare Fig. 8.1(b). In (c) and (d), the force axis is rescaled with the disorder potential strength. The velocity curves in (c) cross at $F_d/p \approx 1.9$, while the gyration radius maxima in (d) align around $F_d/p \approx 2$. (*Adapted from reference [60], figure 2.*)

pinning sites; (ii) trapped at a single columnar pin for its entire length; (iii) forming a vortex half-loop where the elastic line is trapped at a single columnar defect, with the exception of an unpinned section that extends away from the defect line: Depending on the relative strengths of the driving force, thermal noise, and the pinning potential, the unpinned part may either expand or retract. This state represents a short-lived saddle-point configuration; (iv) forming single or double kinks by being simultaneously trapped at two adjacent pinning columns. This state is rather long-lived but will ultimately decay into either the unpinned or completely trapped state.

The gyration radius indicates which configurations are typically assumed by the vortex lines. For $F_d = 0$, most vortex lines are fully trapped. The radius of gyration of a trapped line is restricted by the pinning potential extension b_0 , hence we observe a marked reduction in the value of r_g with columnar pins over free, unbound lines. With increasing but below-critical F_d , r_g decreases since the mean position of trapped vortex lines shifts from the center of the pinning site, which further constrains fluctuations. In the vicinity of the critical depinning force, in the flux creep regime, r_g rises sharply due to the formation of half-loops, single-, and double-kinks. Near the transition to free-flowing flux lines, r_g develops a maximum and gradually decreases for even higher F_d . In this state, vortex motion is slightly restricted by pinning centers, but the flux lines move essentially unimpeded, and the radius of gyration approaches its unbound value.

Chapter 9

Relaxation

This chapter was adapted with only minor changes in the section structure and figure captions, with kind permission of The European Physical Journal (EPJ), from our publication:

U. Dobramysl, H. Assi, M. Pleimling and U. C. Täuber, “Relaxation dynamics in type-II superconductors with point-like and correlated disorder”, Eur. Phys. J. B (2013) 86:228. “Copyright EDP Sciences, Società Italiana di Fisica and Springer-Verlag, 2013.”

In order to study the relaxation dynamics and possible aging scaling of a system of vortex lines in various scenarios, we follow the procedures outlined in reference [67]. As a test case for our simulation code, we first investigate a system of non-interacting lines without disorder, which can be mapped to the one-dimensional Edwards-Wilkinson (EW) interface growth model. We then proceed to noninteracting lines in the presence of point-like disorder with two different pin potential strengths, where the short-time behavior is similar to the clean system while the long-time relaxation is modified by the attractive defects. To disentangle the effects of the mutual vortex repulsion from the disorder influence, we next study a system of interacting vortex lines without pinning sites. Subsequently, we present data on the full system of interacting vortex lines in the presence of point pinning centers. We then point out the differences in the relaxation kinetics in systems with point and correlated extended pins by investigating both non-interacting and interacting flux lines in the presence of columnar defects. Finally, we discuss finite-size effects due to short vortex lengths for both types of pinning sites.

In each of the scenarios presented below, we first look at the relaxation of the single-time mean-square displacement $B(t, 0)$, the time-dependent squared radius of gyration, $r_g^2(t)$, and the associated effective exponents $\beta_B(t) = d \ln B(t, 0) / d \ln t$ and $\beta_h(t) = d \ln r_g^2(t) / d \ln t$. The mean-square displacement predominantly probes changes in the average positions of single vortices. Hence we use the average of β_B over an appropriate time interval as the aging exponent that we utilize to achieve (approximate) data collapse of the two-time global mean-square displacement $B(t, s)$ and density autocorrelation function $C_v(t, s)$. The time-

dependent radius of gyration describes internal thermal vortex line fluctuations and enables us to compute an averaged scaling exponent β_h that can be used for obtaining data collapse of the two-time height autocorrelation function $C(t, s)$.

9.1 Relaxation Simulation Protocol

Throughout our study, the investigated systems contained $N = 16$ vortex lines with $L = 640$ number of layers (except where noted differently). In the scenarios that include disorder, the number of pinning sites per layer is $N_D/L = 1116$ which corresponds to a mean in-plane distance of $9b_0$ between pinning sites. In the case of randomly arranged point defects, the pinning site positions are chosen anew for each layer, whereas for columnar disorder, each layer repeats the pattern of the first layer's randomly chosen positions. The system size is set to $(16/\sqrt{3})\lambda_{ab} \times 8\lambda_{ab}$, with the aspect ratio chosen such that a clean system with interacting vortex lines reproducibly forms a hexagonal Abrikosov lattice configuration after equilibration. We employ periodic boundary conditions in the x and y directions, and free boundary conditions along the z axis.

Our initial out-of-equilibrium condition consists of a system of perfectly straight vortex lines, placed at random locations throughout the computational domain. Since the vortex line elements do not yet fluctuate (i.e. their distance from the vortex line mean in-plane position is zero), the internal vortex line configuration effectively is at zero temperature, hence, the start of the simulation at $t = 0$ is similar to an up-quench to a finite temperature $T = 10$ K. This is in contrast to their random spatial distribution, which is equivalent to an infinite temperature. We then let the system relax towards equilibrium until the waiting time $t = s$ (typically in the range of 2 to 4096) is reached, when we take a snapshot of the system. We proceed to calculate various two-time quantities (see section 9.2 below) at logarithmically-spaced time intervals with a simulation end time that is ten times larger than the waiting time.

9.2 Measured Quantities

To further accurately capture the relaxation and aging dynamics of out-of-equilibrium disordered vortex line systems, we measure two-time correlation quantities. Since we wish to compare the relaxation behavior in LMD with previously measured MC data, we utilize the same two-time observables as in reference [67]: the *height-height autocorrelation* function of the vortex lines, the two-time *mean-square displacement* and the *density-density autocorrelation* function. All these quantities depend on two times, labeled in the following as s and t , with $s < t$.

The roughness or *height-height autocorrelation* function of the vortex lines is defined by:

$$C(t, s) = \langle (\vec{r}_{i,z}(t) - \bar{\vec{r}}_i(t)) (\vec{r}_{i,z}(s) - \bar{\vec{r}}_i(s)) \rangle, \quad (9.1)$$

where $\vec{r}_{i,z}(t)$ are the in-plane coordinates of line i at layer z at time t , $\bar{\vec{r}}_i(t)$ is the mean position of line i , and the averages are taken over all line elements as well as noise and disorder realizations. This quantity contains information about *local* thermal fluctuations of vortex line elements around the flux line's mean lateral position. In the case of free, non-interacting vortices, it can be mapped to the height correlation of growing one-dimensional interfaces (see section 9.3).

The two-time *mean square displacement*, defined as

$$B(t, s) = \langle (\vec{r}_{i,z}(t) - \vec{r}_{i,z}(s))^2 \rangle, \quad (9.2)$$

measures the average square distance between a vortex line element's position at time s and a subsequent time t . This quantity provides data on the time evolution of the *global* structure of the vortex line configuration, in addition to the same local information contained in $C(t, s)$.

Finally, the two-time *density-density autocorrelation* function $C_v(t, s)$ is an observable that is measured by saving a snapshot of the positions of all vortex line elements in the system at time s , calculating the radial distance $r_i(t, s)$ each vortex line element traveled between times s and t and determining the number n_c of vortex line elements for which this distance is smaller than a prescribed cutoff distance $r_i(t, s) < r_c$. The density autocorrelation is then $C_v(t, s) = \langle n_c / NL \rangle$. Throughout our study, the cutoff distance is $r_c = 0.05b_0$. The density autocorrelation also contains information on the formation or decay of global structures; thus we expect it to generally follow the behavior of $B(t, s)$.

9.3 Free Non-interacting Vortex Lines

The thermal fluctuations of the segment locations of free (non-interacting and not subject to disorder) directed elastic lines around their mean in-plane position can be mapped to the problem of a one-dimensional interface growing via random deposition. The continuous version of this growth model is described by the stochastic Edwards-Wilkinson (EW) equation [100]. The temporal evolution of the interface height relative to its mean height is governed by a diffusive term as well as a random noise term. Hence, it may be described mesoscopically by a linear Langevin equation,

$$\frac{\partial h(z, t)}{\partial t} = \nu \frac{\partial^2 h(z, t)}{\partial z^2} + \eta(z, t), \quad (9.3)$$

where ν is the diffusive strength and $\eta(z, t)$ represents thermal white noise with zero mean and second moment $\langle \eta(z, t)\eta(z', s) \rangle = 2T\nu\delta(z - z')\delta(t - s)$ that satisfies Einstein's relation. The temperature T enters through the noise strength.

The linear nature of Eq. (9.3) makes it possible to arrive at analytical expressions for various two-time quantities [80, 101, 102]. In particular, the solution for the two-time height-height autocorrelation function in the correlated growth regime reads [101],

$$C(t, s) = C_0 s^{1/2} \left(\left[\frac{t}{s} + 1 \right]^{1/2} - \left[\frac{t}{s} - 1 \right]^{1/2} \right). \quad (9.4)$$

Comparing with the general scaling form $C(t, s) = s^{-b} f_C(t/s)$ (with scaling function f_C), this predicts the universal aging exponent $b = 1/2$ in the EW regime [67, 101]. The mean square displacement follows a similar scaling form $B(t, s) = s^{-b} f_B(t/s)$, while the density autocorrelation empirically scales as $C_v(t, s) = s^b f_{C_v}(t/s)$.

The relaxation of the observables $B(t, 0)$, $r_g^2(t)$ and the three two-time correlation functions $B(t, s)$, $C(t, s)$, and $C_v(t, s)$ in this scenario as observed in our LMD simulations is presented in Figs. 9.1 and 9.2, respectively. For a very thin system with $L = 10$, we immediately see from the time evolution of the effective exponent $\beta_B(t)$ [solid line with black circles in Fig. 9.1(b)] that the system starts to cross over into equilibrium where $B(t, 0) \sim t$, $\beta_B \rightarrow 1$ for early times $t > 2^5$, and it is truly equilibrated after $t > 2^{10}$. This is also visible in the unscaled two-time quantities $B(t, s)$ and $C_v(t, s)$ displayed in Figs. 9.2(a,c): For $s > 2^4$, the data of $B(t, s)$ for different waiting times s fall onto a single master curve, which indicates the recovery of time translation invariance. In contrast, the data for $C_v(t, s)$ collapse for all waiting times s . The difference in the onset of data collapse in these two quantities is caused by local thermal fluctuations contributing to the mean-square displacement, whereas short-scale variations are effectively averaged out due to the finite cutoff radius in the density autocorrelation; see the description of the algorithm for calculating $C_v(t, s)$ in section 9.2 and reference [67] for more information. The effective gyration radius exponent $\beta_h(t)$, displayed in Fig. 9.1(d), decreases from the start and eventually reaches zero around $t \approx 2^7$. For such a short flux line length, the crossover from the EW regime to the saturated (equilibrated) regime happens at very early times; see reference [103] for a discussion of different EW regimes and the length dependence of the crossovers. The two-time height-height autocorrelation function $C(t, s)$, plotted in Fig. 9.2(b), shows data collapse for waiting times $s > 2^7$, which reflects the time evolution of $\beta_h(t)$.

The extended, bulk-like system with $L = 2560$ exhibits much slower relaxation and hence enables us to study the dynamical aging scaling regime. The effective exponents $\beta_B(t)$ and $\beta_h(t)$ [solid lines with black triangles in Figs. 9.1(b,d)] show the remnants of a crossover for short times, while staying at a value of approximately 0.5 for $t > 2^4$. Figures 9.2(d-f) depict $B(t, s)$, $C(t, s)$ and $C_v(t, s)$ respectively as functions of t/s and scaled with appropriately chosen exponents of the waiting time. The data for all three quantities show data collapse for $s > 2^4$ with exponent $b = 0.5$, indicating dynamical scaling and hence full aging in this time regime. The aging exponent of the two-time height-height autocorrelation function coincides with the predicted EW value from Eq. (9.4).

Except for the early-time crossover between the EW and saturation regimes, which is not

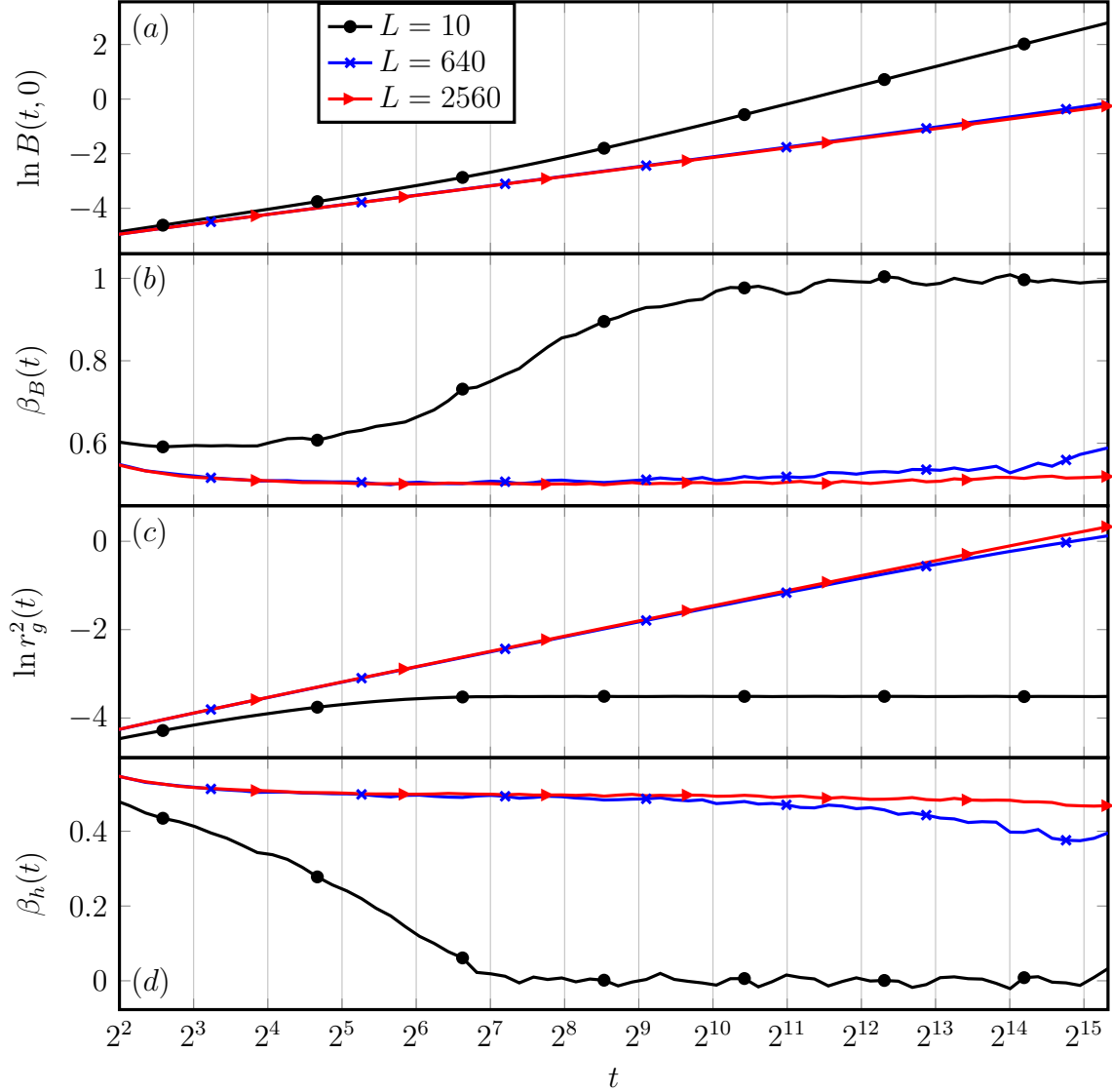


Figure 9.1: Relaxation behavior of (a) the vortex line mean-square displacement $B(t, 0)$, (c) the squared gyration radius $r_g^2(t)$, and (b,d) the associated effective exponents β_B and β_h over time for free non-interacting flux lines with length $L = 10$ (\bullet marker), $L = 640$ (\times marker) and $L = 2560$ (\blacktriangleright marker) averaged over at least 1000 realizations. (Adapted from reference [60], figure 3.)

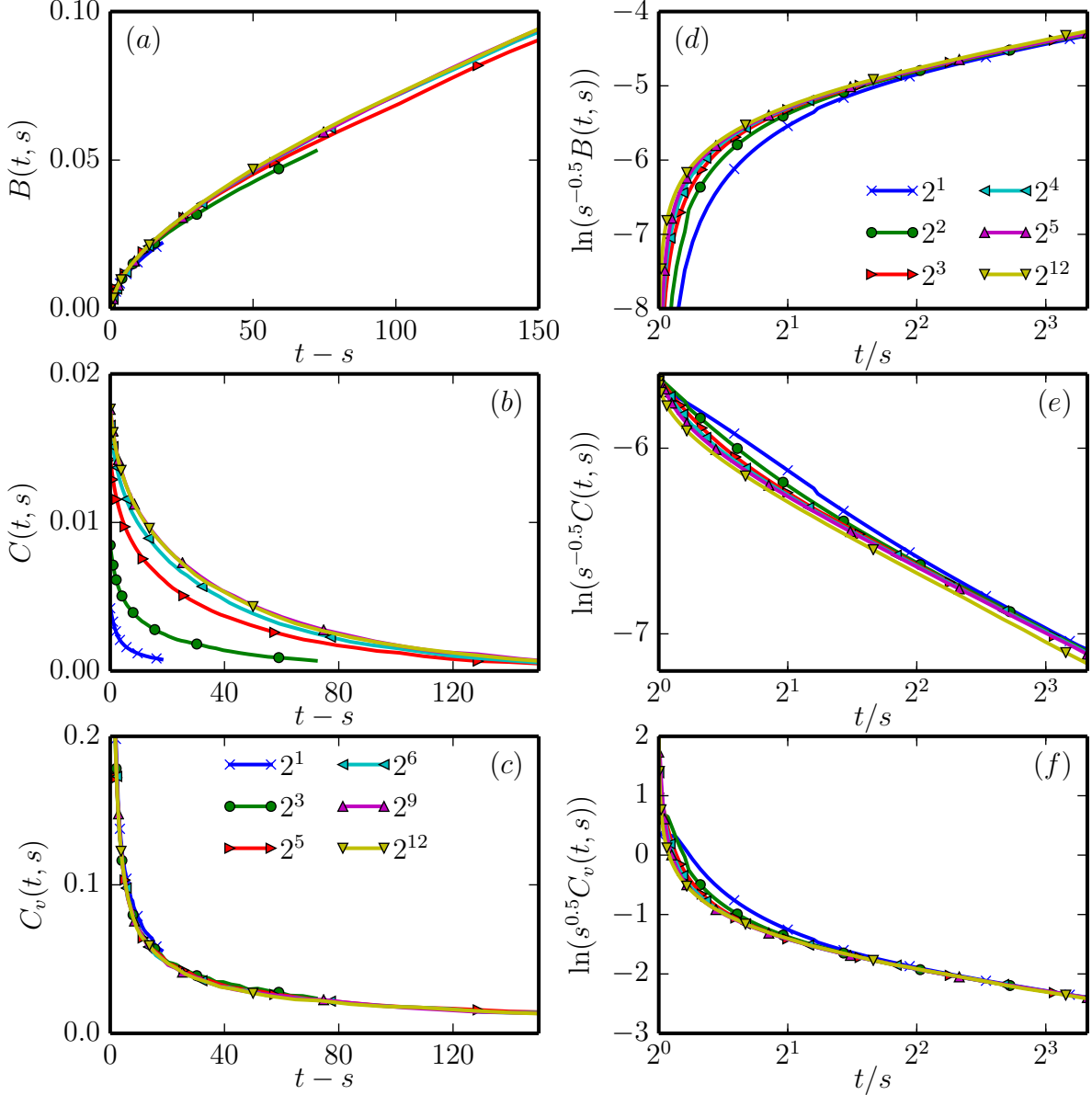


Figure 9.2: Relaxation of two-time quantities in a system of non-interacting flux lines without disorder for a line length of (a-c) $L = 10$ and (d-f) $L = 2560$, averaged over 800 different noise realizations. The sub-figures show (a,d) the mean-square displacement $B(t, s)$, (b,e) the height autocorrelation function $C(t, s)$, and (c,f) the density autocorrelation function $C_v(t, s)$ as a function of (a-c) $t - s$ and (d-f) t/s . Waiting times range from $s = 2$ to $2^{12} = 4096$. For $L = 10$, the system rapidly reaches equilibrium. The height autocorrelation function in (b) displays a short time window ($s < 64$) where it explicitly depends on s and time translation invariance is broken. For $L = 2560$ and $s > 16$, all quantities show aging and dynamical scaling with the EW exponent $b = 0.5$. (Adapted from reference [60], figure 4.)

visible in Fig. 3 in reference [67], our findings produced via LMD simulations are in complete agreement with the MC data for both thin and extended “bulk” systems.

9.4 Non-interacting Vortices with Point Disorder

We now proceed to add point-like disorder with pinning potential strengths $p = 0.01\epsilon_0$ and $p = 0.05\epsilon_0$ to a system of non-interacting vortex lines, see Fig. 9.3. The equilibrium configuration at low temperatures constitutes an extremely dilute vortex glass. For the smaller defect strength of $p = 0.01\epsilon_0$ there exists an intermediate time regime $2^3 < t < 2^7$ during which both effective exponents $\beta_B(t)$ and $\beta_h(t)$ are fairly constant before developing a maximum around $t = 2^{10}$ with a subsequent crossover into a frozen state with $\beta_B, \beta_h \rightarrow 0$ where the vortex lines are firmly bound to the point defects [solid lines with black circles in Fig. 9.3(b,c)]. The slight downward slope at early times is a remnant of the crossover from the random-noise into the EW regime of free flux lines. In fact, the exponent values at times $t < 2^7$ approximately equal those of the disorder-free system, indicating that the time evolution of the mean lateral vortex position is essentially the same as for free lines prior to the disorder effects becoming noticeable. At later times, vortex movement starts to become affected by the attractive pinning sites, which temporarily accelerates the relaxation kinetics as the vortices are drawn into potential wells, before flux line motion becomes at last frozen at the defects.

Figures 9.4(a-c) show the resulting relaxation of the two-time mean square displacement $B(t, s)$, the height-height autocorrelation function $C(t, s)$ and the density-density autocorrelation function $C_v(t, s)$ for the system with pinning strength $p = 0.01\epsilon_0$. The global quantities B and C_v are scaled using the aging exponent $b = 0.543$ taken from the average effective exponent β_B over the short- to intermediate-time region $2^3 < t < 2^7$, where β_B is roughly constant. These two-time autocorrelation functions yield approximate dynamical scaling for waiting times in this time regime, which further supports the interpretation that pinning sites are essentially irrelevant for the motion of the vortex line mean lateral positions during the early stages of the relaxation process.

In the short-time regime $t < 2^5$, the squared gyration radius $r_g^2(t)$ in Fig. 9.3(c,d) is also described by a power law with an approximate effective exponent $\overline{\beta_h} \approx 0.523$. Using this value as the aging exponent for the scaled two-time height-height autocorrelation function $C(t, s)$ in Fig. 9.4(b) reveals approximate dynamical scaling in this time window. However, stronger deviations from the free-line behavior are observed for $C(t, s)$ than for the other quantities. For larger times $t > 2^6$ correlations become increasingly longer-lived, since vortex line elements become trapped at pinning sites. Hence, the influence of weak point defects is observed mainly in the fluctuations of flux line elements, whereas the movements of their mean lateral positions are hardly modified.

For a larger pin strength $p = 0.05\epsilon_0$, the effective exponent maxima in Figs. 9.3(b,d) develop

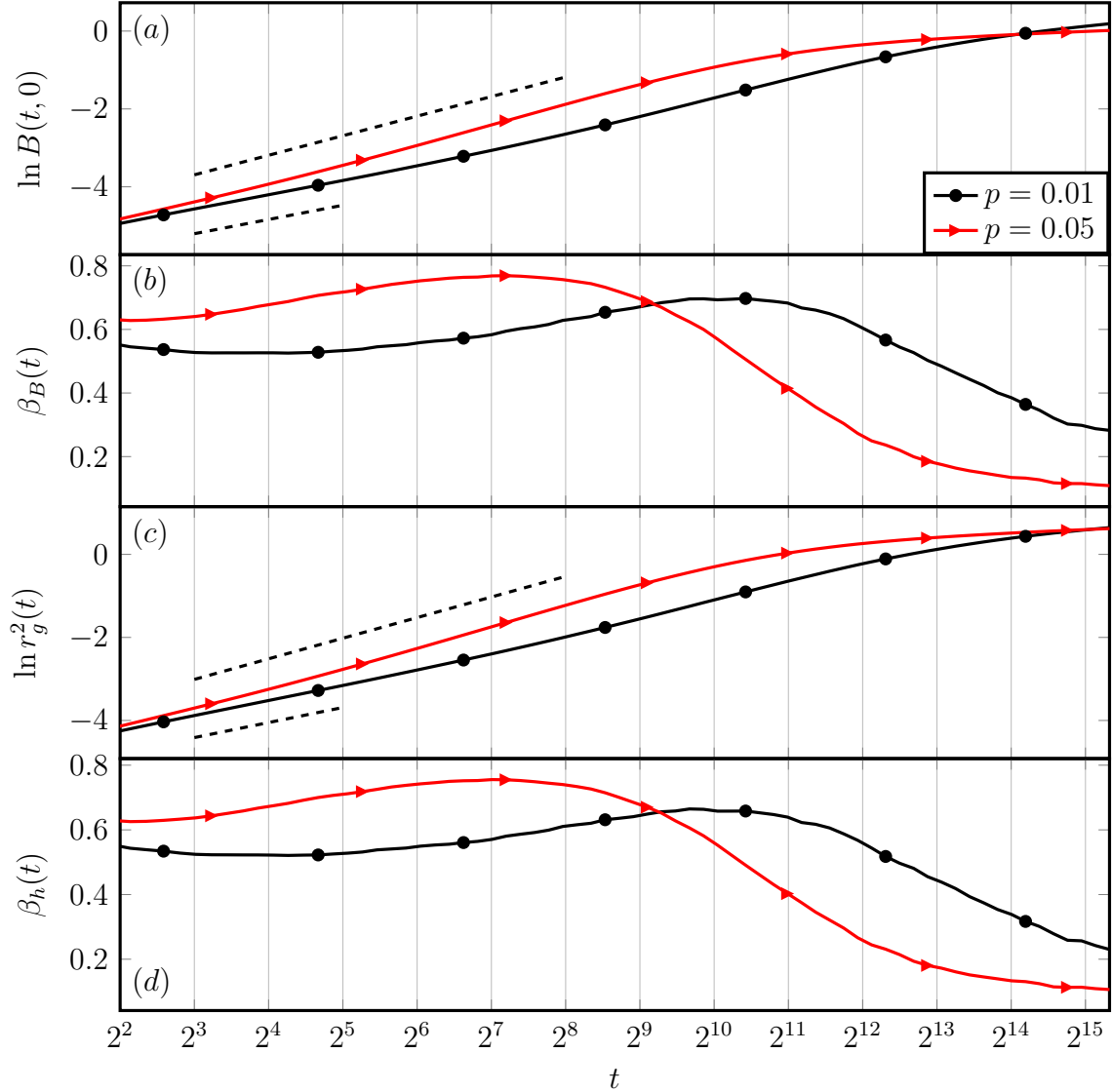


Figure 9.3: Relaxation behavior of (a) the flux line mean-square displacement $B(t, 0)$, (c) the squared gyration radius $r_g^2(t)$, and (b, d) the associated effective exponents β_B and β_h over time for non-interacting vortices subject to point pins with potential strength $p = 0.01\epsilon_0$ (● marker) and $p = 0.05\epsilon_0$ (►), averaged over 1000 realizations. For $p = 0.01\epsilon_0$, the dashed lines (below the curves) indicate the power laws with mean effective exponents $\overline{\beta}_B \approx 0.527 \pm 0.003$ in (a) and $\overline{\beta}_h \approx 0.523 \pm 0.002$ in (c) over the range $2^3 \leq t \leq 2^5$. Similarly for $p = 0.05\epsilon_0$, the dashed lines (above the curves) show the power laws with mean effective exponents $\overline{\beta}_B \approx 0.725 \pm 0.041$ and $\overline{\beta}_h \approx 0.716 \pm 0.037$ over the range $2^3 \leq t \leq 2^8$. (Adapted from reference [60], figure 5.)

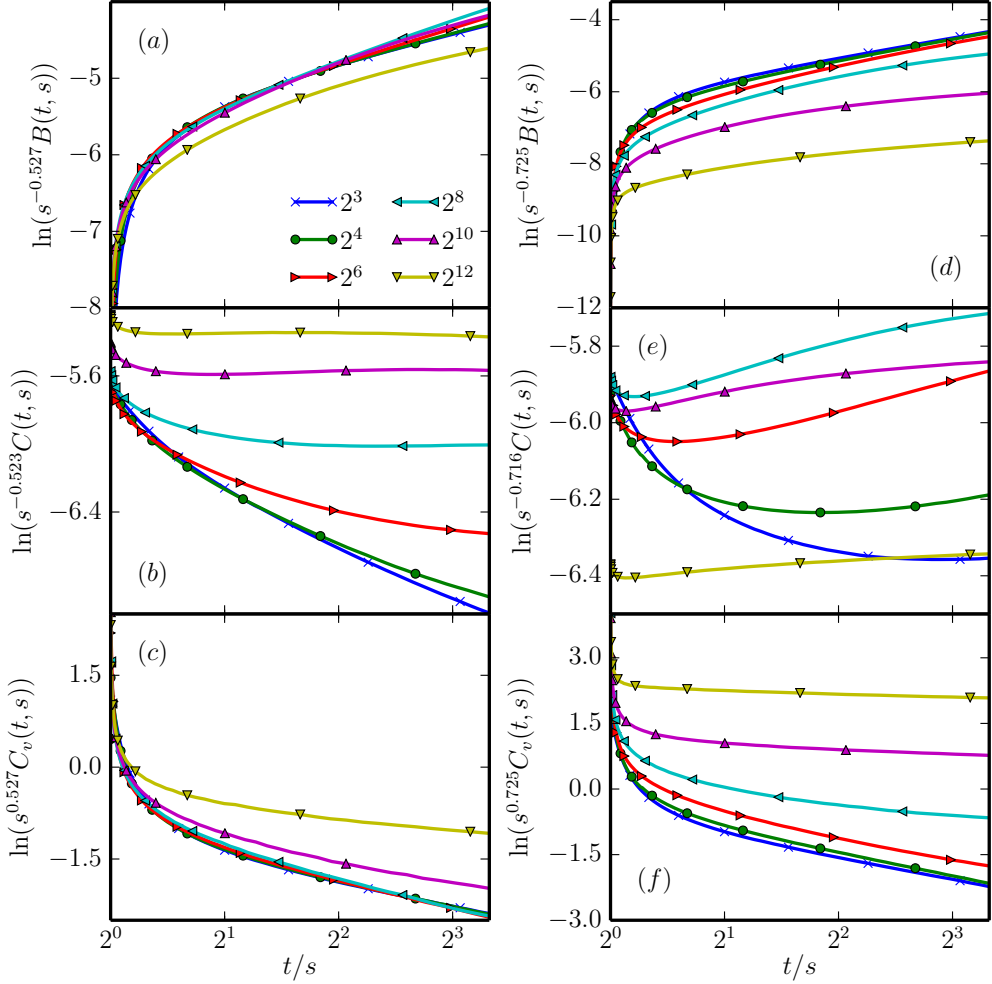


Figure 9.4: Relaxation of (a,d) the mean-square displacement, (b,e) the height autocorrelation function, and (c,f) the density autocorrelation in a system of non-interacting vortex lines of length $L = 640$, subject to randomly distributed point pins with a potential depth of (a-c) $p = 0.01\epsilon_0$ and (d-f) $p = 0.05\epsilon_0$; data averaged over 1000 realizations. Time translation invariance is broken throughout the simulation time window. For both pinning strengths, dynamical scaling for the mean-square displacement and the density autocorrelation approximately holds in an intermediate range of waiting times s , with the mean effective exponents inferred from Fig. 9.3. (Adapted from reference [60], figure 6.)

earlier, near $t = 2^7$, and there appears no region with approximately constant exponents. For $t > 2^{11}$, the system crosses over into a regime where the vortex line configuration appears to become frozen at the pins. This is reflected also in the two-time quantities, where we only see approximate data collapse for B and $C_v(t, s)$ for waiting times $s < 2^6$ [Figs. 9.4(d,f)]. The two-time height autocorrelation function $C(t, s)$ in Fig. 9.4(e) yields interesting non-monotonic behavior for $s > 2^3$, where correlations actually increase again after developing a minimum.

Elastic manifolds subject to disorder can be characterized by means of the roughness exponent χ which is defined via the height-height correlation function along the manifold dimensions [104] (here, the contour length of the directed lines)

$$C(z - z') = \langle [\vec{r}(z) - \vec{r}(z')]^2 \rangle \sim |z - z'|^{2\chi}. \quad (9.5)$$

In the case of a dilute flux line system, for which mutual interactions may be neglected, and free of disorder, thermal fluctuations lead to the EW roughness exponent $\chi = 0.5$, in agreement with our numerical observations. In the dilute vortex glass phase with point-like disorder, renormalization group analysis of manifolds subject to Gaussian disorder [104, 105] predicts a roughness exponent $\chi = 5/8$. Our LMD simulations yield a distance-dependent effective roughness exponent in the range of $0.5 < \chi_{eff} < 0.8$ for a system of non-interacting vortex lines with point-like pinning sites. It should be emphasized, though, that in our model the pinning sites are exclusively attractive. It turns out that the out-of-equilibrium relaxation behavior is considerably different for directed lines subject to a mixture of attractive and repulsive pins: One then actually observes simple aging, albeit with non-universal scaling exponents that depend on temperature as well as pinning strength [67, 106].

9.5 Interacting Vortex Lines without Disorder

To disentangle the effects of mutual flux line repulsion from the influence of disordered point pinning sites, we next study the non-equilibrium relaxation of a clean system of interacting vortex lines. Fig. 9.5 shows the relaxation of the mean-square displacement, the radius of gyration, and the associated effective exponents in this scenario, whereas Fig. 9.6 displays the behavior of the three two-time autocorrelations. One may immediately identify striking differences between non-interacting and mutually repelling vortex lines in the relaxation of $B(t, s)$ and its associated effective exponent $\beta_B(t)$; compare Figs. 9.1(a,b) and Figs. 9.5(a,b). The initially large value of β_B in Fig. 9.5(b) can be traced to the rapid formation of long-range order due to repulsive vortex interactions. After the Abrikosov lattice has fully formed, flux lines perform confined random walks due to the efficient caging from neighboring vortices, which eventually leads to a low effective exponent $\beta_B \approx 0.2$ for $t > 2^{12}$. The data collapse in Fig. 9.6(b) shows that an averaged $\overline{\beta_B} \approx 1.6$ may serve as the effective aging exponent for the two-time mean square displacement $B(t, s)$ for short waiting times $s < 2^6$.

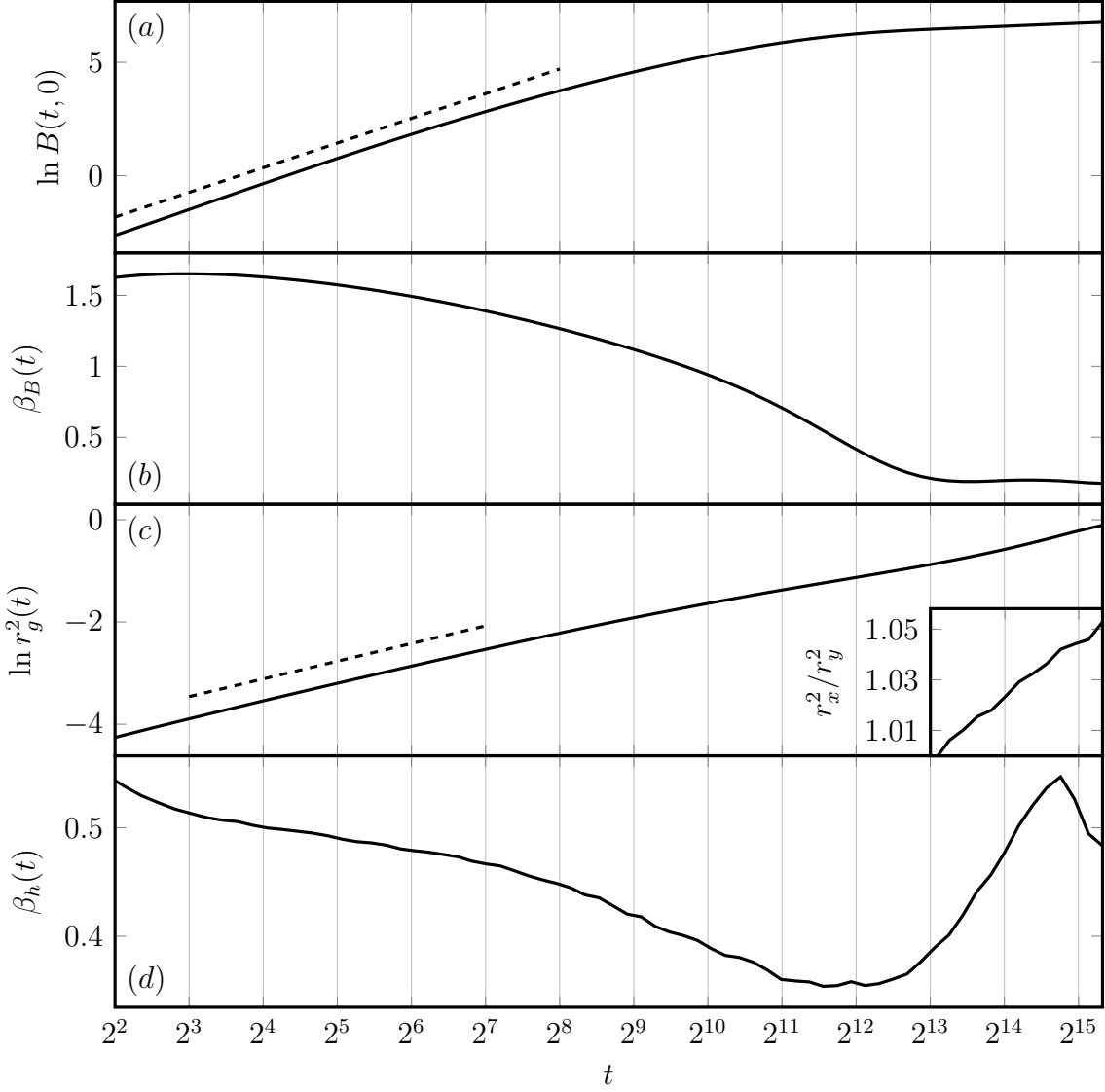


Figure 9.5: Relaxation behavior of (a) the flux line mean-square displacement $B(t, 0)$, (c) the squared gyration radius $r_g^2(t)$, and (b, d) the associated effective exponents β_B and β_h over time for interacting vortices in a system without pinning centers, averaged over 5000 realizations. The dashed lines indicate power laws with the mean effective exponents (b) $\overline{\beta_B} \approx 1.57 \pm 0.08$ (averaged over the time range $2^2 \leq t \leq 2^6$) and (d) $\overline{\beta_h} \approx 0.50 \pm 0.02$ (averaged over $2^3 \leq t \leq 2^7$). The inset in (c) shows the ratio of the x and y components of the radius of gyration for $t > 2^{12}$. (*Adapted from reference [60], figure 7.*)

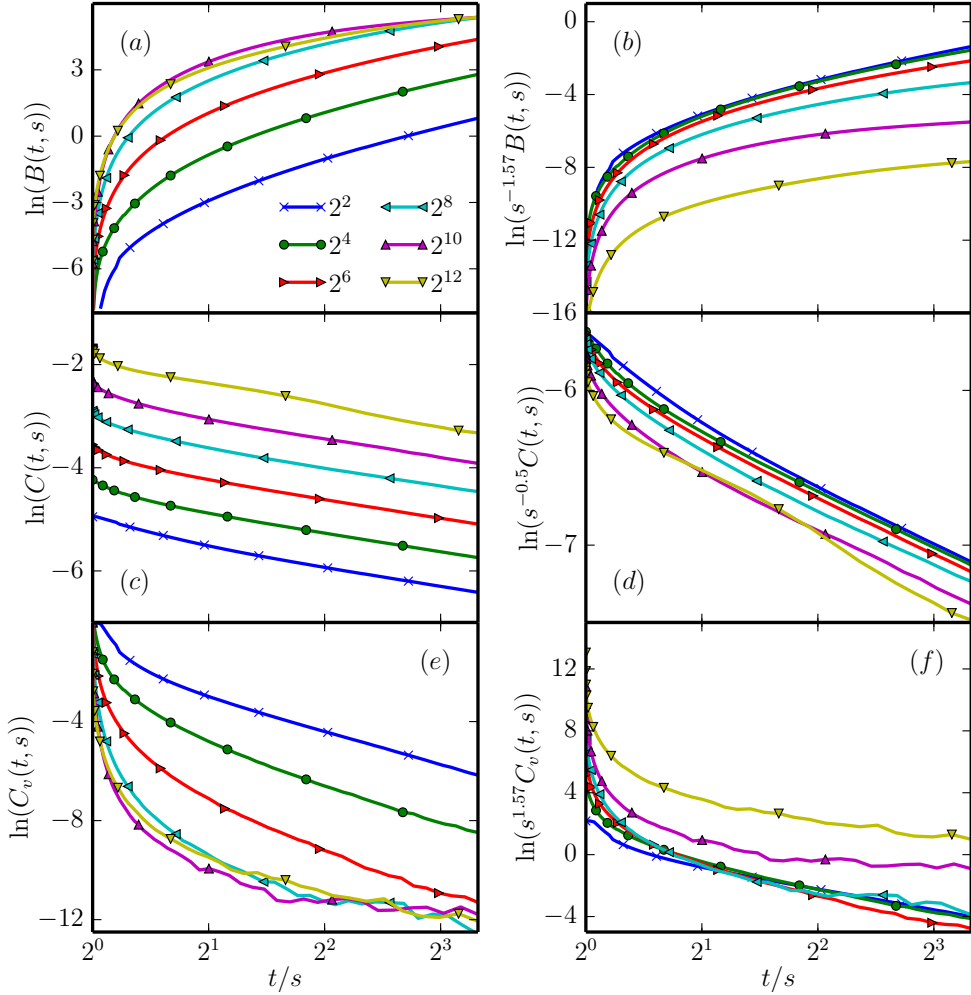


Figure 9.6: Relaxation of (a,d) the mean-square displacement, (b,e) the height autocorrelation function, and (c,f) the density autocorrelation in a system of interacting flux lines without disorder and $L = 640$; data averaged over 800 realizations. The left-hand panels show the unscaled log-log data, whereas data on the right-hand side are scaled by the waiting time s using the mean exponents from Fig. 9.5. (Adapted from reference [60], figure 8.)

The difference between interacting and non-interacting systems does not appear as drastic for the squared radius of gyration $r_g^2(t)$ as for $B(t, 0)$, compare Figs. 9.1(c,d) and Figs. 9.5(c,d). After $t > 2^{10}$, the Abrikosov lattice starts to form, and the repulsive forces due to neighboring vortex lines increasingly suppress transverse flux line wandering. For $t > 2^{12}$, the gyration radius components along the x and y directions assume slightly different values owing to the anisotropic hexagonal vortex line arrangement, which in our rectangular system is always oriented along the x direction; see the inset in Fig. 9.5(c). For small waiting times $s < 2^6$, the height autocorrelation data can be collapsed with the EW aging scaling exponent $b = 0.5$.

9.6 Interacting Vortex Lines with Point Disorder

We are now in a position to investigate the system of interacting vortex lines subject to attractive point-like disorder. As expected, the global time evolution, see Fig. 9.7(a,b), which is dictated by the mutual vortex repulsion, is hardly modified by the defects. The effective exponent $\beta_B(t)$ displays essentially the same behavior as in the absence of pinning centers; compare Figs. 9.7(b) and 9.5(b). Similarly, the aging exponents and the overall shapes of the mean-square displacement and the density-density autocorrelation in Fig. 9.8(a,c) almost match the simulation results without disorder. For short times $t < 2^6$, the effective gyration radius exponent $\beta_h(t)$ in Fig. 9.7(d) is quite similar to $\beta_h(t)$ in the non-interacting case with point pins, see Fig. 9.3(d). For longer times, repulsive forces alter the relaxation of $r_g^2(t)$, which tends towards higher values, Fig. 9.7(c). Hence, the global observables $B(t, s)$ and $C_v(t, s)$ are influenced mainly through the presence or absence of vortex-vortex repulsion through the ensuing mutual caging. The local quantity $C(t, s)$, on the other hand, better probes information on the disorder present in the sample.

In MC simulations [67], an interesting, non-monotonic behavior was revealed in the height-height autocorrelation function for a system of interacting vortex lines subject to point-like disorder: The height autocorrelations displayed a pronounced maximum for small waiting times s and $\ln(t - s) \approx 5$. Yet this feature is absent when the corresponding system is investigated with our LMD algorithm; see Fig. 9.8(b). In the present study, we have taken the vortex mass per unit length to be small and neglected the inertial term in the Langevin equation; see section 7.2.2. The algorithm used in reference [67] assumes a finite displacement per MC step which generates an effective mass. This in turn gives rise to oscillatory behavior at short times. This interpretation is indeed confirmed by LMD simulations that allow for a mass term in the Langevin equation, as depicted in Fig. 9.9. With increasing vortex mass, $C(t, s)$ shows damped oscillations on top of the monotonic time dependence of the overdamped, zero-mass case.

We observe two-step relaxation behavior, typical e.g. for structural glasses, in the normalized two-time height-height autocorrelation $C(t, s)$ when plotted as a function of the time difference $t - s$, shown in Fig. 9.8(b). This behavior was also reported in the previous MC study [67]: A β -relaxation regime where $C(t, s)$ is hardly changing and displays time trans-

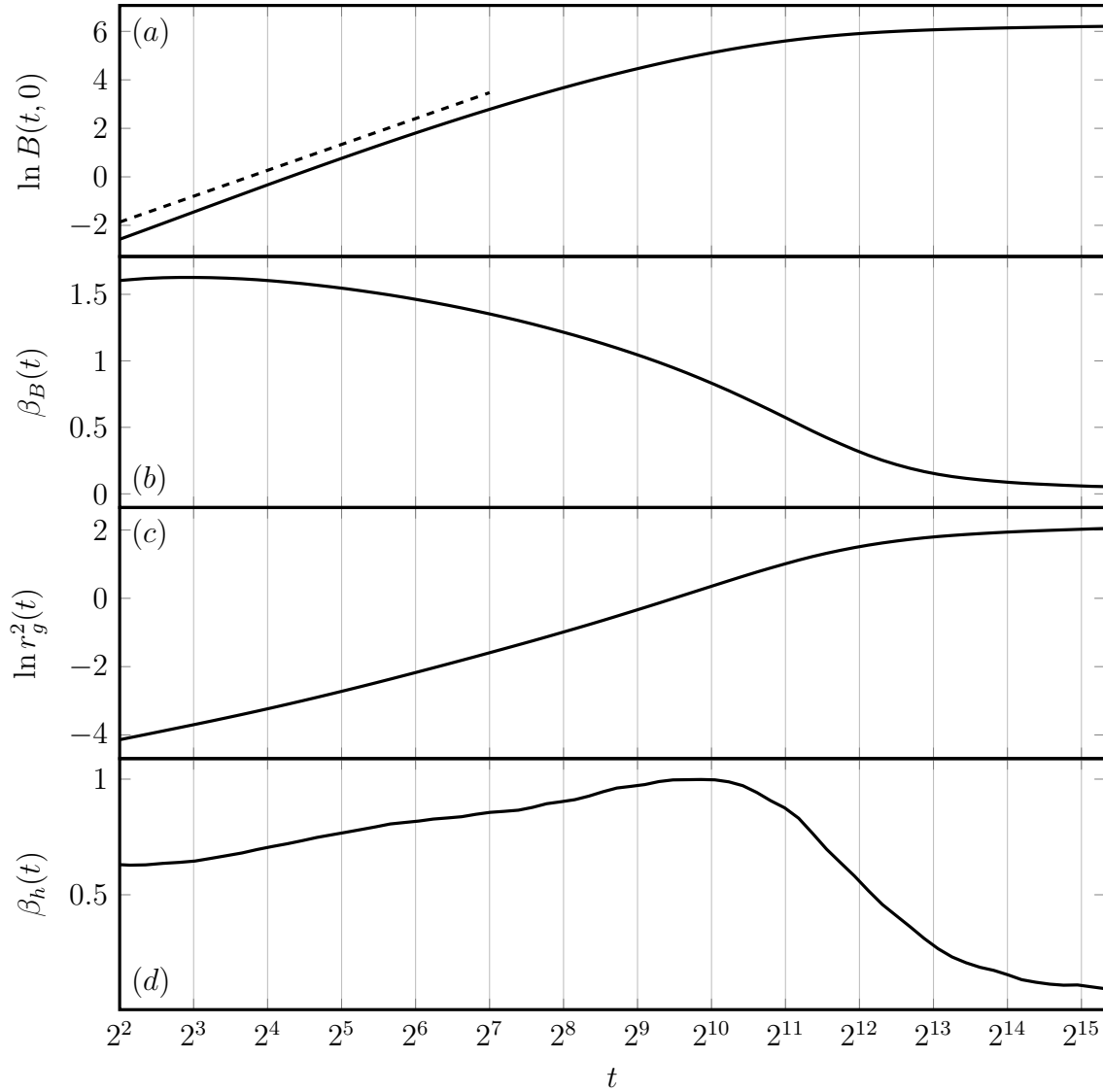


Figure 9.7: Relaxation behavior of (a) the flux line mean-square displacement $B(t, 0)$, (c) the squared gyration radius $r_g^2(t)$, and (b, d) the associated effective exponents β_B and β_h over time for interacting vortices in a system with point-like disorder of strength $p = 0.05\epsilon_0$, averaged over 1000 realizations. The dashed line in (a) indicates a power law with the mean effective exponent $\overline{\beta_B} \approx 1.54 \pm 0.08$ (averaged over the time interval $2^2 \leq t \leq 2^7$). (Adapted from reference [60], figure 9.)

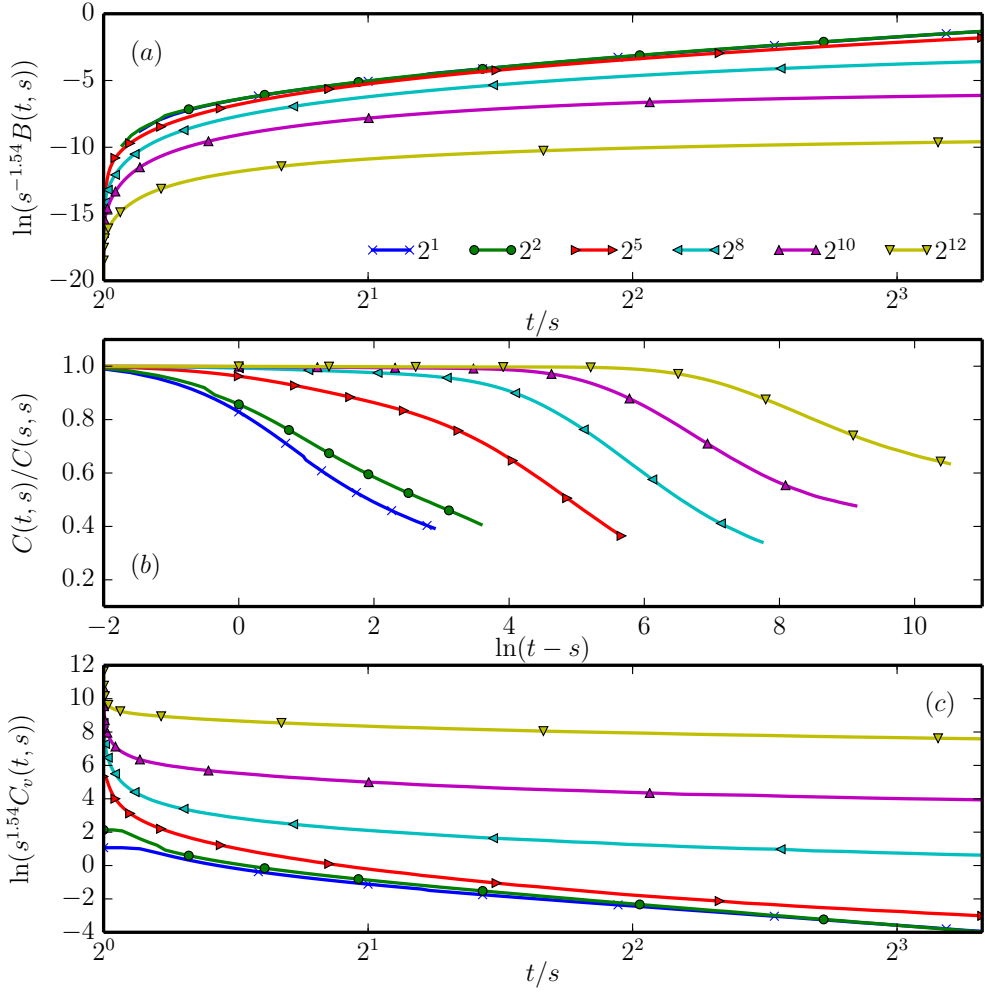


Figure 9.8: Relaxation of (a) the mean-square displacement, (b) the normalized height autocorrelation function, and (c) the density autocorrelation in a system of interacting vortex lines with point pinning centers of strength $p = 0.05\epsilon_0$ and $L = 640$; data averaged over 800 realizations. (*Adapted from reference [60], figure 10.*)

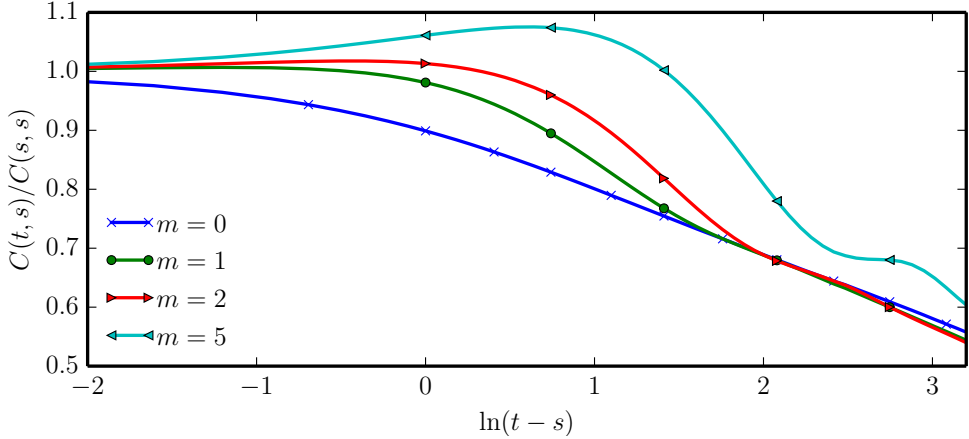


Figure 9.9: The normalized two-time height autocorrelation function $C(t, s)$ for different values of the vortex mass m in a system of interacting flux lines subject to randomly distributed point pins of strength $p = 0.05\epsilon_0$, at waiting time $s = 8$, and averaged over 1000 simulation runs. The data for $m > 0$, for which $C(t, s)$ displays non-monotonic and even oscillatory behavior, was generated using the Brünger-Brooks-Karplus integrator [107, 108]. (Adapted from reference [60], figure 11.)

lation invariance precedes the ultimate very slow decay. We attempted to fit a stretched exponential function to our long-time results, but could not achieve satisfactory agreement with our data.

9.7 Non-interacting Vortices with Columnar Defects

To compare the effects of uncorrelated point pins with those of extended, correlated defects on the flux line relaxation kinetics, we now investigate a system of non-interacting vortex lines in the presence of columnar pinning centers with a pinning potential strength $p = 0.05\epsilon_0$. We start by first considering the case of non-interacting flux lines relaxing in the presence of columnar defects. Figure 9.10 shows the relaxation curves for $B(t, 0)$ and $r_g^2(t)$ with their associated effective exponents $\beta_B(t)$ and $\beta_h(t)$. The time evolution of the mean-square displacement $B(t, 0)$ is slightly accelerated compared to the disorder-free case for times up to $t = 2^9$; see Fig. 9.1. This indicates that the initial trapping of vortices at linear pinning sites happens during this time regime. At later times, the effective exponent approaches the value of free flux lines $\beta_B = 0.5$, due to unbound vortex line wandering. In fact, only ~ 4 to 5% of the vortices are pinned at the end of our simulation time window.

As mentioned above, the average number of pinning sites per layer in our simulations is the same for point-like and columnar defects. Hence the combined lateral cross section along the z axis of all pinning sites is much larger for point than it is for columnar pins. Consequently,

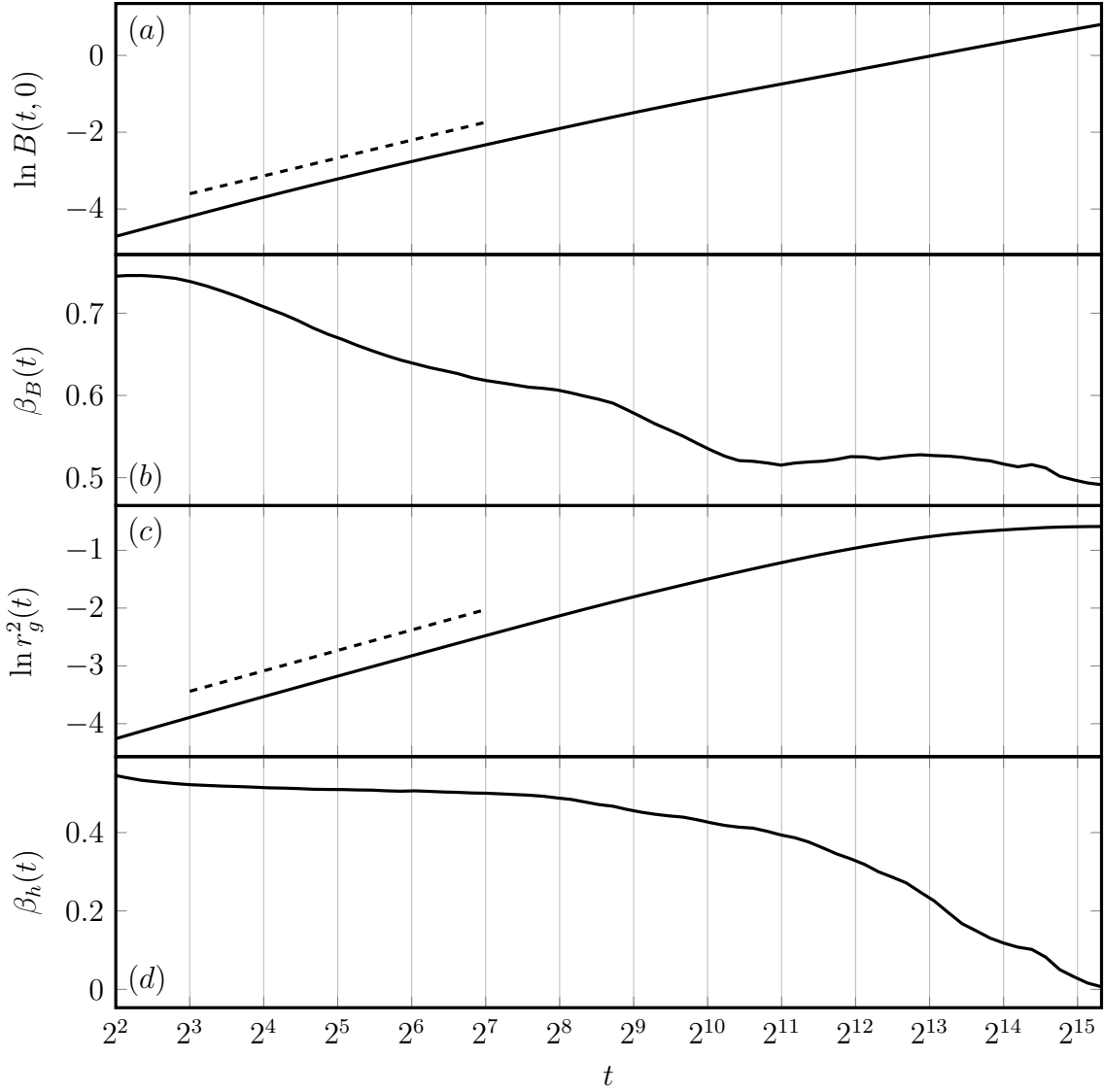


Figure 9.10: Relaxation behavior of (a) the flux line mean-square displacement $B(t, 0)$, (c) the squared gyration radius $r_g^2(t)$, and (b, d) the associated effective exponents β_B and β_h over time for non-interacting vortices subject to columnar pinning centers with $p = 0.05\epsilon_0$; data averaged over 10000 realizations. The dashed lines indicate the power laws with the mean effective exponents $\bar{\beta}_B \approx 0.672 \pm 0.037$ and $\bar{\beta}_h \approx 0.510 \pm 0.006$ over the time range $2^3 \leq t \leq 2^8$. (Adapted from reference [60], figure 12.)

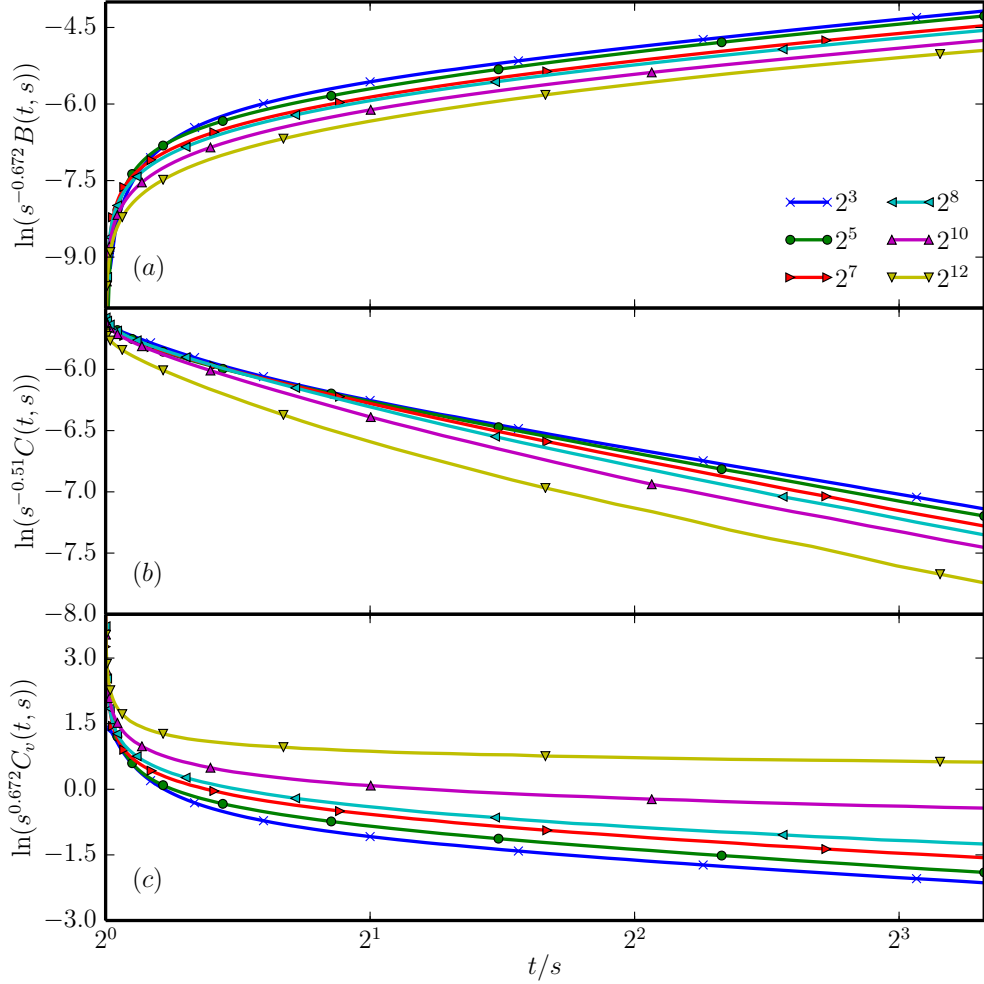


Figure 9.11: Relaxation of (a) the mean-square displacement, (b) the height autocorrelation function, and (c) the density autocorrelation in a system of non-interacting flux lines of length $L = 640$ subject to randomly distributed columnar pins of strength $p = 0.05\epsilon_0$; data averaged over 1000 realizations. Scaling attempts with the averaged effective exponents taken from Fig. 9.10 do not yield data collapse for $B(t,s)$ and $C_v(t,s)$. One achieves better data collapse at early waiting times s for the height autocorrelations $C(t,s)$. (*Adapted from reference [60], figure 13.*)

the probability for a vortex line to encounter a randomly placed columnar pin during what is essentially a random walk is much lower than in samples with randomly placed point defects. A flux line is therefore most likely to be initially captured by a single columnar defect (rather than multiple pinning sites, which would lead to vortex kink configurations) along a short length span, and subsequently becomes completely trapped at that pinning center; this yields rather small values for the final gyration radius, see Figs. 9.10(c) and 8.2(b). This is in stark contrast with samples containing uncorrelated point defects, where a single vortex line becomes captured by many pinning sites, which leads to a larger terminal radius of gyration because the line is stretched in random directions between multiple pins; see section 9.4. Thus, point-like pinning centers typically generate rough flux line configurations, whereas columnar defects straighten bound vortices. This fact can be expressed as an effective upward renormalization of the elastic line stiffness, reflected macroscopically as a diverging tilt modulus for the entire vortex system in the pinned Bose glass phase [64].

Comparing with the disorder-free system, the time evolution of the effective exponent of the radius of gyration $\beta_h(t)$ in the columnar defect case is also different: The exponent initially assumes a value 0.5 consistent with EW scaling. It begins to deviate from the EW value at $t \approx 2^9$, while in the non-disordered case this decrease does not occur until $t \approx 2^{12}$, see Fig. 9.10(d) and section 9.3. This is due to the fact that thermal line fluctuations inside a single columnar defect are confined to the pinning potential well, which causes early saturation of the equivalent EW growth process. An appreciable number of kinks and double-kinks due to vortices trapped at multiple columnar pinning sites would presumably alter this relaxation behavior, but the occurrence probability of kinks is rather small in our system, as explained above. At low temperatures, our non-interacting flux line system in the presence of correlated disorder forms a very dilute Bose glass, where the number of vortex lines is much less than the number of pinning sites.

Figure 9.11 shows the relaxation of the three two-time autocorrelation functions for different waiting times s as a function of the ratio t/s . We obtain data collapse for the height autocorrelation function $C(t, s)$ when scaling with the appropriately averaged effective aging exponent for early waiting times $s < 2^9$ and $t/s < 2$, which is consistent with the EW regime. The more global mean-square displacement $B(t, s)$ and the density autocorrelation $C_v(t, s)$ cannot similarly be scaled to obtain data collapse, because the effective exponent $\beta_B(t)$ is never even approximately constant throughout the entire observed time interval, as is evident in Fig. 9.10(b).

9.8 Interacting Vortex Lines with Columnar Defects

Next, we again turn on the repulsive vortex-vortex interactions. Similar to the disorder-free system and the samples with point pinning centers, see Secs. 9.5 and 9.6, caging effects accelerate vortex motion, and the shape of the single-time mean-square displacement $B(t, 0)$ and its associated effective exponent are hardly modified by the disorder; compare Fig. 9.12(a,b).

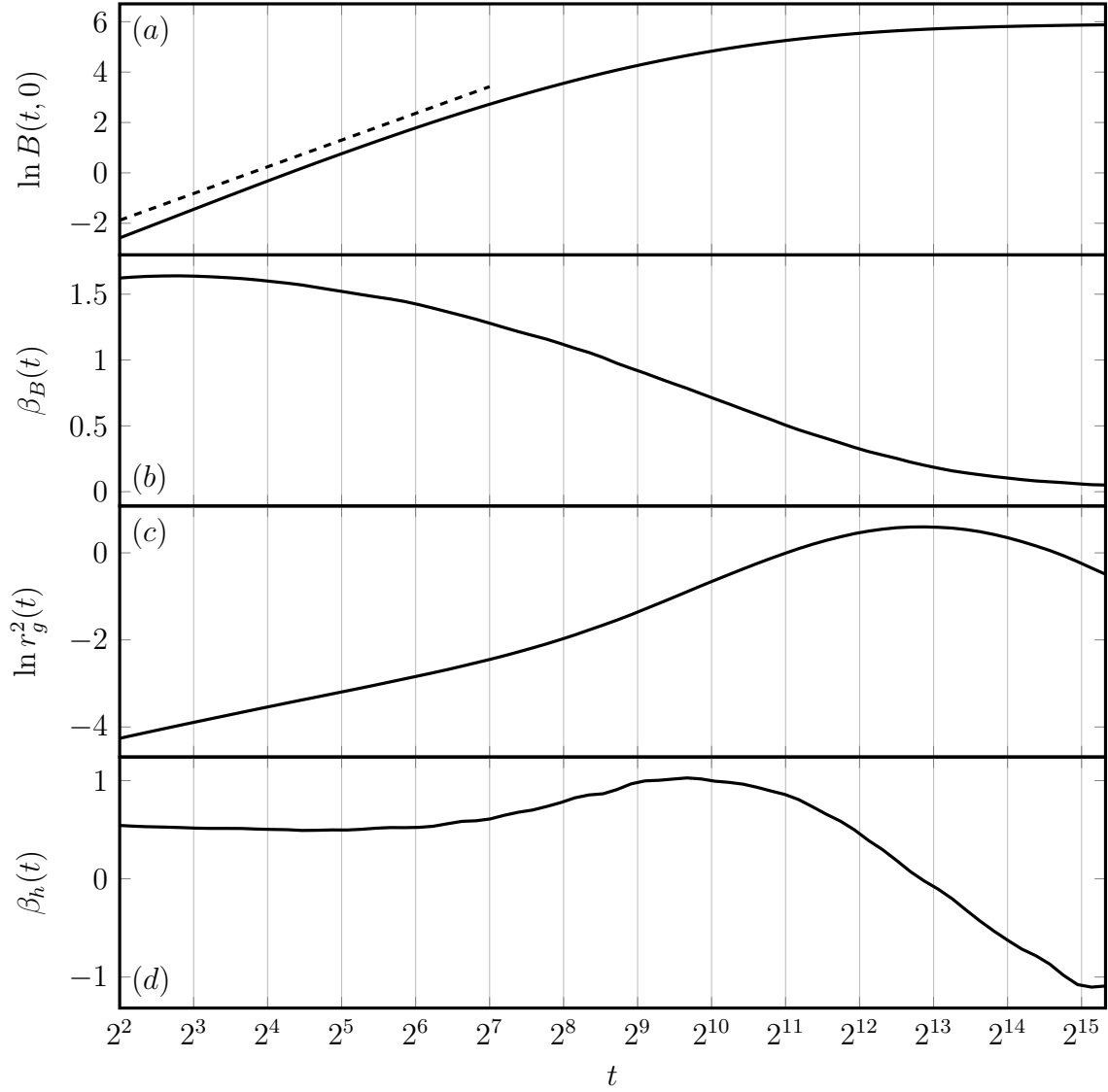


Figure 9.12: Non-equilibrium relaxation of (a) the flux line mean-square displacement $B(t, 0)$, (c) the squared gyration radius $r_g^2(t)$, and (b, d) the associated effective exponents β_B and β_h over time for interacting vortices in a system with columnar defects of strength $p = 0.05\epsilon_0$, averaged over 1000 realizations. The dashed line in (a) shows a power law with the mean effective exponent $\overline{\beta_B} \approx 1.53 \pm 0.11$, averaged over the time interval $2^2 \leq t \leq 2^7$. (Adapted from reference [60], figure 14.)

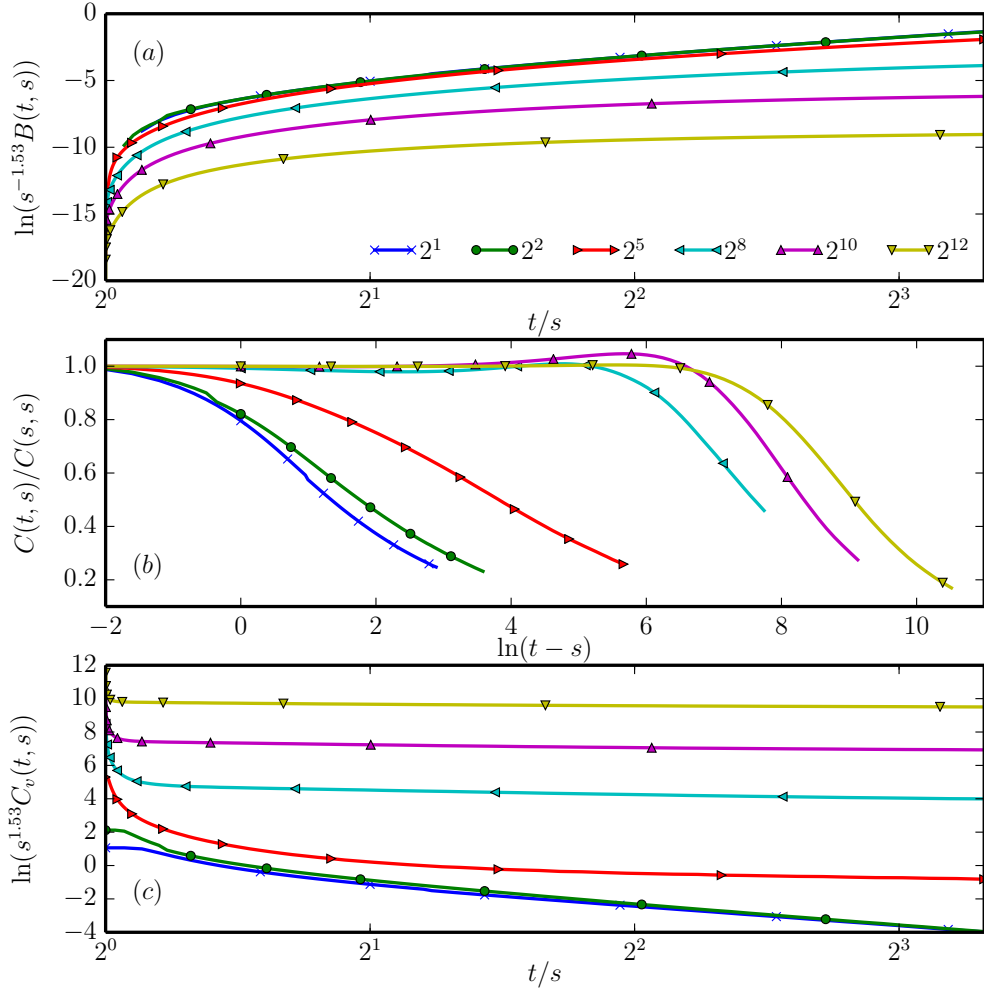


Figure 9.13: Relaxation of (a) the mean-square displacement, (b) the normalized height autocorrelation function, and (c) the density autocorrelation in a system of interacting vortices of length $L = 640$ with columnar defects of strength $p = 0.05\epsilon_0$; data averaged over 800 realizations. (*Adapted from reference [60], figure 15.*)

At very large times $t > 2^{12}$, $B(t, 0)$ becomes flatter and approaches a plateau owing to the confinement of vortex lines by attractive defects. This effect is rather more pronounced for columnar pins than for uncorrelated point defects. In fact, the maximal values of $B(t, 0)$ and $r_g^2(t)$ are both smaller in the case of correlated disorder, which indicates tighter binding to the pinning sites.

The radius of gyration also shows similar time evolution trends as compared to samples with point-like disorder; see Figs. 9.12(c) and 9.7(c). The effects of attractive columnar pinning sites set in later than for point-like pins, owing to the aforementioned differences in the encounter probability for flux lines and pinning centers. The accelerated growth of the gyration radius for $t > 2^9$ is due to the pinning at multiple sites and the subsequent formation of kinks, here facilitated by the strong repulsive forces. The non-monotonic behavior of $r_g^2(t)$ at times $t > 2^{13}$ is caused by the decay of previously formed kinks. The density autocorrelation $C_v(t, s)$ in Fig. 9.13(c) becomes flat for waiting times $s > 2^8$, which supports the interpretation that the vortex lines are essentially trapped by this time and the only remaining relaxation process is the decay of metastable kink configurations.

Figure 9.13(b) depicts the normalized height-height autocorrelation function of this system for different waiting times s . This function shows non-monotonic behavior, but in this situation it cannot stem from an effective mass, as we checked. The appearance of the maximum indicates a fundamental change in the lateral fluctuations. Although we do not yet fully understand this phenomenon, we tentatively relate this observation once again to the decay of kinks in the long-time limit.

9.9 Finite-Size Effects

Effects due to the finite flux line length are best analyzed in terms of the second crossover between the EW and saturation regimes for non-interacting vortices in the absence of pinning sites; see section 9.3. (The first crossover between the random thermal noise and the EW regimes only depends on the EW diffusion constant, which here corresponds to the vortex line tension.) The time at which this second crossover occurs depends on the square of the line length, $t_C = (L/24b_0)^2 2\pi/\epsilon_0$ (in the limit of large L) [103]. Our choice of $L = 640$ for most of the simulation scenarios in this paper thus provides a sufficiently long time window $t_C \approx 2^{12}$ to observe the competing effects of vortex interactions and pinning.

Of particular interest is the value of L at which the relaxational difference between point-like and columnar pinning sites becomes apparent. Figure 9.14 shows a comparison plot of $B(t, 0)$ and $r_g^2(t)$ for both columnar and point-like disorder for very short vortex lines with $L = 2$ and $L = 10$. In a purely two-dimensional system with $L = 1$, where the flux lines are reduced to point particles, there is obviously no difference between the two types of pinning sites. But already for $L = 2$ we observe differences in the long-time evolution of $B(t, 0)$. The curve for columnar defects can be almost exactly reproduced by using point pins and

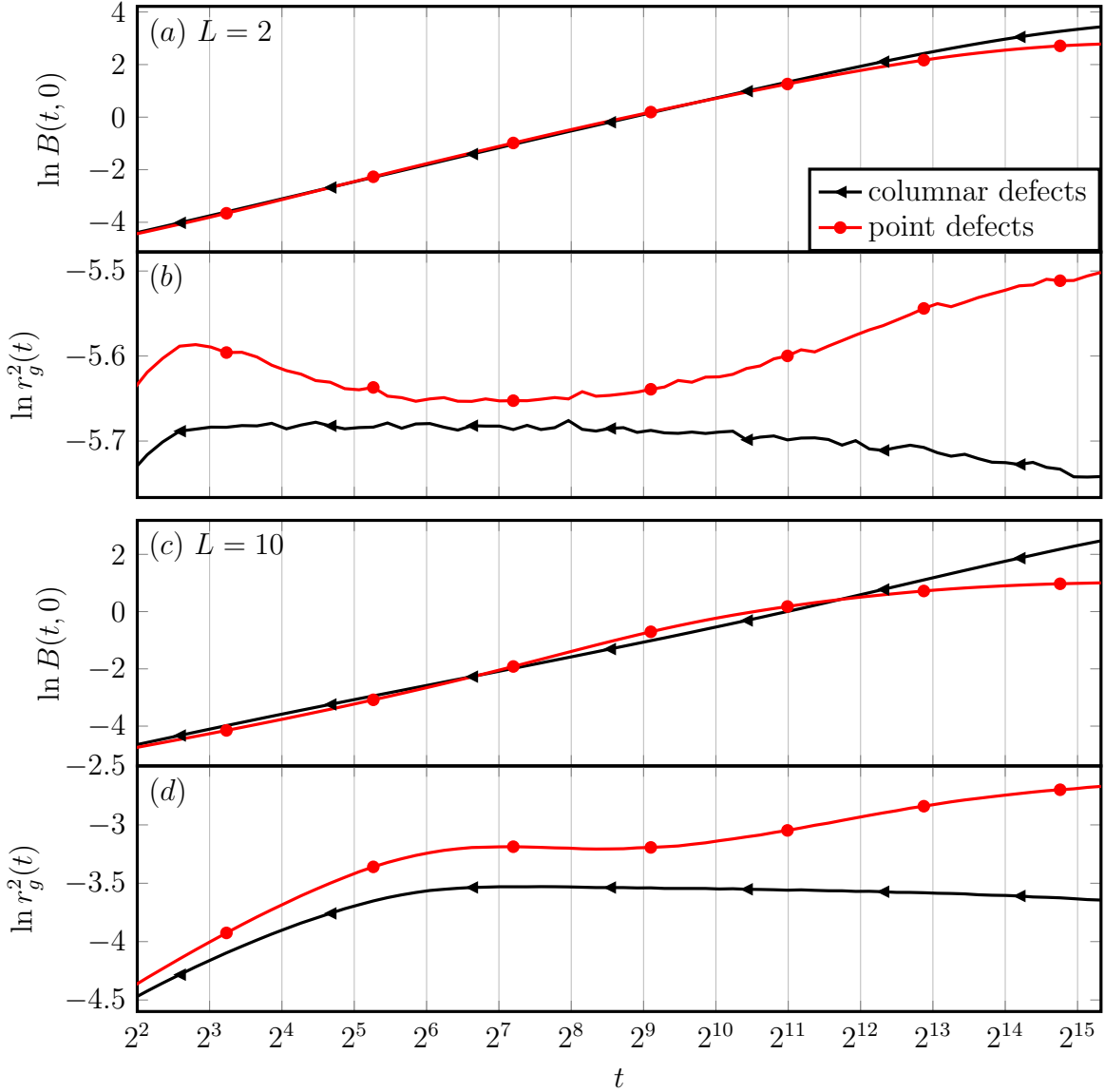


Figure 9.14: Non-equilibrium relaxation of the flux line mean-square displacement $B(t, 0)$ and the squared gyration radius $r_g^2(t)$ over time for non-interacting vortices in systems with point-like and columnar defects with identical pinning strengths $p = 0.05\epsilon_0$ for (a,b) $L = 2$ and (c,d) $L = 10$, averaged over 10000 realizations. (Adapted from reference [60], figure 16.)

halving the number of pinning sites. Hence the difference at $L = 2$ is largely due to the lower effective density of columnar disorder, as discussed in section 9.7. Yet this equivalence does not extend to the time evolution of the gyration radius $r_g^2(t)$, which displays small but significant qualitative differences for the two defect types throughout the simulation time window.

For $L = 10$, the long-time difference in $B(t, 0)$ between columnar and point-like pinning sites can also be explained by the lower effective density of columnar pinning sites. But the deviations appearing at much shorter times reflect genuine physical distinctions in the pinning behavior and ensuing relaxation kinetics.

Chapter 10

Conclusions

This chapter was adapted from our publication, reference [60], with modifications to the text.

We have investigated the differences in the non-equilibrium relaxation features between systems of magnetic flux lines in the presence of point-like and columnar disorder. Proceeding in a systematic way, and considering different limiting cases, allowed us to disentangle the distinct contributions originating from the attractive pinning centers, the repulsive mutual vortex interactions, and the line tension.

We validated both our Langevin Molecular Dynamics simulation code and the Monte Carlo algorithm used in previous studies in a genuine out-of-equilibrium setting by comparing the steady-state vortex velocity and radius of gyration as a function of an external driving force to results from Monte Carlo simulations. As discussed in Sec. 7.3, both these simulation methods need to be tested and validated when applied to non-equilibrium situations. We found that the pinning potential strength in MC is slightly renormalized as compared to LMD due to the (inevitable) choice of a maximal MC step size.

The introduction of columnar instead of point-like pinning sites dramatically changes the steady-state properties. As expected, the critical depinning force is enhanced by approximately an order of magnitude. The radius of gyration is suppressed via vortex line confinement in columnar pinning sites for a driving force well below the critical depinning force. At the transition, partial depinning leads to the formation of half-loops and kinks in the vortex lines and thus to a sharp increase in the radius of gyration. At even higher driving forces, flux line motion is not influenced by pinning.

We carefully studied the relaxation towards equilibrium of a system of initially perfectly straight and randomly placed vortex lines under various conditions by observing single- and two-time quantities to again compare the effects of uncorrelated point pins and correlated extended defects, and to further validate our LMD code against previously published MC results. We investigated the possibility of data collapse and, hence, a simple aging scenario, by appropriately scaling our two-time quantities. We started with free, non-interacting vortex

lines and showed that our results completely agreed with the MC data and the predictions from the Edwards-Wilkinson interface growth model. We then systematically introduced attractive pinning centers and mutual repulsive vortex interactions. Caging effects due to vortex-vortex interactions lead to a considerable acceleration in the relaxation of global quantities, such as the single-time mean-square vortex displacement. A recent study revealed that the MC two-time height-height autocorrelation function for a system with interactions and point-like disorder displayed non-monotonic behavior (shown in Ref. [67]). Comparing with data obtained with an additional inertial term in our LMD algorithm, we argued that these oscillations stem from an effective mass generated by the introduction of a maximal MC step length.

We demonstrated that the relaxation behavior of vortex lines depends crucially on the type of disorder. The vortex and Bose glass phases display complex non-universal relaxation features that are highly dependent on the material parameters. Once a deeper understanding of the transient behavior has been established, detailed information contained in such time-dependent quantities could be used to characterize material properties and specific samples. Point-like disorder binds vortices to many pinning sites at once, while columnar defects capture entire flux lines. When comparing these two defect types, one needs to take into account the difference in the effective pin density and thus the distinct probability of vortex line elements to become trapped. One may characterize the vortex glass phase through the roughness exponent χ of the spatial height-height correlation function along the strongly fluctuating flux line trajectory. In contrast, correlated linear defects effectively enhance the elastic line stiffness and hence straighten the trapped vortices in the Bose glass phase.

We plan to expand our study to the transient properties of driven vortex lines. The resulting relaxation then is towards a genuine non-equilibrium state in contrast to the relaxation towards equilibrium, which I presented in this work. Possible protocols would include an initial relaxation at a high driving force (in the depinning regime) and a subsequent quench onto the depinning transition.

Other avenues for further studies include the study of different and more realistic initial conditions, such as magnetic field or temperature quenches. Changing the magnetic field is equivalent to changing the density of vortex lines, hence the simple removal of vortex lines from, or their addition to the computational domain corresponds to a magnetic field quench.

Additionally, we want to investigate the depinning behavior and time distributions of vortex line elements in a medium with randomly distributed and correlated pinning sites. There exist theoretical predictions for an algebraic long-time decay of the depinning time distribution [109], as well as previously performed computer simulation studies [110].

This project demonstrates quite convincingly that the interplay between many energy scales leads to complex and rich physics. In order to understand emerging effects one needs to study different limits and time regimes, which requires the careful design and investigation of appropriate quantities.

Chapter 11

Bibliography

- [39] V. L. Ginzburg and L. D. Landau. “On superconductivity theory”. *Zhurnal Eksperimental'noi i Teoreticheskoi Fiziki* **20** 1064 (1950) (cit. on pp. 41, 46, 49).
- [40] G. Blatter, V. B. Geshkenbein, A. I. Larkin, and V. M. Vinokur. “Vortices in high-temperature superconductors”. *Reviews of Modern Physics* **66** 1125–1388 (1994) (cit. on pp. 42, 43, 54).
- [41] M. Tinkham. *Introduction to superconductivity*. New York, NY, McGraw-Hill Publishing Co (1996) (cit. on pp. 42, 46, 48–50, 52).
- [42] E. Thuneberg, J. Kurkijärvi, and D. Rainer. “Pinning of a Vortex Line to a Small Defect in Superconductors”. *Physical Review Letters* **48** 1853–1856 (1982) (cit. on pp. 42, 52).
- [43] A. A. Abrikosov. “On the Magnetic Properties of Superconductors of the Second Group”. *Soviet Physics JETP* **5** (1957) (cit. on pp. 43, 49, 51).
- [44] U Essmann and H Träuble. “The direct observation of individual flux lines in type II superconductors”. *Physics Letters A* **24** 526–527 (1967) (cit. on p. 43).
- [45] D. R. Nelson. “Vortex Entanglement in High- T_c Superconductors”. *Physical Review Letters* **60** 1973–1976 (1988) (cit. on p. 43).
- [46] D. R. Nelson and H. Seung. “Theory of melted flux liquids”. *Physical Review B* **39** 9153–9174 (1989) (cit. on p. 43).
- [47] D. R. Nelson. “Statistical mechanics of flux lines in high- T_c superconductors”. *Journal of Statistical Physics* **57** 511–530 (1989) (cit. on p. 43).
- [48] M. P. A. Fisher. “Vortex-glass superconductivity: A possible new phase in bulk high- T_c oxides”. *Physical Review Letters* **62** 1415–1418 (1989) (cit. on p. 43).
- [49] D. S. Fisher, M. P. A. Fisher, and D. Huse. “Thermal fluctuations, quenched disorder, phase transitions, and transport in type-II superconductors”. *Physical Review B* **43** 130–159 (1991) (cit. on p. 43).

- [50] M. Feigel'man, V. Geshkenbein, A. Larkin, and V. M. Vinokur. "Theory of collective flux creep". *Physical Review Letters* **63** 2303–2306 (1989) (cit. on p. 43).
- [51] T. Nattermann. "Scaling approach to pinning: Charge density waves and giant flux creep in superconductors". *Physical Review Letters* **64** 2454–2457 (1990) (cit. on p. 43).
- [52] T. Giamarchi and P. Le Doussal. "Elastic theory of pinned flux lattices". *Physical Review Letters* **72** 1530–1533 (1994) (cit. on p. 43).
- [53] T. Giamarchi and P. Le Doussal. "Elastic theory of flux lattices in the presence of weak disorder". *Physical Review B* **52** 1242–1270 (1995) (cit. on p. 43).
- [54] J. Kierfeld, T. Nattermann, and T. Hwa. "Topological order in the vortex-glass phase of high-temperature superconductors". *Physical Review B* **55** 626–629 (1997) (cit. on p. 43).
- [55] D. Fisher. "Stability of Elastic Glass Phases in Random Field XY Magnets and Vortex Lattices in Type-II Superconductors". *Physical Review Letters* **78** 1964–1967 (1997) (cit. on p. 43).
- [56] T. Giamarchi and P. Le Doussal. "Phase diagrams of flux lattices with disorder". *Physical Review B* **55** 6577–6583 (1997) (cit. on p. 43).
- [57] T Klein, I Journaud, S Blanchard, J Marcus, R Cubitt, T Giamarchi, and P Le Doussal. "A Bragg glass phase in the vortex lattice of a type II superconductor." *Nature* **413** 404–406 (2001) (cit. on p. 43).
- [58] G. Menon. "Phase behavior of type-II superconductors with quenched point pinning disorder: A phenomenological proposal". *Physical Review B* **65** 104527 (2002) (cit. on p. 43).
- [59] S. Banerjee, A. Grover, M. Higgins, G. I. Menon, P. Mishra, D. Pal, S. Ramakrishnan, T. Chandrasekhar Rao, G. Ravikumar, V. Sahni, S. Sarkar, and C. Tomy. "Disordered type-II superconductors: a universal phase diagram for low-T_c systems". *Physica C: Superconductivity* **355** 39–50 (2001) (cit. on p. 43).
- [60] U. Dobramysl, H. Assi, M. Pleimling, and U. C. Täuber. "Relaxation Dynamics in Type-II Superconductors with Point-like and Correlated Disorder". *European Physics Journal B* (2013) (cit. on pp. 43, 58, 59, 65, 66, 68, 69, 71, 72, 74–78, 80, 81, 83, 85).
- [61] L. Civale, A. Marwick, T. Worthington, M. Kirk, J. Thompson, L. Krusin-Elbaum, Y. Sun, J. Clem, and F. Holtzberg. "Vortex confinement by columnar defects in $YBa_2Cu_3O_7$ crystals: Enhanced pinning at high fields and temperatures". *Physical Review Letters* **67** 648–651 (1991) (cit. on pp. 43, 57).
- [62] D. R. Nelson and V. M. Vinokur. "Boson localization and pinning by correlated disorder in high-temperature superconductors". *Physical Review Letters* **68** 2398–2401 (1992) (cit. on p. 43).

- [63] I. F. Lyuksyutov. “Flux Pinning by Linear Defects”. *Europhysics Letters (EPL)* **20** 273–278 (1992) (cit. on p. 43).
- [64] D. R. Nelson and V. M. Vinokur. “Boson localization and correlated pinning of superconducting vortex arrays”. *Physical Review B* **48** 13060–13097 (1993) (cit. on pp. 43, 44, 53, 57, 79).
- [65] M. P. A. Fisher, P. B. Weichmann, G. Grinstein, and D. S. Fisher. “Boson localization and the superfluid-insulator transition”. *Physical Review B* **40** 546–570 (1989) (cit. on p. 43).
- [66] U. C. Täuber and D. R. Nelson. “Superfluid bosons and flux liquids: disorder, thermal fluctuations, and finite-size effects”. *Physics Reports* **289** 157–233 (1997) (cit. on p. 43).
- [67] M. Pleimling and U. C. Täuber. “Relaxation and glassy dynamics in disordered type-II superconductors”. *Physical Review B* **84** 174509 (2011) (cit. on pp. 44, 61, 62, 64, 67, 70, 73, 86).
- [68] T. Klongcheongsan, T. J. Bullard, and U. C. Täuber. “Nonequilibrium steady states of driven magnetic flux lines in disordered type-II superconductors”. *Superconductor Science and Technology* **23** 025023 (2010) (cit. on pp. 44, 54, 55).
- [69] L. C. E. Struik. *Physical Aging in Amorphous Polymers and Other Materials*. Amsterdam, Elsevier (1978) (cit. on p. 44).
- [70] M. Henkel, M. Pleimling, and E. Sanctuary, eds. *Ageing and the Glass Transition*. Vol. 716. Lecture Notes in Physics. Berlin, Springer (2007) (cit. on p. 44).
- [71] M. Henkel and M. Pleimling. *Non-Equilibrium Phase Transitions, Vol.2: Ageing and Dynamical Scaling Far from Equilibrium*. Berlin, Springer (2010) (cit. on p. 44).
- [72] L. F. Cugliandolo. “Dynamics of glassy systems”. *Slow Relaxation and Non Equilibrium Dynamics in Condensed Matter*. Ed. by J. L. Barrat, J. Dalibart, J. Kurchan, and M. Feigel'man. Berlin, Springer (2003) (cit. on p. 44).
- [73] M. Henkel and M. Pleimling. “No Title”. *Rugged Free Energy Landscapes: Common Computational Approaches in Spin Glasses, Structural Glasses and Biological Macromolecules*. Ed. by W. Janke. Vol. 736. Lecture Notes in Physics. Berlin, Springer (2008), p. 107 (cit. on p. 44).
- [74] X. Du, G. Li, E. Y. Andrei, M. Greenblatt, and P. Shuk. “Ageing memory and glassiness of a driven vortex system”. *Nature Physics* **3** 111–114 (2007) (cit. on p. 44).
- [75] M. Nicodemi and H. J. Jensen. “Equilibrium and off-equilibrium dynamics in a model for vortices in superconductors”. *Physical Review B* **65** 144517 (2002) (cit. on p. 44).
- [76] M. Nicodemi and H. J. Jensen. “Ageing and memory phenomena in magnetic and transport properties of vortex matter”. *Journal of Physics A: Mathematical and General* **34** 8425–8443 (2001) (cit. on p. 44).

- [77] H. J. Jensen and M. Nicodemi. “Off-equilibrium properties of vortex creep in superconductors”. *Europhysics Letters (EPL)* **54** 566–572 (2001) (cit. on p. 44).
- [78] M. Nicodemi and H. J. Jensen. “Creep of Superconducting Vortices in the Limit of Vanishing Temperature: A Fingerprint of Off-Equilibrium Dynamics”. *Physical Review Letters* **86** 4378–4381 (2001) (cit. on p. 44).
- [79] S. Bustingorry, L. Cugliandolo, and D. Domínguez. “Out-of-Equilibrium Dynamics of the Vortex Glass in Superconductors”. *Physical Review Letters* **96** 027001 (2006) (cit. on p. 44).
- [80] S. Bustingorry, L. Cugliandolo, and D. Domínguez. “Langevin simulations of the out-of-equilibrium dynamics of vortex glasses in high-temperature superconductors”. *Physical Review B* **75** 024506 (2007) (cit. on pp. 44, 64).
- [81] L. D. Landau. “No Title”. *Zhurnal Eksperimental'noi i Teoreticheskoi Fiziki* **7** 19–32 (1937) (cit. on p. 46).
- [82] L. N. Cooper. “Bound Electron Pairs in a Degenerate Fermi Gas”. *Physical Review* **104** 1189–1190 (1956) (cit. on p. 46).
- [83] J. Bardeen, L. N. Cooper, and J. R. Schrieffer. “Microscopic Theory of Superconductivity”. *Physical Review* **106** 162–164 (1957) (cit. on p. 46).
- [84] J. Bardeen, L. N. Cooper, and J. R. Schrieffer. “Theory of Superconductivity”. *Physical Review* **108** 1175–1204 (1957) (cit. on p. 46).
- [85] L. P. Gor'kov. “Microscopic derivation of the Ginzburg-Landau equations in the theory of superconductivity”. *Soviet Physics JETP* **9** 1364–1367 (1959) (cit. on p. 46).
- [86] P.-G. de Gennes. *Superconductivity of metals and alloys*. New York, NY, W.A. Benjamin (1966) (cit. on p. 46).
- [87] F. London and H London. “The Electromagnetic Equations of the Supraconductor”. *Proceedings of the Royal Society A: Mathematical, Physical and Engineering Sciences* **149** 71–88 (1935) (cit. on p. 47).
- [88] A. A. Abrikosov. “Vliyanie razmerov na kriticheskoe pole sverkhprovodnikov vtoroi gruppy”. *Doklady Akademii Nauk SSSR* **86** 489 (1952) (cit. on p. 49).
- [89] A. Zee. *Quantum Field Theory in a Nutshell*. Princeton, NJ, Princeton University Press (2003) (cit. on p. 50).
- [90] F London. “On the Problem of the Molecular Theory of Superconductivity”. *Physical Review* **74** 562–573 (1948) (cit. on p. 51).
- [91] W. H. Kleiner, L. M. Roth, and S. H. Autler. “Bulk Solution of Ginzburg-Landau Equations for Type II Superconductors: Upper Critical Field Region”. *Physical Review* **133** A1226–A1227 (1964) (cit. on pp. 51, 52).
- [92] J. Das, T. J. Bullard, and U. C. Täuber. “Vortex transport and voltage noise in disordered superconductors”. *Physica A: Statistical Mechanics and its Applications* **318** 48–54 (2003) (cit. on pp. 53, 54).

- [93] T. J. Bullard, J. Das, G. L. Daquila, and U. C. Täuber. “Vortex washboard voltage noise in type-II superconductors”. *The European Physical Journal B* **65** 469–484 (2008) (cit. on pp. 54, 55).
- [94] J. Bardeen and M. Stephen. “Theory of the Motion of Vortices in Superconductors”. *Physical Review* **140** A1197–A1207 (1965) (cit. on p. 54).
- [95] A Brass and H. J. Jensen. “Algorithm for computer simulations of flux-lattice melting in type-II superconductors”. *Physical Review B* **39** 9587–9590 (1989) (cit. on p. 54).
- [96] V. Gotcheva, A. Wang, and S. Teitel. “Lattice Gas Dynamics: Application to Driven Vortices in Two Dimensional Superconductors”. *Physical Review Letters* **92** 247005 (2004) (cit. on p. 55).
- [97] V. Gotcheva, Y. Wang, A. Wang, and S. Teitel. “Continuous-time Monte Carlo and spatial ordering in driven lattice gases: Application to driven vortices in periodic superconducting networks”. *Physical Review B* **72** 064505 (2005) (cit. on p. 55).
- [98] M. M. Abdelhadi and K. A. Ziq. “The behaviour of the flux flow resistance in YBCO / (Ag₂O)_x”. *Superconductor Science and Technology* **7** 99–102 (1994) (cit. on p. 55).
- [99] D. S. Fisher. “Collective transport in random media: from superconductors to earthquakes”. *Physics Reports* **301** 113–150 (1998) (cit. on pp. 56, 57).
- [100] S. F. Edwards and D. R. Wilkinson. “The Surface Statistics of a Granular Aggregate”. *Proceedings of the Royal Society A* **381** 17–31 (1982) (cit. on p. 63).
- [101] A. Röthlein, F. Baumann, and M. Pleimling. “Erratum: Symmetry-based determination of space-time functions in nonequilibrium growth processes [Phys. Rev. E 74, 061604 (2006)]”. *Physical Review E* **76** 019901 (2007) (cit. on p. 64).
- [102] Y.-L. Chou and M. Pleimling. “Characterization of non-equilibrium growth through global two-time quantities”. *Journal of Statistical Mechanics: Theory and Experiment* **2010** P08007 (2010) (cit. on p. 64).
- [103] Y.-l. Chou, M. Pleimling, and R. K. P. Zia. “Changing growth conditions during surface growth”. *Physical Review E* **80** 061602 (2009) (cit. on pp. 64, 82).
- [104] T. Nattermann and S. Scheidl. “Vortex-glass phases in type-II superconductors”. *Advances in Physics* **49** 607–704 (2000) (cit. on p. 70).
- [105] M. Lässig. “Quantized Scaling of Growing Surfaces”. *Physical Review Letters* **80** 2366–2369 (1998) (cit. on p. 70).
- [106] J. Iguain, S. Bustingorry, A. Kolton, and L. Cugliandolo. “Growing correlations and aging of an elastic line in a random potential”. *Physical Review B* **80** 094201 (2009) (cit. on p. 70).
- [107] J. A. Izaguirre, D. P. Catarello, J. M. Wozniak, and R. D. Skeel. “Langevin stabilization of molecular dynamics”. *Journal of Chemical Physics* **114** 2090 (2001) (cit. on p. 76).

- [108] A. Brünger, C. L. Brooks, and M. Karplus. “Stochastic boundary conditions for molecular dynamics simulations of ST2 water”. *Chemical Physics Letters* **105** 495–500 (1984) (cit. on pp. 76, 99).
- [109] V. Vinokur, M. Marchetti, and L.-W. Chen. “Glassy Motion of Elastic Manifolds”. *Physical Review Letters* **77** 1845–1848 (1996) (cit. on p. 86).
- [110] M. S. de la Lama, J. M. López, J. J. Ramasco, and M. A. Rodríguez. “Activity statistics of a forced elastic string in a disordered medium”. *Journal of Statistical Mechanics: Theory and Experiment* **2009** P07009 (2009) (cit. on p. 86).
- [111] U. C. Täuber. *Critical Dynamics*. unpublished (cit. on p. 93).
- [112] N. Metropolis, A. W. Rosenbluth, M. N. Rosenbluth, A. H. Teller, and E. Teller. “Equation of State Calculations by Fast Computing Machines”. *The Journal of Chemical Physics* **21** 1087 (1953) (cit. on p. 95).

Appendix A

Monte Carlo Simulations

Monte Carlo simulations represent a numerical method to find approximate solutions to the master equation of a system. In its most general form a master equation reads

$$\frac{\partial P(x, t)}{\partial t} = \int dx' [P(x', t)W(x' \rightarrow x, t) - P(x, t)W(x \rightarrow x', t)], \quad (\text{A.1})$$

where $P(x, t)$ is the time dependent probability distribution of a vector of random variables x [111]. The collection of random variables in this vector represents the current state of the system. Transitions between the states x and x' are governed by the transition rates, $W(x \rightarrow x', t)$.

The master equation (A.1) is generally impossible to solve exactly, especially if the state vector x has many components and/or the transition rates include non-linear terms. By starting from some realization of the initial condition $P(x, t = 0)$, and implementing the transitions between states, single Monte Carlo simulation runs then yield realizations of the time-dependent probability density $P(x, t)$. We can then combine a large number of runs to reconstruct arbitrary moments of the probability distribution (although higher moments will inevitably need more realizations to achieve the desired accuracy). In practice, however, one calculates observables and correlation directly from simulation data.

In Monte Carlo simulations, the system traverses between states by picking a random component of the state vector and letting it make an allowed transition (that may influence other components as well), according to the rules of the system. The probability of that transition occurring is then determined via the transition rates $W(x \rightarrow x', t)$. The simulation algorithm generates a random number between zero and one and rejects the move if the number is larger than this probability.

It should be noted that the time axis generated by a Monte Carlo simulation algorithm is artificial. It is determined by the transition rates and depends on the details of the specific algorithm. It is usually possible to relate the time scale of simulation results with

experimental time scales via a phenomenological factor, however there is no exact one-to-one relationship between them.

A.1 Population Dynamics

In population dynamics, one usually employs Monte Carlo simulations to simulate large numbers of interacting species beyond the mean-field limit. The method is quite important in this field, since stochasticity often plays a crucial role in these systems, as I discussed in section 1.4. Here, the method is also often called agent-based modeling, or individual-based simulations.

As in the case of the Lotka-Volterra model described in section 1.2, population dynamics models (and models for chemical reactions) deal with N species A_i with $i = 1, \dots, N$, that are interacting via M rules of the form

$$\sum_{i=1}^N c_{ji} A_i \xrightarrow{k_j} \sum_{k=1}^N d_{jk} A_k. \quad (\text{A.2})$$

The coefficients c_{ji} and d_{ji} are integer-valued and positive, and describe the number of particles of species i are used and produced by rule j , respectively. The reaction rate k_j determines the probability for the application of rule j , and might be a dynamic function of the participating particles (see section 2.1).

In well-mixed, zero-dimensional simulations, the Monte Carlo algorithm is straightforward:

1. Set the fractional step counter C to zero.
2. A random particle is picked out of a list of all particles of all species. Determine the species of the particle as i .
3. Determine which rules the particle can participate in via the rule $c_{ji} > 0$.
4. Iterate through the possible rules:
 - (a) Check if the conditions for rule j are fulfilled (i.e. enough particles, according to c_{jk} , of the other k species exist).
 - (b) Generate a random number r between zero and one. If $r < k_j$ is true, apply the rule by removing $\min(0, c_{jk} - d_{jk})$ and creating $\max(0, d_{jk} - c_{jk})$ particles of each species k .
5. Add the fraction $1/N$ to the fractional step counter C , where N is the total number of particles. If $C < 1$, jump to step 2.
6. Advance time by one Monte Carlo step and jump to step 1.

The application order of the rules might be important for the dynamics and it is important to test if there is an influence on the observables.

For spatial Monte Carlo simulations on a lattice, we need to introduce modifications to the algorithm above. There are two fundamentally different types of particle movement: particle swapping and simple diffusion. In the present work only the latter was used, hence I will only discuss this case. There needs to be an additional particle movement step before the model rules are applied. If there is a maximum number of particles per lattice site, the simulation needs to determine if there is enough space on all of the next-neighbor lattice sites and constructs a list of the possible movement directions. One the directions is then chosen at random and the particle moved from its old position to the new position. In our simulations, the rules in step 4 above are applied locally, on-site, as if the lattice site itself represented a zero-dimensional system.

A.2 Metropolis Monte Carlo

When simulating the equilibration of a system that is described by a Hamiltonian H and is coupled to a heat bath with a temperature T , one needs to choose appropriate transition rates $W(x \rightarrow x', t)$. A popular choice is the Metropolis update rule [112]. Here, I restrict the description to systems in which the random variables are continuous spatial coordinates of components of the system, such as in the elastic line Hamiltonian (7.18) described in section 7.2. Hence, the algorithm can be summarized as follows:

1. Choose a random particle i at position \vec{r}_i out of the N particles in the system.
2. Generate a random “jump” vector $\Delta\vec{r}$ with $|\Delta\vec{r}| < \alpha$, but otherwise uniformly distributed. This jump distance cut-off α has to be smaller than the smallest features of the system, to prevent unphysical smoothing effects, see section 7.3.
3. Calculate the change in energy ΔE of the system when the particle is moved to its new position $\vec{r}_i + \Delta\vec{r}$.
4. Generate a random number h in the range between zero and one. Accept the step if $h < \max(1, \exp[-\Delta E/k_B T])$ and move the particle to the new position. If the condition is not fulfilled, leave the particle at its old position.
5. If N particles have been chosen, advance the Monte Carlo time counter by one.
6. Jump to step 1.

The Metropolis update rule includes a Boltzmann factor to determine the probability of acceptance of a step that increases the system energy. It serves as the coupling to the temperature bath with temperature T . It should be noted that the choice of the Boltzmann

factor is by no means unique and that there are a number of possibilities to implement the coupling to an external temperature reservoir. In addition, this choice of update rule is only well-defined for a relaxation into the equilibrium state. For genuine out-of-equilibrium systems, such as driven vortex lines, where the system relaxes into a non-equilibrium steady-state, the situation is less clear and the algorithm needs to be validated by comparing with different methods; see sections 7.3 and 8.1.

Appendix B

Langevin Molecular Dynamics

In this appendix I discuss the Langevin Molecular Dynamics algorithm we use for our studies of vortex lines in type-II superconductors, see section 7.2, in detail. Our model uses the Hamiltonian (7.18) to describe the energetics of interacting elastic lines with trajectories $\vec{r}(z)$, i.e. the $x - y$ position \vec{r} as a function of the third dimension z .

In order to simulate the dynamics, we need to find a suitable spatial discretization scheme. The class of type-II superconductors that are used in technological applications consists of the ceramic high-temperature materials, which are highly anisotropic; the crystallographic c -direction of the unit cell is much larger than the a and b -directions. Hence, the superconducting medium is layered along the c -axis, which is also the natural choice of discretization in this system; see figure B. Plugging in the form of the pinning potential and the interaction potential, the Hamiltonian in this discrete setting thus becomes

$$H(\{\vec{r}_{i,l}\}) = \sum_{i=1}^N \sum_{l=0}^{L/b_0} \left\{ \frac{\tilde{\epsilon}_1}{2b_0} |\vec{r}_{i,l-1} + \vec{r}_{i,l+1} - 2\vec{r}_{i,l}|^2 - \frac{p}{2} \sum_{\alpha=1}^{N_D} \delta_{l,l_\alpha} \left[1 - \tanh \left(5 \frac{|\vec{r}_{i,l} - \vec{r}_\alpha| - b_0}{b_0} \right) \right] + 2\epsilon_0 b_0 \sum_{j=i+1}^N K_0 \left(\frac{|\vec{r}_{i,l} - \vec{r}_{j,l}|}{\lambda_{ab}} \right) \right\}. \quad (\text{B.1})$$

The index l enumerates the layers, while i and j iterate over vortex lines, with $\vec{r}_{i,l}$ denoting the position of the element in the l th layer of the i th vortex line. Pinning sites indices are denoted by α , with \vec{r}_α being the in-plane position of the pinning site α , while l_α is the index of the layer of the site.

The pinning potential, shown in the second line of equation (B.1), has the shape of a smooth potential well of size b_0 , displayed in figure B.2(a). The potential is cut off at a distance $r/b_0 = 2$. The repulsive interaction potential consists of a zeroth order modified Bessel

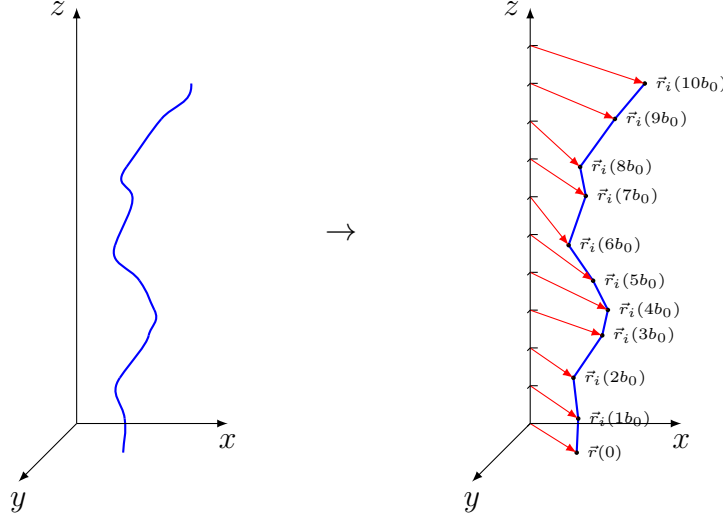


Figure B.1: Vortex line discretization scheme. The smooth vortex line on the left is discretized along the z -axis into elastically coupled point particles with coordinates $\vec{r}_i(lb_0)$, where l represents the index of the $x - y$ plane in which the particle can move. The spacing between planes is given by b_0 .

function of the second kind, with a characteristic length of λ_{ab} , the magnetic penetration depth.

This scheme leads to a force on a single vortex line element $\vec{r}_{i,l}$, given by the expression

$$\begin{aligned} \vec{F}_{i,l}(\vec{r}_{i,l}) = -\frac{dH}{d\vec{r}_{i,l}} &= \frac{\tilde{\epsilon}}{b_0}(2\vec{r}_{i,l} - \vec{r}_{i,l-1} - \vec{r}_{i,l+1}) \\ &- \frac{5p}{4} \sum_{\alpha=1}^{N_D} \delta_{l,l_\alpha} \frac{\vec{r}_{i,l} - \vec{r}_\alpha}{|\vec{r}_{i,l} - \vec{r}_\alpha|} \cosh^{-2}\left(5\frac{|\vec{r}_{i,l} - \vec{r}_\alpha| - b_0}{b_0}\right) \\ &+ 2\frac{\epsilon_0 b_0}{\lambda_{ab}} \sum_{j=i+1}^N K_1\left(\frac{|\vec{r}_{i,l} - \vec{r}_{j,l}|}{\lambda_{ab}}\right). \end{aligned} \quad (\text{B.2})$$

As already explained in section 7.2.2, we employ a simple over-damped Langevin equation of motion in order to simulate the time evolution of vortex line elements

$$\eta \frac{d\vec{r}_{i,l}(t)}{dt} = \vec{F}_{i,l}(\{\vec{r}_{i,l}(t)\}) + \vec{f}_i(t, z).$$

The discretization in time of this equation is straightforward: We define the instantaneous velocity as $v_{i,l}(t) \equiv \frac{dr_{i,l}(t)}{dt}$. The stepping algorithm then becomes

1. Initialize the vortex line element position arrays $\vec{r}_{i,l}$.

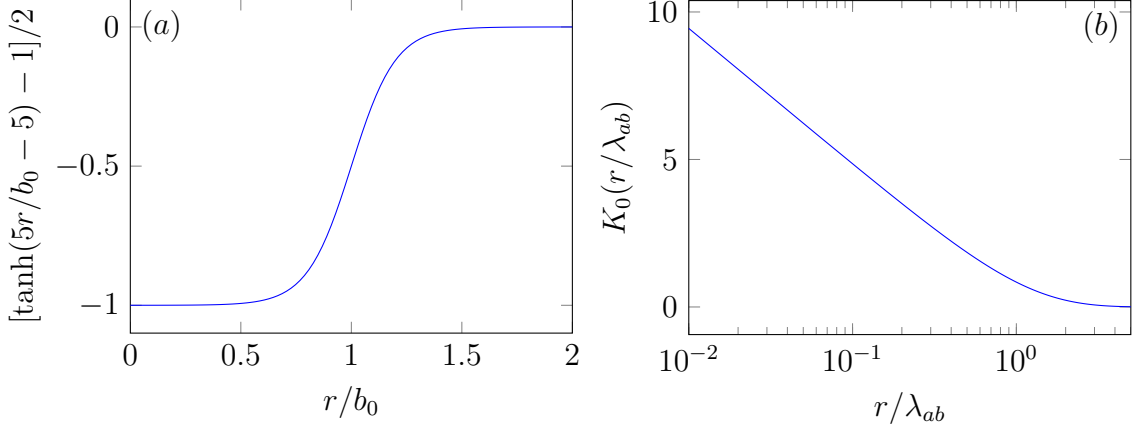


Figure B.2: Shape of the pinning and interaction potentials. (a) The pinning potential has the form of a smooth potential well. (b) The interaction potential between two vortex lines has the form of a modified Bessel function of the second kind.

2. Calculate the forces on all of the vortex line elements $\vec{F}_{i,l}(\{\vec{r}_{i,l}\})$.
3. Set the thermal force values to $\vec{f}_{i,j}(t) = \sqrt{\frac{2\eta k_B T}{\Delta t}} \vec{\zeta}_{i,l}(t)$, where the $\vec{\zeta}_{i,l}(t)$ are independent, Gaussian-distributed random variables fulfilling $\langle \vec{\zeta}_{i,l}(t) \rangle = 0$ and $\langle \vec{\zeta}_{i,l}(t) \cdot \vec{\zeta}_{j,m}(s) \rangle = \delta_{i,j} \delta_{l,m} \delta_{t,s}$.
4. Update the velocity of all vortex line elements $v_{i,l}(t) = \frac{1}{\eta} [\vec{F}_{i,l}(\{\vec{r}_{i,l}(t)\}) + \vec{f}_{i,l}(t)]$.
5. Forward interpolate the position of all vortex line elements $\vec{r}_{i,l}(t + \Delta t) = \vec{v}_{i,l}(t) \Delta t$.
6. Increase time by Δt .
7. Jump to step 2.

For simulations where we assume a finite vortex mass m , the Langevin equation acquires an additional inertial term and the time stepping becomes slightly more complicated. In this case we use the BBK time stepping scheme, described in reference [108].